Politecnico di Torino

ScuDo
Scuola di Dottorato ~ Doctoral School
WHAT YOU ARE, TAKES YOU FAR

Doctoral Dissertation
Doctoral Program in Civil and Environmental Engineering (36^{th} cycle)

Modelling of dynamic fracture by Phase Field and Finite Fracture Mechanics

By

Arturo Chao Correas

******

Supervisors:
Prof. M. Corrado, Supervisor, Politecnico di Torino
Prof. P. Cornetti, Co-supervisor, Politecnico di Torino
Prof. J. Reinoso, Co-supervisor, Universidad de Sevilla

Doctoral Examination Committee:
Prof. D. Kammer, Referee, ETH Zürich
Prof. E. Martínez Pañeda, Referee, University of Oxford
Prof. I. García García, Universidad de Sevilla
Prof. S. Invernizzi, Politecnico di Torino
Dr. Ing. P. Rosendahl, TU Darmstadt

Politecnico di Torino
2024

Declaration

I hereby declare that the contents and organization of this dissertation constitute my own original work and they do not compromise in any way the rights of third parties, including those relating to the security of personal data.

Arturo Chao Correas
2024

* This dissertation is presented in partial fulfillment of the requirements for **Ph.D. degree** in the Graduate School of Politecnico di Torino (ScuDo).

This thesis is dedicated to my loving parents and grandparents, for they are the foundations on which I rely.

Acknowledgements

It takes a village to raise a child

Any complex and lasting-in-time endeavour is, to some extent, governed by the underlying concept of this popular saying. Naturally, parents are bestowed with the responsibility of raising the child, just as it is also natural to share this task with the infant's social "village". As such, the resulting merits (and blame) do not belong exclusively to the the parents, but also to everyone involved. For that reason and in the spirit of fairness, I would like to use this personal space in my thesis to explicitly thank and acknowledge those who I believe have contributed most significantly to "raise this child".

Innanzitutto, vorrei ringraziare i miei supervisori del Politecnico di Torino, Mauro, Pietro e Alberto, che ormai considero cari colleghi e che sin dal primo giorno del mio percorso in Italia sono stati un supporto fondamentale. Da loro ho imparato tanto, anche l'italiano, e senza dubbio a loro appartiene una parte importante del merito di questa tesi. Inoltre, mi sento in dovere di riconoscere anche la loro contribuzione dal punto di vista personale, dato che sono riusciti a farmi sentire a casa nonostante stessi affrontando la sfida del dottorato in mezzo a una pandemia e appena arrivato in un paese straniero. Per tutto ciò, grazie.

Por otro lado, quiero agradecer la contribución de mi supervisor de la Universidad de Sevilla, José. A pesar de que yo haya estado físicamente en Turín durante la mayor parte del doctorado, su apoyo y ayuda desde la distancia han sido sin duda esenciales tanto para el desarrollo de la tesis, como para mi formación como joven científico. De Sevilla también querría destacar la labor de Vlado como coordinador del proyecto NEWFRAC, que no solo ha provisto de financiación económica, sino que también ha supuesto un entorno muy prolífico donde empezar mi carrera investigadora. Likewise, I would like to extend my gratitude to all students, supervisors and participants in the NEWFRAC project, for it has been an amazing opportunity for kicking off my research career.

Desde el punto de vista personal, quiero agradecer a mis padres su incansable e incondicional apoyo en esta ardua empresa. A pesar de las muchas vicisitudes afrontadas durante los últimos años, siempre han creído en mi y han encontrado el modo y la energía para levantarme cuando flaqueaban las fuerzas. También quiero dejar por escrito mi eterna gratitud a mis abuelos, y espero que en la distancia (terrenal o empírea) sean capaces de ver que, en parte gracias a sus esfuerzos y sacrificios durante años, su nieto está completando una tesis doctoral. A mi prima Candelas le agradezco que me propusiera la idea de hacer un doctorado, ya que me ha hecho descubrir un trabajo que me apasiona. Más allá de la familia, quiero reconocer a la que ha sido mi amiga y camarada durante el doctorado, Ángela, que ha hecho de esta dura etapa un viaje mucho más llevadero y enriquecedor.

Last but not least, to all my friends and colleagues from Politecnico, Francesco, Sasan, Mattia, Amir, Lorenza and many others that have been alongside me these almost four years, así como a mis amigos españoles de Turín, Alberto, Elena y Dani. To all of you, heartily thanks.

Now, without any further ado, let's go back to science!

Funding Acknowledgements

This project has received funding from the European Union's Horizon 2020 research and innovation programme under the Marie Skłodowska Curie grant agreement No 861061

Abstract

Fracture is the physical process through which an initially pristine and continuous structural domain undergoes changes in its mechanical configuration due to the development of an internal discontinuity over time. Macroscopically, this phenomenon manifests as a worsening in the structural performance of the affected components that eventually leads to a total collapse. Therefore, the proper understanding of the involved physics is essential for ensuring structural integrity. On the other hand, the inherent dynamism that arises from the evolution over time of fracturing systems suggests that the dynamic aspects of fracture should not be lightly neglected. In this context, the present thesis delves into the modelling of dynamic fracture by exploiting two different but complementary approaches: the Phase Field fracture model and the Finite Fracture Mechanics failure criterion. The former provides a highly-detailed and theoretically robust description of fracture that allows the development of a solid core understanding of the involved physics, albeit at a considerably high computational cost. In contrast, the latter failure criterion provides less detailed but cost effective predictions that align with experimental evidence, rendering it a useful tool for preliminary stages of structural design. As such, the present work provides a multi-perspective insight into the modelling of dynamic fracture.

The first thematic block is devoted to the Phase Field fracture model, which is introduced and developed following a bottom-up approach. Firstly, the framework is contextualized by describing the pioneer variational revisit of brittle fracture and its ensuing regularization that led to the original Phase Field fracture model. Thereafter, the generalized formulation of the Phase Field fracture model in a quasi-static context is introduced, and the main existent modelling options are briefly described. The ability of the approach to accurately reproduce crack growth under multi-axial stress states is then tested through a case study on the crack onset from circular holes under quasi-static biaxial loadings, in which reasonable agreement is shown with Dugdale's Cohesive Zone Model when the No-Tension strain energy decomposition

and the AT1 Phase Field model are used. With these learnings present, the Phase Field fracture model is subsequently developed in a dynamic context by virtue of Hamilton's principle and variational inequalities. In addition to the theoretical derivation of the governing principles, the main technical aspects concerning its numerical implementation with an explicit time integrator are also covered. Subsequently, the inherent ability of the Phase Field fracture model to reproduce complex crack patterns is exploited to study the post-punching fragmentation of biaxially pre-strained glass panes, depicting the effect of the pre-straining intensity and biaxiality on the resultant crack patterns. Eventually, the already introduced quasi-static and dynamic Phase Field fracture models are juxtaposed under unstable crack growth conditions, revealing that: (i) inertial effects are not negligible for such conditions, even under quasi-static loadings; (ii) the representativeness of the resulting crack paths is undermined if the actual diffusion of mechanical information is overlooked; and (iii) the irreversibility condition of fracture is significantly weakened if crack growth is not modelled progressively.

The second thematic block instead covers the Finite Fracture Mechanics failure criterion, once again following a bottom-up approach. Hence, the well-established quasi-static formulation is first introduced and then particularized to two different case studies. The first one involves the size-effect of failure when stemming from a spherical void embedded in a uniaxially tensioned infinite domain. This setup leads to relatively simple failure conditions, and available experimental results show reasonable agreement with the Finite Fracture Mechanics predictions. More complex failure conditions are instead obtained by retrieving the case study on the crack onset from circular holes under biaxial loadings, where the resultant Finite Fracture Mechanics predictions are found to agree with those of Dugdale's Cohesive Zone Model. Once the specific aspects of the criterion are understood in a quasi-static setup, its formulation is then extended to include sudden loadings. To that end, the basic requirements of proper dynamic failure criteria are first drawn, and then the existent approaches are put to the test. To address the identified shortcomings of the previously proposed criteria, a pre-emptive proposal for the dynamic Finite Fracture Mechanics is put forward, implemented, and compared with relevant sets of experiments. Despite the limited amount of experimental data, the proposed formulation shows promising capabilities for predicting the loading rate effect in the onset of cracks.

Sommario

La frattura è il processo fisico attraverso il quale un dominio strutturale, inizialmente intatto e continuo, subisce cambiamenti nella sua configurazione meccanica a causa dello sviluppo nel tempo delle discontinuità interne. Macroscopicamente, questo fenomeno si manifesta come una riduzione delle prestazioni strutturali dei componenti interessati, che porta infine al collasso. Perciò, la corretta comprensione della fisica coinvolta è necessaria per garantire l'integrità strutturale. D'altra parte, il dinamismo intrinseco che deriva dall'evoluzione delle fessure suggerisce che gli aspetti dinamici non debbano essere trascurati. In questo contesto, la presente tesi approfondisce la modellazione della frattura dinamica sfruttando due approcci diversi ma complementari: il modello di frattura con Campo di Fase e il criterio di rottura della Meccanica della Frattura Finita. Il primo rileva una descrizione dettagliata e teoricamente robusta del processo di fessurazione, consentendo lo sviluppo di una solida comprensione della fisica coinvolta, sebbene a un costo computazionale considerevole. D'altro canto, il secondo fornisce delle previsioni che, pur essendo meno dettagliate, sono in grado di riprodurre risultati sperimentali. Ciò, unito ad un minore costo computazionale, lo rende uno strumento adatto per le fasi preliminari della progettazione strutturale. Di conseguenza, il presente lavoro approfondisce da diverse prospettive la modellazione della frattura dinamica.

Il primo blocco tematico è dedicato al modello di frattura con Campo di Fase, il quale viene introdotto e sviluppato seguendo un approccio dal basso verso l'alto. Inizialmente, la metodologia viene contestualizzata introducendo sia la primigenia rivisitazione variazionale della frattura fragile, sia la regolarizzazione che ha portato al modello di frattura con Campo di Fase originale. Successivamente, la formulazione generalizzata si introduce in un contesto quasi statico, e le principali opzioni di modellazione esistenti vengono descritte brevemente. La capacità dell'approccio di riprodurre lo sviluppo della frattura in condizioni di tensione multi-assiale viene testata mediante uno studio sull'innesco di fessure da fori circolari presenti in domini

sottoposti a carichi biassiali e quasi statici, dove si riscontra un ragionevole accordo con il Modello di Zona Coesiva di Dugdale. Il modello di frattura con Campo di Fase viene successivamente sviluppato in un contesto dinamico in virtù del principio di Hamilton e delle disuguaglianze variazionali. Oltre alla derivazione teorica dei principi governanti, vengono trattati anche i principali aspetti tecnici relativi alla sua implementazione numerica con un integratore nel tempo esplicito. Inoltre, la capacità intrinseca del modello di frattura con Campo di Fase di riprodurre percorsi di frattura complessi viene sfruttata per studiare la frammentazione dovuta a punzonatura in lastre di vetro biassialmente pre-tensionate. In particolare, viene mostrato l'effetto sui percorsi di frattura risultanti dell'intensità e biassialità della pre-tensione. Infine, i già noti modelli di frattura con Campo di Fase quasi statico e dinamico vengono confrontati in condizioni di frattura instabile, rivelando che: (i) gli effetti inerziali non sono trascurabili per tali casi, anche sotto carichi quasi statici; (ii) la rappresentatività dei percorsi di frattura risultanti viene meno se trascurata la diffusione dell'informazione meccanica; e (iii) la condizione di irreversibilità della frattura risulta indebolita se lo sviluppo delle fessure non si modella progressivamente.

Il secondo blocco tematico tratta il criterio di rottura della Meccanica della Frattura Finita seguendo ancora un approccio dal basso verso l'alto. Pertanto, la ben consolidata formulazione quasi statica viene prima introdotta e poi particolarizzata per due geometrie (di studio). La prima coinvolge l'effetto di scala sulla rottura quando essa si innesca da un poro sferico presente in un dominio infinito sotto trazione uniassiale. Questa configurazione rileva condizioni di rottura relativamente semplici, e le previsioni della Meccanica della Frattura Finita mostrano un ragionevole accordo coi risultati sperimentali disponibili. Condizioni di rottura più complesse sono analizzate considerando l'innesco della frattura da fori circolari soggetti a carichi biassiali, dove le previsioni risultanti della Meccanica della Frattura Finita si trovano comunque in accordo con quelle del Modello di Zona Coesiva di Dugdale. Infine si introduce l'estensione del modello per includere carichi dinamici. A tale scopo i requisiti di base per i criteri di rottura dinamici vengono prima delineati, e poi si mettono alla prova gli approcci esistenti. Al fine di risolvere le carenze identificate, si propone una formulazione dinamica della Meccanica della Frattura Finita, la quale viene poi implementata e confrontata con dei set di esperimenti dinamici pertinenti. Nonostante la quantità limitata di dati sperimentali, la metodologia proposta si mostra promettente per prevedere l'effetto della velocità di carico sull'innesco della rottura.

Resumen

La fractura es el proceso físico a través del cual un dominio estructural inicialmente prístino y continuo sufre cambios en su configuración mecánica debido al desarrollo en el tiempo de discontinuidades internas. Macroscópicamente, este fenómeno se manifiesta como una reducción en el rendimiento estructural de los componentes afectados que eventualmente lleva a su colapso. Por tanto, la adecuada comprensión de la física involucrada es esencial para garantizar la integridad de estructural. Por otro lado, el dinamismo inherente de la evolución temporal de la fractura sugiere que los aspectos dinámicos no deben ser descuidados. En este contexto, la presente tesis profundiza en la modelización de la fractura dinámica explotando dos enfoques diferentes pero complementarios: el modelo de fractura con Campo de Fase y el criterio de fallo de la Mecánica de Fractura Finita. El primero proporciona una descripción detallada y teóricamente robusta de la fractura, permitiendo el desarrollo de una sólida comprensión de la física involucrada, aunque a un costo computacional considerable. En cambio, la segunda metodología proporciona predicciones más económicas que, aún siendo menos detalladas, son capaces de reproducir resultados experimentales, lo que le convierte en una herramienta útil para las etapas preliminares del diseño estructural. En consecuencia, el presente trabajo proporciona una visión multi-perspectiva de la modelización de la fractura dinámica.

El primer bloque temático está dedicado al modelo de fractura con Campo de Fase, el cual se introduce y desarrolla siguiendo un enfoque ascendente. En primer lugar, el marco se contextualiza introduciendo la revisión variacional de la fractura frágil primigenia, así como la regularización que llevó al modelo original de fractura con Campo de Fase. A continuación, se introduce la formulación generalizada en un contexto cuasi-estático, describiéndose brevemente las principales opciones de modelado existentes. La capacidad del modelo para reproducir con precisión el desarrollo de la fractura bajo estados de tensión multi-axial se prueba estudiando la nucleación de grieta desde agujeros circulares presentes en dominios bajo carga

biaxial y cuasi estática, caso para el cual se muestra un acuerdo razonable con el Modelo de Zona Cohesiva de Dugdale. El modelo de fractura con Campo de Fase posteriormente se desarrolla en un contexto dinámico en virtud del principio de Hamilton y las desigualdades variacionales. Además de la derivación teórica de los principios rectores, también se tratan los principales aspectos técnicos de su implementación numérica usando un integrador temporal explícito. Posteriormente, la capacidad inherente del modelo de fractura con Campo de Fase para reproducir grietas complejas se explota para estudiar la fragmentación post-punzonado de paneles de vidrio pre-tensados biaxialmente, detallando el efecto de la intensidad y la biaxialidad de la pre-tensión en la fragmentación resultante. Finalmente, los ya introducidos modelos de fractura con Campo de Fase cuasi estático y dinámico se yuxtaponen bajo condiciones de fractura inestable, revelando que: (i) los efectos inerciales no son despreciables para tales casos, incluso bajo cargas cuasi-estáticas; (ii) la representatividad de las grietas resultantes se ve socavada si se obvia la difusión real de la información mecánica; y (iii) la condición de irreversibilidad de la fractura se debilita si el crecimiento de grieta no se modela de forma progresiva.

El segundo bloque temático trata el criterio de fallo de la Mecánica de Fractura Finita siguiendo una vez más un enfoque ascendente. De este modo, primero se introduce la bien establecida formulación cuasi-estática y luego se particulariza a dos casos. El primero consiste en el estudio del efecto de escala de la rotura cuando esta se desarrolla a partir de un vacío esférico incrustado en un dominio infinito sometido a tensión uniaxial. Esta configuración genera condiciones de fallo relativamente simples, donde los resultados experimentales disponibles muestran un acuerdo razonable con las predicciones de la Mecánica de Fractura Finita. Condiciones de fallo más complejas se obtienen por otro lado recuperando el estudio de la nucleación de grieta desde agujeros circulares bajo cargas biaxiales, para el cual se obtiene que las predicciones de la Mecánica de Fractura Finita coinciden con las del Modelo de Zona Cohesiva de Dugdale. Una vez comprendido el criterio cuasi-estático, su formulación se extiende para incluir cargas dinámicas. Para ello, primero se determinan los requisitos básicos para un criterio de fallo dinámico, y luego se ponen a prueba los enfoques existentes. En base a las deficiencias identificadas, se presenta una propuesta para la Mecánica de Fractura Finita dinámica, la cual se implementa y se compara con resultados experimentales relevantes. A pesar de la cantidad limitada de datos empíricos, la formulación propuesta se muestra prometedora para predecir el efecto de la velocidad de carga en la nucleación de grietas.

Contents

List of Figures

List of Tables

List of Algorithms

Chapter 1

Introduction

1.1 Background and motivation

In the realm of mechanics, the term fracture encompasses all the physical phenomena related to the nucleation and propagation of cracks within structural domains. Its study and comprehension are the responsibility of Fracture Mechanics, a highly specialized branch of Structural Mechanics. In turn, the latter is deeply rooted in Newtonian mechanics, which provides the fundamental laws governing the motion and dynamics of systems under the umbrella of classical physics. The analysis of fracture cannot be thereby carried out independently from the principles of Newtonian physics, being only through this multi-layered lens that one can begin to unravel the complexities of material fracture.

As introduced in the very own Newton's *Principia* [1], the evolution of classical systems is dictated by a balance between mass, acceleration and forces, be they internal or external. As such, these are generally dynamic processes in that they present non-null inertial effects. Indeed, only in the idealized case of exact balance between the internal and external forces acting on a system with unchanging mechanical configuration, the resulting acceleration is null, and its evolution (or the lack thereof) can be perfectly static with respect to an inertial reference system. Particularizing to fracture, this statement implies that crack development is always a dynamic process for it entails changes in the structural domains itself; only under very restrictive conditions it can be treated quasi-statically, i.e. insofar as the rate of change of any involved magnitude or characteristic is negligible.

The two main sources of dynamic effects in a fracture problem are the external loading and the internal changes in the mechanical configuration due to crack growth. From a rigorous standpoint, a quasi-statically loaded system undergoing sudden failure is as dynamic as if the applied loading rapidly changes. For that reason, only through the comprehensive study of dynamic fracture, in the sense of both sudden loadings and fast growing cracks, the breakage mechanisms featured by real-world components can be understood and their structural integrity can be ensured. Certainly, the study of dynamic evolutions in a continuum context is not straightforward even upon "stationary" domains[1], let alone when time-dependent cracks come into play. For that reason, most of the developments within the Fracture Mechanics field are left to sprout in a quasi-static context and, once mature enough, they are transplanted into a more complete dynamic framework.

Regarding the evolution of Fracture Mechanics as a scientific field, its starting point is now consensually identified in the work by Griffith [2], although it remained quite unnoticed until Irwin's work [3]. In any case, the study of cracks had already garnered certain interest within the scientific community, especially in what concerns the effect of their presence on the quasi-static solution of the elastic problem [4–6]. Later on, the dynamic nature of crack evolution, unquestionable in many cases, also favoured the research on non-stationary cracks [7–9]. However, these studies were carried out under strong simplifying assumptions so as to keep the studies analytical, and as such, they overlooked or could not explain some experimentally observed phenomena like crack branching or the actual upper bound for crack velocities [10–13].

The introduction of the numerically-convenient Cohesive Zone Model [14, 15], boosted by the ever improving computational capabilities, eventually allowed for conducting much less restrained analyses on dynamic fracture. In this sense, the numerical implementation of a dynamic cohesive framework was proven able to reproduce crack branching or the upper-bounded crack tip velocity [16]. Thereafter, several studies have exploited the Cohesive Zone Model to study complex dynamic fracture conditions, including high-velocity impacts [17], fragmentation [18, 19] or unstable crack propagations [20, 21], to mention but a few. Indeed, the much less restrictive numerical setup enabled capturing phenomena that had hitherto been out-of-reach. On the downside however, Cohesive Zone Models can only propagate

[1] Stationary domains in that they present an unchanging mechanical configuration.

cracks along predefined paths, unless specific re-meshing or kinematic enrichment techniques are used, thus undermining their representativeness for modelling bulk fracture.

In an attempt to introduce a generalized approach to brittle bulk fracture within a variational context, the Phase Field fracture model was introduced [22, 23]. Its main advantage lies in the obtention of the crack topology as an outcome of an energy minimization principle, thus eliminating the need to define its potential paths *a priori*. Likewise, the numerically challenging sharp discontinuities are regularized through the introduction of a continuous phase field that governs the material soundness, considerably easing the numerical implementation and reducing the problem's mesh dependency. The intricacies of this regularization and its effect on the resulting predictions have been the focus of many studies [24–26]. Moreover, the variational origin of the framework allows for a straightforward incorporation of the inertial effects, and theoretically robust dynamic frameworks are available [27–29]. Subsequently, these have proven to reproduce certain complex dynamic fracture phenomena [30–32] that were mostly out of reach for previous modelling frameworks.

However, any degree of failure is unacceptable for some structural applications, and hence it is only of interest therein to predict when fracture nucleates, and not how it evolves afterwards. In most of these cases, the highly-detailed approaches introduced above can still provide the required answers, yet at a considerable computational cost. Instead, a cheaper alternative is to develop a failure criterion capable of predicting when and where fracture onsets. Being computationally lighter in most cases, such a strategy is more convenient for the iterative and preliminary stages of structural design. Notice that this pathway has been the classical way of dealing with material fracture, with some relevant pre-modern scientific rationale being documented as early as in Galileo's [33]. Arguably, this represented an early proposal of a stress-based failure criterion, although it was not until Rankine's [34] that the first stress failure criterion would take its modern shape. On the other hand, Griffith's proposal [2] can be regarded as the inception of energy-based failure criteria.

As simple as they are, early failure criteria lacked generality: local stress approaches only work for plain geometries, whereas large cracks are required for those relying on the infinitesimal energy release. In an aim to bridge the uncovered set of configurations in between, several studies proposed more general failure crite-

ria that non-locally assess a stress or an energy condition [35–38]. These showed promising predictive capabilities, although some important limitations still applied. In this context, the modern Finite Fracture Mechanics framework for crack onset was introduced in [39, 40] by taking the paradigm of non-local assessment further and coupling stress and energy failure conditions. Its main underlying concept is to regard crack onset as a phenomenon that is: (i) instantaneous in time and finite in space, and (ii) subjected to the simultaneous fulfilment of both stress and energy conditions. The resultant framework has ever since proven to be effective in predicting failure onset upon a wide variety of stress-raisers under quasi-static loadings [41]. In contrast, the panorama of existent failure criteria applicable to sudden loadings is noticeably less well-established, and despite some relevant proposals having been made [42–44], these still present limited predictive capabilities and applicability.

1.2 Main objectives

The primary objective of this thesis is to provide a comprehensive insight into the modelling of dynamic fracture so as to improve its understanding and eventually contribute to the enhancement of structural safety. In particular, such a task is herein carried out through the Phase Field fracture model and the Finite Fracture Mechanics failure criterion. These two well-established frameworks represent disparate but complementary approaches to the modelling of fracture; the former aims at a detailed physical description of the phenomenon, whereas the latter restrains itself to positing the necessary and sufficient conditions for a crack to nucleate. This dichotomy allows for a thorough, two-sided analysis of dynamic fracture that covers from pure theoretical aspects up to the development of predictive engineering-grade tools.

Regarding the Phase Field modelling of fracture, both the quasi-static and dynamic frameworks have already been proposed in the literature with a great deal of success. Therefore, the present work will not focus on developing a new and disruptive formulation, but instead on validating and delving into the predictive capabilities of the existing Phase Field fracture model, first in quasi-static contexts and then in dynamic ones. Once presented and well-understood, both variants are confronted using bespoke case studies so as to unequivocally prove that every fracturing system should indeed be treated as dynamic unless the validity of quasi-static hypotheses has been ascertained, both locally and globally. This statement eventually leads to the

ultimate objective of the first thematic block, which is to provide proof supporting that quasi-static fracture is a very restrictive case of the dynamic one, and that naively neglecting this aspect can lead to unsafe failure predictions.

The second thematic block, on the other hand, covers the deep-rooted Finite Fracture Mechanics framework for crack nucleation. In this case however, there is no well-established formulation applicable to dynamic loading scenarios. The main objective of this section is thereby to make an experimentally supported proposal in such regard. Once again, a bottom-up approach to the undertaken task is followed: first, the conventional quasi-static criterion is introduced and implemented for different cases; then, a modified formulation that incorporates rate-dependent loadings is presented, discussed, implemented, and finally, validated with experimental evidence.

1.3 Thesis outline

The contents of this thesis are therefore organized in two thematic blocks that spread along five chapters. The first block, which covers the Phase Field fracture model, is structured as follows.

Chapter 2 serves as an introduction to the Phase Field fracture model, describing the origins of the framework and developing its formulation in a quasi-static context. The different modelling choices, functions and parameters are described in detail so as to get familiarized with the methodology. Eventually, the introduced approach is used to study the failure onset from a circular hole under remote biaxial loading conditions, validating the resultant predictions against those of Dugdale's Cohesive Zone Model.

Chapter 3 drops the quasi-static hypothesis and describes the Phase Field fracture model in a dynamic context. Particular attention is paid not only to the theoretical framework but also to the technical aspects concerning its numerical implementation. The potential of the approach for modelling dynamic fracture is exploited to conduct a case study on the post-punching fragmentation of a biaxially pre-strained glass pane under different loading conditions.

Chapter 4 makes use of the already introduced quasi-static and dynamic variants of the Phase Field fracture model, and delves into the differences between the respec-

tive predictions upon unstable crack growth under quasi-static loadings. Particularly, the lack of representativeness of the former approach is revealed evident through a series of case studies, including simple spring-mass models of multi-ligament fracture, detailed Phase Field simulations and experimental results. In contrast, the dynamic Phase Field fracture model is shown to yield theoretically robust predictions that align with the empirical findings.

The second block covers instead the Finite Fracture Mechanics approach for crack nucleation, and spans along two chapters that are organized as described below.

Chapter 5 introduces the well-established coupled criterion of Finite Fracture Mechanics for predicting crack onset under quasi-static loading conditions. The described approach is then used to study the size-effect of failure in a uniaxially-tensioned infinite domain that contains a single spherical void, and the resultant predictions are proven to closely agree with the experimental data from the literature. Besides, the previously studied case of crack onset from a circular hole under remote biaxial loading conditions is also tackled with this approach, yielding failure predictions comparable to those already obtained.

Chapter 6 undertakes the modification of the Finite Fracture Mechanics criterion to enable its implementation under sudden (dynamic) loadings. To that end, a discussion covering the requisites to be fulfilled by a generic dynamic failure criterion is first presented, and then the existent proposals are put to the test. Once identified their shortcomings, a tentative proposal for the dynamic Finite Fracture Mechanics criterion is presented, implemented for different dynamic setups, and the resultant failure predictions are validated with the results from relevant dynamic experiments.

Chapter 2

Phase Field fracture model[1]

2.1 Introduction

Widely regarded as the father of Fracture Mechanics, Griffith [2] pioneered the use of energetic considerations for predicting fracture. The advent of this approach was mainly triggered by the work of Inglis [4], which proves that elastic solutions present stress singularities at sharp corners. Such a discovery showed that the then contemporary stress-based failure criteria are unsuitable for cracked and notched domains, since these would predict breakage at an arbitrarily small loading intensity. To overcome this limitation, Griffith regarded failure in cracked domains as governed by a competition between the decrease of potential energy and the increase of surface energy upon infinitesimal crack growth; hence, failure develops when it leads to a reduction in the system's energy. This groundbreaking paradigm proved fruitful and eventually became the cornerstone of the Linear Elastic Fracture Mechanics framework.

Despite its subsequent success, the simplicity of Griffith's proposal came at the cost of significant limitations. For instance, it requires the pre-existence of a sufficiently large crack within the domain, thus not being able to describe how cracks

[1] Part of the work described in this chapter has been published in: **(i)** Chao Correas, A., Sapora, A., Reinoso, J., Corrado, M., Cornetti, P. (2023). Coupled versus energetic nonlocal failure criteria: A case study on the crack onset from circular holes under biaxial loadings. *Eur J Mech A Solids* 101, 105037; and **(ii)** Chao Correas, A., Reinoso, J., Cornetti, P., Corrado, M. (2024). On the (lack of) representativeness of quasi-static variational fracture models for unstable crack propagation. *J Mech Phys Solids* 186, 105573.

appear in the first place. Even if so, the obtainable predictions are mostly limited to the loading intensity that triggers fracture, although it can also provide some insights on the stability and direction of propagation right after onset. In any case, the prediction of complete crack patterns is out of reach. As such, it cannot explain complex but practically important fracture phenomena such as crack branching, coalescence or kinking. Moreover, its reliance on perfectly linear elastic solutions limits the applicability to many widespread and not-so-brittle structural materials, *inter alia* concrete, metals or polymers.

Aiming at broadening the applicability of Griffith's energetic approach to fracture, Dugdale [14] and Barenblatt [15] put forward the concept of cohesive forces. Their proposal assumed that the continuum's stress-strain constitutive relation only holds below a certain stress threshold, above which the behaviour turns cohesive, i.e. governed by a stress-crack opening law. Hence, cohesive process zones develop in the vicinities of highly stressed regions, wherein material softening occurs and fracture energy builds up. In some sense, these cohesive laws mimic the essence of intermolecular forces, and it is through their tailoring that the model can reproduce different fracturing behaviours. Nonetheless, the interfacial nature of cohesive process zones restraints numerical implementations to only develop fracture within predefined regions, thus precluding a rigorous reproduction of generic bulk fracture.

To cover the niche of modelling bulk fracture, Griffith's framework was revisited from a variational standpoint by Francfort and Marigo [22] and, for the first time, the whole crack pattern was considered as an output of the energy minimization principle. The original proposal in itself was eminently theoretical due to its unpractical implementation, but it did pave the way for the subsequent highly-successful variational approaches to bulk fracture. In this sense, Bourdin, Francfort and Marigo [23] presented a theoretically robust regularized model of bulk fracture by exploiting the mathematical developments of Ambrosio and Tortorelli for image segmentation problems [45]. Particularly, this approach consisted in smearing sharp cracks into the domain through a continuous *phase field* that governs the state of a material, hence the name of Phase Field fracture models. The resultant variational framework turned out dual in nature: on one hand, it acts as a Gradient Damage Model upon crack nucleation; on the other, it represents a regularization of Griffith's problem in the sense of Γ-convergence when into crack propagation [46]. In addition to this, the regularized formulation shows thermodynamical consistency and can be easily implemented in conventional Finite Element frameworks [47, 48].

Given its theoretical robustness, versatility and simplicity of implementation, several pieces of research have been ever since devoted to comprehend, generalize and exploit the full potential of Phase Field fracture models. In this sense, one can highlight the theoretical studies in [25, 26] which illustrate several mathematical formalisms, such as the stability of the homogeneous solution, the localization of damage along bands and the size-effect of failure. The model's performance under multiaxial stress states has also been a topic of great interest and many proposals have been developed in this regard [49, 24, 50–52], allowing for instance the modelling of fracture in the presence of interacting stress concentrators [53]. More complex material behaviours have also been tackled, with applications to anisotropic [54] and heterogeneous [55] materials being available in the literature. The model's versatility is ultimately proven by its applicability to studying fracture in multi-physics problems, including but not limited to those concerning thermo-elasto-plasticity [56], thermal shocks [26], hydrogen embrittlement [57], electro-chemo-mechanical degradation [58], corrosion-driven damage in fractal porous media [59], and hygro-thermo-mechanical degradation [60].

The present chapter is thus devoted to introduce and describe the widespread Phase Field fracture model for quasi-static setups. To that end, a bottom-up approach to the framework is utilized: first, the evolution of variational approaches to bulk fracture towards the Phase Field fracture model is presented, followed this by the derivation of the latter's generalized weak form and the introduction of the most common formulations available. The presented approach is then exploited to conduct a case study on the crack onset from circular holes under biaxial loadings, which yields a wide range of failure conditions and complex stress states. Lastly, the resultant predictions are validated through comparison with the well-established Dugdale's Cohesive Zone Model.

2.2 Variational approaches to bulk brittle fracture

Let us consider the N-dimensional fracture mechanics problem described in Fig. 2.1, where an elastic domain $\Omega \in \mathbb{R}^N \,|\, N \in \{2, 3\}$ with an external boundary $\partial\Omega \in \mathbb{R}^{N-1}$ is subjected to quasi-static mechanical solicitations. Hence, Ω deforms per a displacement field $\underline{u} : \Omega \to \mathbb{R}^N$ that complies with certain Dirichlet and Neumann boundary conditions along $\partial_u\Omega$ and $\partial_f\Omega = \partial\Omega \setminus \partial_u\Omega$, respectively. Let us further introduce in

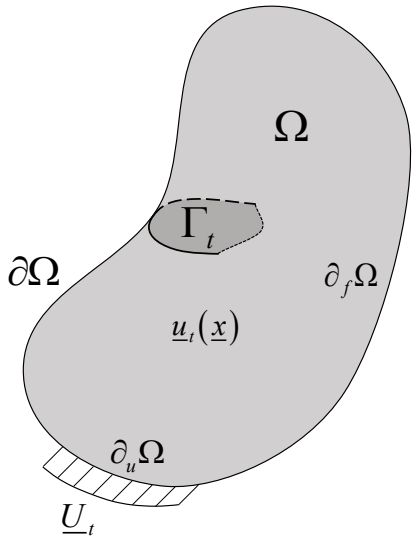

Fig. 2.1 Schematic representation of a classical displacement-controlled Fracture Mechanics problem.

Ω an internal sharp crack $\Gamma \in \mathbb{R}^{N-1}$ so that the displacement field $\underline{u}$ is not necessarily continuous therein. In the absence of body forces and pressure components, i.e. $\underline{b} = \underline{0} \ \ \forall \underline{x} \in \Omega$ and $\underline{f} = \underline{0} \ \ \forall \underline{x} \in \partial_f \Omega$, the work done by the prescribed external forces $\mathscr{W}_{\text{ext}}$ is null, and the domain's potential energy $\mathscr{P}$ is the sum of strain $\mathscr{E}_{\text{str}}$ and fracture $\mathscr{E}_{\text{frac}}$ energies. For the instant t, this reads as:

$$\mathscr{P}(\underline{u}_t, \Gamma_t) = \mathscr{E}_{\text{str}}(\underline{u}_t, \Gamma_t) + \mathscr{E}_{\text{frac}}(\Gamma_t)\,, \tag{2.1}$$

$$\mathscr{E}_{\text{str}}(\underline{u}_t, \Gamma_t) = \int_{\Omega\setminus\Gamma_t} \frac{1}{2}\lambda \,\text{tr}\Big(\underline{\underline{\varepsilon}}(\underline{u}_t)\Big)^2 + \mu\left(\underline{\underline{\varepsilon}}(\underline{u}_t) : \underline{\underline{\varepsilon}}(\underline{u}_t)\right) \mathrm{d}\underline{x}, \tag{2.2}$$

$$\mathscr{E}_{\text{frac}}(\Gamma_t) = \int_{\Gamma_t} G_C \,\mathrm{d}\underline{x}, \tag{2.3}$$

where $\bullet_t$ represents the value of a magnitude $\bullet$ at the instant t, λ and μ are the Lamé constants, G_C stands for the specific fracture energy, and $\underline{\underline{\varepsilon}}(\underline{u})$ is the infinitesimal strain tensor:

$$\underline{\underline{\varepsilon}}(\underline{u}) = \frac{\nabla\underline{u} + \nabla^{\mathrm{T}}\underline{u}}{2}. \tag{2.4}$$

After revisiting brittle fracture from a variational perspective, Francfort and Marigo [22] theorized that the system evolution in terms of $(\underline{u}_t, \Gamma_t)$ is governed by the global minimization of $\mathscr{P}$. Their proposal was in turn subjected to the inequality condition $\Gamma_t \subseteq \Gamma_{t+\Delta t} \ \ \forall \Delta t > 0$, so as to account for the irreversibility of fracture and forbid material healing. This way, the resultant variational model impedes the crack

set Γ_t to unrealistically shrink or translate with respect to previous states. At the same time, no information regarding the prospective crack pattern is required *a priori*, for this is an outcome of the conditioned minimization problem. This latter feature undoubtedly represents the biggest advantage of the proposed variational approach to bulk fracture, since it allows robust modelling of complex fracture phenomena, such as crack branching, coalescence and kinking, among others.

Despite such an outstanding upside, the original proposal from [22] is not devoid of weaknesses. For instance, by considering the global minimization of $\mathscr{P}$ as the governing principle, the model can unrealistically overcome any arbitrarily large energetic barrier in order to reach the globally stable state [61]. On the other hand, the potential discontinuity of $\underline{u}$ along Γ renders its numerical implementation rather tortuous, especially given that the latter evolves in time and is not necessarily coherent with the spatial discretization of Ω.

The latter difficulty was somehow sorted out in [23], where a theoretically rigorous regularization of the sharp problem above was put forward after exploiting the mathematical developments from [45]. The proposed approach relies on enriching the displacement problem so that a continuous scalar field $\alpha : \Omega \to [0,1]$ (so-called *phase field*) portrays a smeared representation of Γ. This way, the displacement jumps are regularized along a finite region of dimension $\sim \ell$, and thus $\underline{u}$ remains continuous even for "cracked" configurations. Likewise, since the concept of sharp cracks no longer holds in the regularized approach, $\mathscr{E}_{\text{frac}}$ must be instead computed by the domain integral of a proper elliptic functional of α. Assuming that $\alpha = 0$ and $\alpha = 1$ represent pristine and broken conditions, respectively, the original Phase Field fracture model (PFM) can be interpreted to rely on the global minimization of the following potential energy functional $\mathscr{P}$ [23]:

$$\mathscr{P}(\underline{u}_t, \alpha_t) = \mathscr{E}_{\text{str}}(\underline{u}_t, \alpha_t) + \mathscr{E}_{\text{frac}}(\alpha_t)\,, \tag{2.5}$$

$$\mathscr{E}_{\text{str}}(\underline{u}_t, \alpha_t) = \int_\Omega \left[(1-\alpha_t)^2 + k\right] \left[\frac{1}{2}\lambda\, \text{tr}\Big(\underline{\underline{\varepsilon}}(\underline{u}_t)\Big)^2 + \mu\left(\underline{\underline{\varepsilon}}(\underline{u}_t) : \underline{\underline{\varepsilon}}(\underline{u}_t)\right)\right] \mathrm{d}\underline{x}, \tag{2.6}$$

$$\mathscr{E}_{\text{frac}}(\alpha_t) = \int_\Omega G_C \left(\frac{\alpha_t^2}{2\ell} + \frac{\ell}{2}\nabla\alpha_t \cdot \nabla\alpha_t\right) \mathrm{d}\underline{x}, \tag{2.7}$$

where k is a small parameter ($k \ll 1$) that ensures the well-posedness of the numerical implementation when $\alpha \to 1$. Given the multi-field description of the

regularized problem, both $\underline{u}_t$ and α_t are admissible only if they comply with their corresponding Dirichlet boundaries, i.e. $\underline{u}_t(\underline{x} \in \partial_u\Omega) = \underline{U}_t$ and $\alpha_t(\underline{x} \in \partial_\alpha\Omega) = A_t$. Likewise, the admissibility of α_t is also subjected to the irreversibility condition of fracture, which translates upon regularization to $\alpha_t(\underline{x} \in \Omega) \geq \alpha_s(\underline{x} \in \Omega) \quad \forall s < t$.

The global minimization of PFM's potential energy functional $\mathscr{P}$ is not trivial for it is not convex in $(\underline{u}_t, \alpha_t)$, yet it is so in both[2] $(\underline{u}_t; \alpha_t)$ and $(\alpha_t; \underline{u}_t)$. Therefore, the minimization of $\mathscr{P}$ can be undertaken by combining a staggered approach with an alternate minimization scheme, although at the cost of only getting convergence to stationary points [62]. Anyhow, it was already suggested in [23] that metastable evolutions are probably more realistic than globally stable ones. All of this, combined with the proven thermodynamic consistency [47], led to the widespread adoption of the PFM with the staggered alternate minimization as the default resolution scheme (see e.g. [46, 26, 24]). Remarkably, relaxing the search of minimizers from global to local also reconciles the variational approach to bulk fracture with the original Griffith's criterion for infinitesimal crack growth [2].

2.3 Weak form of the Phase Field fracture model

The PFM has come a long way since its first proposal in [23], and ever since many studies have been devoted to its study and generalization (see e.g. [25, 26, 52, 63]). The generic description of the strain and fracture energy component can be written as:

$$\mathscr{E}_{\text{str}}(\underline{u}_t, \alpha_t) = \int_\Omega \psi\Big(\underline{\underline{\varepsilon}}(\underline{u}_t), a_{\text{PF}}(\alpha_t)\Big)\, \mathrm{d}\underline{x}, \tag{2.8}$$

$$\mathscr{E}_{\text{frac}}(\alpha_t) = \int_\Omega \frac{G_C}{c_w}\left(\frac{w_{\text{PF}}(\alpha_t)}{\ell} + \ell\,\nabla\alpha_t \cdot \nabla\alpha_t\right) \mathrm{d}\underline{x}, \tag{2.9}$$

where ψ stands for the strain energy density modulated by the degradation function $a_{\text{PF}}(\alpha)$, $w_{\text{PF}}(\alpha)$ is a function that governs the local term of $\mathscr{E}_{\text{frac}}$, and c_w is a scaling parameter defined as in Eq. (2.10). It results evident from Eq. (2.9) that ℓ weights the relative importance of the local and non-local terms in $\mathscr{E}_{\text{frac}}$, so that for a large (small) values of ℓ, smooth (sharp) transitions of α are energetically cheaper.

$$c_w = 4\int_0^1 \sqrt{w_{\text{PF}}(\alpha)}\, \mathrm{d}\alpha \tag{2.10}$$

[2]The semicolon separates variable fields to its left from fixed ones to its right.

In the herein considered quasi-static framework, the inclusion of non-null external forces of either surface $\underline{f}$ or body $\underline{b}$ type can jeopardize the problem resolution due to the domain softening as fracture develops. For that reason, it is a common practice to perform the quasi-static implementation of the PFM under displacement control and refrain from considering non-null external work components $\mathscr{W}_{\text{ext}}$.

Following the conventionalities of variational procedures, the admissibility of both $\underline{u}_t$ and α_t fields is weakly imposed by requiring them to belong to the affine spaces V_t and B_t, correspondingly defined as:

$$\mathrm{V}_t = \left\{ \underline{u}_t : \Omega \to \mathbb{R}^N \,|\, \underline{u}_t = \underline{U}_t \;\; \forall \underline{x} \in \partial_u \Omega \right\}, \tag{2.11}$$

$$\mathrm{B}_t = \left\{ \alpha_t : \Omega \to [0,1] \;\middle|\; \begin{array}{ccc} \alpha_t = A_t & \forall \underline{x} \in \partial_\alpha \Omega & \text{and} \\ 0 \leq \alpha_\tau \leq \alpha_t \leq 1 & \forall \underline{x} \times \tau \in \Omega \times [0,t) & \end{array} \right\}. \tag{2.12}$$

Likewise, the admissible variations $\delta\underline{u}$ and $\delta\alpha$ belong to the vector spaces V_0 and B_0, respectively, which are in turn the homogeneous counterparts of V_t and B_t. Upon this, the governing variational principle of the PFM can be obtained from the first order stability condition $\delta\mathscr{P} \geq 0$, which once developed results in:

$$\mathrm{D}_{\underline{u}}\mathscr{P}(\underline{u}_t, \alpha_t)\,[\delta\underline{u}] + \mathrm{D}_\alpha \mathscr{P}(\underline{u}_t, \alpha_t)\,[\delta\alpha] \geq 0 \;\; \forall \{\delta\underline{u}, \delta\alpha\} \in \{\mathrm{V}_0, \mathrm{B}_0\}, \tag{2.13}$$

where the notation $\mathrm{D}_\phi \mathscr{F}(\phi, ...)\,[\delta\phi]$ represents the first Gateaux derivative of the functional $\mathscr{F}$ with respect to the field ϕ and in the direction of the variation $\delta\phi$. Remarkably, the weak inequality in Eq. (2.13) stems from the irreversibility of α and portraits duality in the system's evolution: if the irreversibility condition is not violated, the solution lies at a stationary admissible state ($\delta\mathscr{P} = 0$); otherwise, it lies in an admissible state surrounded by either inadmissible or higher potential energy states ($\delta\mathscr{P} > 0$).

Certainly, $\mathscr{P}$ not being convex in $(\underline{u}_t, \alpha_t)$ means that also the second order stability condition is required in order to determine whether the stationary point obtained from solving Eq. 2.13 is actually a minimum [26]. Nonetheless, a workaround to this burden is possible on the basis that $\mathscr{P}$ is convex on both $(\underline{u}_t; \alpha)$ and $(\alpha_t; \underline{u})$: a local minimum of $\mathscr{P}$ can be iteratively approached through alternate minimization

of the staggered variational principles, which are defined as follows:

$$\mathrm{D}_{\underline{u}}\mathscr{P}(\underline{u}_t;\,\alpha)\,[\delta\underline{u}] = 0 \;\; \forall \delta\underline{u} \in \mathrm{V}_0\,, \tag{2.14}$$

$$\mathrm{D}_{\alpha}\mathscr{P}(\alpha_t;\,\underline{u})\,[\delta\alpha] \geq 0 \;\; \forall \delta\alpha \in \mathrm{B}_0\,. \tag{2.15}$$

Substituting the generalized energetic components from Eqs. (2.8) and (2.9) and developing the functional derivatives, the staggered governing principles for both the displacement and phase field problems result as:

$$\int_{\Omega} \underline{\underline{\sigma}}\Big(\underline{\underline{\varepsilon}}(\underline{u}_t)\,;\, a_{\mathrm{PF}}(\alpha)\Big) : \underline{\underline{\varepsilon}}(\delta\underline{u})\,\mathrm{d}\underline{x} = 0 \;\; \forall \delta\underline{u} \in \mathrm{V}_0\,, \tag{2.16}$$

$$\begin{aligned}\int_{\Omega} \frac{G_C}{c_w}\left(\frac{1}{\ell}\frac{\partial w_{\mathrm{PF}}(\alpha_t)}{\partial\alpha}\cdot\delta\alpha + 2\ell\,\nabla\alpha_t\cdot\nabla\delta\alpha\right)\mathrm{d}\underline{x} + \\ + \int_{\Omega}\frac{\partial\psi\Big(a_{\mathrm{PF}}(\alpha_t)\,;\,\underline{\underline{\varepsilon}}(\underline{u})\Big)}{\partial\alpha}\cdot\delta\alpha\,\mathrm{d}\underline{x} \geq 0 \;\; \forall\delta\alpha\in\mathrm{B}_0\,,\end{aligned} \tag{2.17}$$

where the notation $\partial g(\phi_t)/\partial\phi$ represents the first derivative of the function g with respect to ϕ evaluated at ϕ_t, the integrand $\partial\psi/\partial\alpha$ in Eq. (2.17) is commonly referred to as the crack driving force, and $\underline{\underline{\sigma}}$ stands for the stress tensor. The latter is nothing but the dual magnitude of the strain $\underline{\underline{\varepsilon}}$, and hence gets defined as:

$$\underline{\underline{\sigma}}\Big(\underline{\underline{\varepsilon}}(\underline{u})\,;\, a_{\mathrm{PF}}(\alpha)\Big) = \frac{\partial\psi\Big(\underline{\underline{\varepsilon}}(\underline{u})\,;\, a_{\mathrm{PF}}(\alpha)\Big)}{\partial\underline{\underline{\varepsilon}}}\,. \tag{2.18}$$

In Eqs. (2.16) and (2.17), the parameters fed to each staggered equation are "generic" fields, i.e. not related to any instant t in particular. This notation is chosen to emphasize that such fields are no longer unknowns but externally-defined inputs. In any case, for the staggered variational principles to be coherent with the original one in Eq. (2.13), both fixed fields should always correspond to their best estimates available. Even in that case, the sequential resolution of Eqs. (2.16) and (2.17) does not necessarily yield a good approximation to the solution of Eq. (2.13), specially upon coarse time-discretizations. For that reason, it is essential for the representativeness of the quasi-static PFM to perform proper convergence control within the alternate minimization procedure.

2.3.1 Phase Field laws for stiffness degradation and homogeneous fracture energy

The dependence of the generalized PFM with α is hence governed by two different laws: $a_{\mathrm{PF}}(\alpha)$ for the stiffness degradation, and $w_{\mathrm{PF}}(\alpha)$ for the homogeneous fracture energy term. In particular, for a function $a_{\mathrm{PF}}(\alpha)$ to be admissible as a Phase Field law for stiffness degradation, it must comply with the following conditions [47]:

$$a_{\mathrm{PF}} : \alpha \to [0,1] \left| \begin{array}{l} a_{\mathrm{PF}}(\alpha=0)=1 \ \text{ and} \\ a_{\mathrm{PF}}(\alpha=1)=0 \ \text{ and} \\ \quad a'_{\mathrm{PF}}(\alpha)<0 \quad \text{ and} \\ a'_{\mathrm{PF}}(\alpha=1)=0 \end{array} \right. , \tag{2.19}$$

so that a_{PF} yields one and zero for pristine and broken conditions, respectively, evolving monotonically in between. Likewise, the not-so-straightforward fourth condition ensures that the crack driving force vanishes as $\alpha \to 1$, thus inherently upper bounding α. On the other hand, the suitability conditions of the Phase Field law for the homogeneous fracture energy $w_{\mathrm{PF}}(\alpha)$ are [26]:

$$w_{\mathrm{PF}} : \alpha \to [0,1] \left| \begin{array}{l} w_{\mathrm{PF}}(\alpha=0)=0 \ \text{ and} \\ w_{\mathrm{PF}}(\alpha=1)=1 \ \text{ and} \\ \quad w'_{\mathrm{PF}}(\alpha)>0 \end{array} \right. , \tag{2.20}$$

which entail that the homogeneous fracture energy component must monotonically increase from zero to one as α transitions from pristine to broken conditions.

The requirements above can be fulfilled by simple polynomial functions such as those from the widespread AT1 and AT2 models in Eqs. (2.21) and (2.22), respectively. Clearly, $a_{\mathrm{PF}}(\alpha)$ is the same quadratic polynomial for both cases and the difference resides instead in the choice of $w_{\mathrm{PF}}(\alpha)$: AT1 considers a linear expression as opposed to the quadratic one in the AT2 model. This difference in the definition results in noticeable differences behaviour-wise, as proven by the corresponding one-dimensional localized profiles α_{1D} illustrated in Fig. 2.2, which are obtained for an infinite 1D bar under traction that breaks in the surroundings of $x = 0$.

$$\text{AT1 } [25]: \begin{cases} a_{\text{PF}}(\alpha) = (1-\alpha)^2 \\ w_{\text{PF}}(\alpha) = \alpha \\ c_w = \dfrac{8}{3} \\ \alpha_{\text{1D}}\left(-2\ell \le x \le 2\ell\right) = \left(1 - \dfrac{|x|}{2\ell}\right)^2 \end{cases} \tag{2.21}$$

$$\text{AT2 } [23]: \begin{cases} a_{\text{PF}}(\alpha) = (1-\alpha)^2 \\ w_{\text{PF}}(\alpha) = \alpha^2 \\ c_w = 2 \\ \alpha_{\text{1D}}\left(x \in \mathbb{R}\right) = \exp\left(-\dfrac{|x|}{\ell}\right) \end{cases} \tag{2.22}$$

In a generic N-dimension scenario, this translates into the AT1 damaged regions being compactly supported so that purely elastic behaviour $(\alpha = 0)$ is allowed for low enough stresses; conversely, AT2's are infinitely supported and feature α developing for every non-zero stress state. For that reason, AT1 model is often regarded as superior than the AT2 for capturing the distribution of fracture energy [30]. On the other hand, the quadratic definition of $w_{\text{PF}}(\alpha)$ in the AT2 model presents considerable numerical advantages for it inherently bounds α to be semi-positive, while AT1 requires an explicit enforcement of this condition.

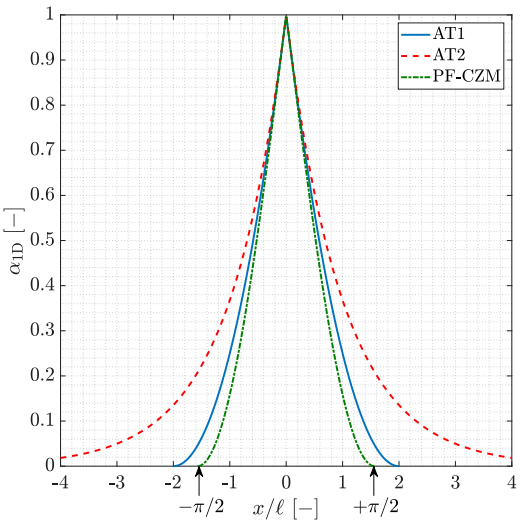

Fig. 2.2 Localized damage profiles obtained for a one-dimensional bar under uniaxial traction when using the AT1, AT2 and PF-CZM models.

The simplistic definition of $a_{\mathrm{PF}}(\alpha)$ and $w_{\mathrm{PF}}(\alpha)$ in both AT1 and AT2 models straightjackets the resulting PFM in contrast to the flexibility showcased by cohesive laws for instance. Furthermore, none of these two incorporates the tensile strength σ_C in their definition, which results instead to be a modelling artefact that depends on the regularization length and the material properties (see e.g. [64]). Towards palliating the rigidity showcased by the PFM when using the AT models, the work by Wu [63] aimed at proposing a more general definition in which: (i) σ_C and ℓ were uncoupled so as to fully recover the regularized nature of the PFM; and (ii) the fracturing behaviour could be modified to match different materials. Due to its resemblance with the renowned Cohesive Zone Model, Wu's proposal is often identified with the acronym PF-CZM. Particularly for the case of linear softening, the corresponding $a_{\mathrm{PF}}(\alpha)$, $w_{\mathrm{PF}}(\alpha)$, c_w and α_{1D} are:

$$\mathrm{PF-CZM}\ \ [63]: \begin{cases} a_{\mathrm{PF}}(\alpha) = \dfrac{\pi\ell\sigma_C^2(1-\alpha)^2}{\pi\ell\sigma_C^2(1-\alpha)^2 + 2EG_C(2\alpha-\alpha^2)} \\ w_{\mathrm{PF}}(\alpha) = 2\alpha - \alpha^2 \\ c_w = \pi \\ \alpha_{\mathrm{1D}}\left(\frac{-\pi\ell}{2} \leq x \leq \frac{\pi\ell}{2}\right) = 1 - \sin\left(\dfrac{|x|}{\ell}\right) \end{cases}, \tag{2.23}$$

where E represents the Young's modulus. As seen in Fig. 2.2 and Eq. (2.23), the PF-CZM model also showcases compact support for the one-dimensional damage bands, and so it allows purely elastic behaviour at low stresses. On the downside, the improved flexibility with respect to the aforementioned AT models comes at the cost of increased complexity. Remarkably, the definition of the generic PF-CZM's $a_{\mathrm{PF}}(\alpha)$ as a fraction (see [63]) requires special care when implementing it in a Finite Element package that features automatic differentiation, since these techniques are not inherently robust to handle $0/0$ indeterminations for instance (see [65]).

2.3.2 Strain energy decompositions

At this point, the last PFM ingredient to be defined is the strain energy density function ψ modulated by the stiffness degradation law $a_{\mathrm{PF}}(\alpha)$. For the sake of generality, ψ can be separated into two parts, one damageable ψ_D and one residual

ψ_R, as follows:

$$\psi\left(\underline{\underline{\varepsilon}}, a_{\mathrm{PF}}\right) = \psi_D\left(\underline{\underline{\varepsilon}}, a_{\mathrm{PF}}\right) + \psi_R\left(\underline{\underline{\varepsilon}}\right). \tag{2.24}$$

For pure brittle fracture, an ideal decomposition of ψ would involve ψ_D and ψ_R being exclusively associated to traction and compression states, respectively. Besides, once a crack is formed and $\psi_D = 0$, the ideal residual term ψ_R would be able to mimic the shear-free unilateral contact between crack lips. Undoubtedly, finding a variationally consistent decomposition of ψ that simultaneously fulfils all these requirements is not easy, if possible at all. Still, many strain energy decompositions have been proposed in the literature (see e.g. [52]). Among these, the most common of those fitting in the variational framework of structured deformations are hereafter presented and briefly commented. It should be noted that, since the material is always assumed linear elastic when pristine, its original strain energy density function ψ_0 is equal to:

$$\psi_0\left(\underline{\underline{\varepsilon}}\right) = \frac{1}{2}\lambda\,\mathrm{tr}\left(\underline{\underline{\varepsilon}}\right)^2 + \mu\left(\underline{\underline{\varepsilon}} : \underline{\underline{\varepsilon}}\right). \tag{2.25}$$

Standard decomposition

The first expression for $\psi(\underline{\underline{\varepsilon}}, a_{\mathrm{PF}})$ was introduced in the PFM's seminal work [23], wherein it was assumed that the stiffness degradation function a_{PF} affects all components of the straining equally. As such, it is not an energy decomposition *per se*, for it is defined as:

$$\psi_D^{\mathrm{Std}}\left(\underline{\underline{\varepsilon}}, a_{\mathrm{PF}}\right) = a_{\mathrm{PF}}\,\psi_0\left(\underline{\underline{\varepsilon}}\right), \tag{2.26}$$

$$\psi_R^{\mathrm{Std}}\left(\underline{\underline{\varepsilon}}\right) = 0. \tag{2.27}$$

Despite its simple definition and easiness of implementation, the resultant strain energy density function satisfies virtually none of the requirements listed above other than the traction and shear-free crack plane. Moreover, it predicts an unrealistic fracture behaviour that is symmetric between tensile and compressive states.

Volumetric-Deviatoric-based decompositions

On the basis of the Volumetric-Deviatoric decomposition of the strain tensor, two well-known energy splits were proposed in [50] and [49], namely the Deviatoric and Cleavage-Deviatoric decompositions (see e.g. [51]). In the former, only shear

fracture is permitted by defining ψ_D^{Dev} and ψ_R^{Dev} as:

$$\psi_D^{\text{Dev}}\left(\underline{\underline{\varepsilon}}, a_{\text{PF}}\right) = a_{\text{PF}}\left[\mu\left(\underline{\underline{\varepsilon}}_{\text{dev}} : \underline{\underline{\varepsilon}}_{\text{dev}}\right)\right], \tag{2.28}$$

$$\psi_R^{\text{Dev}}\left(\underline{\underline{\varepsilon}}\right) = \left(\frac{\lambda}{2} + \frac{\mu}{3}\right)\text{tr}\left(\underline{\underline{\varepsilon}}\right)^2. \tag{2.29}$$

where $\underline{\underline{\varepsilon}}_{\text{dev}}$ is the deviatoric part of $\underline{\underline{\varepsilon}}$. For the latter instead, shear-only fracture was limited to cases where the volumetric component of the strain was negative. Otherwise, the "total" fracture pertaining to the Standard "decomposition" was recovered. To that end, the strain tensor trace was divided into positive and negative parts per $\bullet^{\pm} = (\bullet \pm |\bullet|)/2$, each correspondingly contributing to ψ_D^{CD} and ψ_R^{CD} as:

$$\psi_D^{\text{CD}}\left(\underline{\underline{\varepsilon}}, a_{\text{PF}}\right) = a_{\text{PF}}\left[\left(\frac{\lambda}{2} + \frac{\mu}{3}\right)\text{tr}^+\left(\underline{\underline{\varepsilon}}\right)^2 + \mu\left(\underline{\underline{\varepsilon}}_{\text{dev}} : \underline{\underline{\varepsilon}}_{\text{dev}}\right)\right], \tag{2.30}$$

$$\psi_R^{\text{CD}}\left(\underline{\underline{\varepsilon}}\right) = \left(\frac{\lambda}{2} + \frac{\mu}{3}\right)\text{tr}^-\left(\underline{\underline{\varepsilon}}\right)^2. \tag{2.31}$$

Compared to the Standard model, the Cleavage-Deviatoric decomposition improves marginally the tension-compression strength asymmetry. Once fractured, it also features both shear and traction-free interaction between the crack lips. At the same time, this strain energy decomposition avoids trans-crack interpenetration in the sense of Γ-convergence [66]. As such, the residual stiffness featured by this energy decomposition tends to rigorously reproduce the sought after unilateral contact conditions between the crack lips as $\ell \to 0$.

No-Tension decomposition

Aiming at improving the insufficient strength asymmetry of the existent energy decompositions, the Theory of Structured Deformations [67] was exploited in [51] in order to obtain a PFM that, once in broken conditions, mimics the behaviour of the so-called No-Tension materials. The proposal's basic idea consists in gathering the tensile components of the strain in a structured deformation tensor $\underline{\underline{\eta}}$, so that it reduces the strain energy stored in the domain modulated by α. For a given strain state defined by $\underline{\underline{\varepsilon}}$, the corresponding structured deformation tensor $\underline{\underline{\eta}}$ is the solution

of the following minimization problem:

$$\underline{\underline{\eta}}\left(\underline{\underline{\varepsilon}}\right) = \underset{\underline{\underline{\phi}} \in \mathrm{Sym}^{+}}{\arg\min} \left(\psi_0 \left(\underline{\underline{\varepsilon}} - \underline{\underline{\phi}} \right) \right) , \tag{2.32}$$

where Sym^{+} represents the set of all symmetric and semidefinite positive tensors. Generally speaking, the pointwise resolution of Eq. (2.32) for determining $\underline{\underline{\eta}}$ renders its implementation potentially unmanageable. Nonetheless, the minimization problem above can be solved analytically for linear elastic materials since the tensors $\underline{\underline{\varepsilon}}$ and $\underline{\underline{\eta}}$ result to be coaxial for such a case [68]. Assuming without any loss of generality that the eigenvalues of a tensor follow $\bullet_1 \geq \bullet_2 \geq \bullet_3$, the corresponding closed form relation between $\underline{\underline{\varepsilon}}$ and $\underline{\underline{\eta}}$ is:

$$[\eta_1, \eta_2, \eta_3] = \begin{cases} [\varepsilon_1, \varepsilon_2, \varepsilon_3] & \text{if} \quad \varepsilon_3 \geq 0 \\ [\varepsilon_1 + \nu\varepsilon_3, \varepsilon_2 + \nu\varepsilon_3, 0] & \text{else if} \quad \varepsilon_2 + \nu\varepsilon_3 \geq 0 \\ \left[\varepsilon_1 + \dfrac{\nu\left(\varepsilon_2 + \varepsilon_3\right)}{1-\nu}, 0, 0\right] & \text{else if} \quad \varepsilon_1 + \dfrac{\nu\left(\varepsilon_2 + \varepsilon_3\right)}{1-\nu} \geq 0 \\ [0, 0, 0] & \text{else} \end{cases} , \tag{2.33}$$

and the No-Tension strain energy density function ψ^{NT} can be then defined for a generic stiffness degradation function $a_{\mathrm{PF}}(\alpha)$ as follows [52]:

$$\psi^{\mathrm{NT}}\left(\underline{\underline{\varepsilon}}, a_{\mathrm{PF}}\right) = \psi_0 \left(\underline{\underline{\varepsilon}} - (1 - \sqrt{a_{\mathrm{PF}}})\, \underline{\underline{\eta}}\left(\underline{\underline{\varepsilon}}\right) \right) . \tag{2.34}$$

From Eqs. (2.33) and (2.34) it results clear how the stiffness modulation function $a_{\mathrm{PF}}(\alpha)$ only affects ψ^{NT} whenever $\underline{\underline{\eta}}$ is not null, i.e. for tensile straining. In turn, this also means that: (i) the resultant material model presents infinite compressive strength; and (ii) even for completely broken conditions, the system retains its original compressive stiffness. Total fracture is once again recovered for sufficiently tensile conditions so that $\underline{\underline{\varepsilon}} = \underline{\underline{\eta}}$. On the downside, non-null shear stiffness is obtained in the crack planes.

2.4 Case study on the crack onset from circular holes under biaxial loadings (I)

As seen in the previous section, there exist many options regarding the PFM modelling choices, each resulting in different behaviours. Recalling that the ultimate objective of this thesis is the dynamic modelling of fracture, wherein tensile and compressive stress waves are ubiquitous, it is paramount that the PFM is ascertained to be able to deal with failure under complex multiaxial stress states. To that end, the present section conducts a thorough study on the PFM's ability to predict crack initiation from a circular hole in an infinite (or at least very large) plate under biaxial loading conditions. The resultant predictions are then put against those of the renowned Dugdale's Cohesive Zone Model (CZM) for validation. Remarkably, by just modifying the loading biaxiality, the showcased conditions upon fracture vary noticeably in terms of the pre-cracking stress field and energy release rate, making this setup a powerful contender for benchmarking failure criteria. For the sake of simplicity, the analysis is conducted under plane strain conditions and the continuum is assumed homogeneous and filled with an isotropic, linear elastic and brittle material that only cracks under tension.

2.4.1 Problem characterization

The setup herein considered is shown in Fig. 2.3a, where Σ_1 and Σ_2 represent remotely-imposed constant stresses in two perpendicular directions. Given the geometric symmetry and the material isotropy and homogeneity, the expected failure behaviour is symmetric with respect to the bisector of the first and third quadrants of the bidimensional loading space $(\Sigma_1 - \Sigma_2)$. The analysis can be thereby restricted to only considering the $\Sigma_1 \geq \Sigma_2$ loadings with no loss of generality. However, the problem definition in terms of Σ_1 and Σ_2 is not adequate for characterization because it couples the parametrization of the loading intensity and biaxiality. Previous relevant studies have instead used Σ_1 and $\beta = \Sigma_2/\Sigma_1$ to separately control those two loading characteristics [69, 70]. Nonetheless, such a choice is not convenient either since β presents an infinite discontinuity for $\Sigma_1 = 0$. To avoid this, the problem can be instead characterized in the more appropriate $(\Sigma'_1 - \Sigma'_2)$ surrogate loading space, which rotates the $(\Sigma_1 - \Sigma_2)$ baseline loading space $\pi/4$ radians clockwise (see

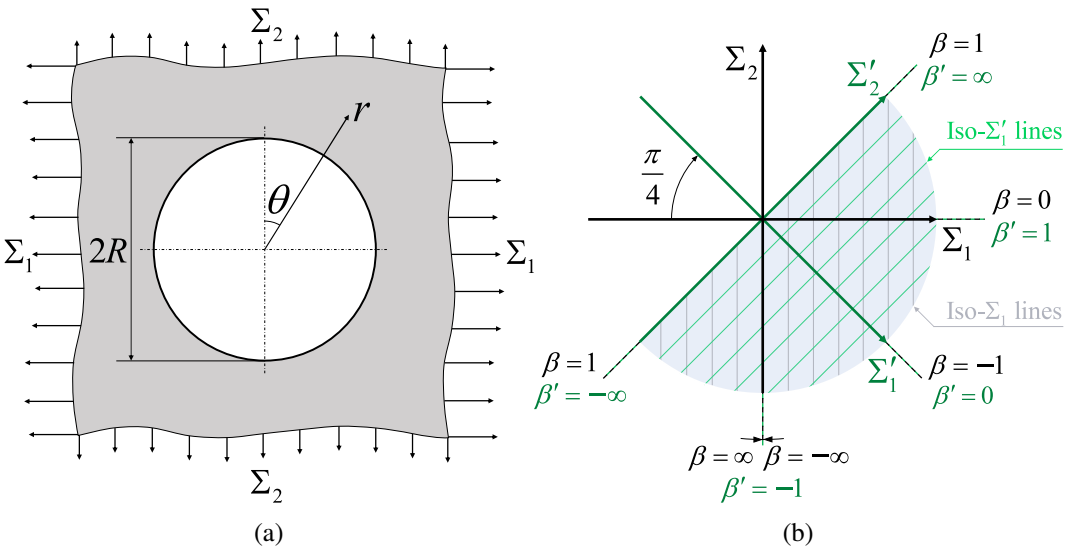

Fig. 2.3 Schematic representation of: (a) a biaxially loaded infinite plate containing a circular hole; (b) the loading subspace of interest (light blue), the baseline (black) and surrogate (green) biaxial loading spaces.

Fig. 2.3b). Mathematically, the mapping between both corresponds to the following vector rotation transformation:

$$\begin{pmatrix} \Sigma'_1 \\ \Sigma'_2 \end{pmatrix} = \frac{1}{\sqrt{2}} \begin{bmatrix} 1 & -1 \\ 1 & 1 \end{bmatrix} \begin{pmatrix} \Sigma_1 \\ \Sigma_2 \end{pmatrix} . \tag{2.35}$$

This way, all the biaxiality ratios of interest are continuously parametrized by the so-called surrogate biaxiality ratio $\beta' = \Sigma'_2/\Sigma'_1 \,|\, \beta' \in (-\infty, \infty)$, which relates to β as:

$$\beta' = \frac{1+\beta}{1-\beta}; \quad \beta = \frac{-1+\beta'}{1+\beta'} . \tag{2.36}$$

Additionally, Σ'_1 remains semi-positive for $\Sigma_1 \geq \Sigma_2$ so that the sign analysis of relevant magnitudes simplifies considerably in the surrogate loading space. From a physical perspective, the change of coordinates entails that loading biaxiality is achieved by superposing pure shear and plane hydrostatic states governed by Σ'_1 and Σ'_2, respectively. As such, $\beta' = \pm\infty$ represent either uniform bi-tension or bi-compression states; $\beta' = \pm 1$ stand for either uniaxial tension or compression; and $\beta' = 0$ corresponds to pure shear conditions.

The well-known exact solution of the stress field around a hole embedded in an uniaxially tensioned infinite plate was given in [71]. Using the superposition principle

and taking Σ_1' and β' as the loading parameters, the pre-crack stress components for the case at hand result as follows:

$$\sigma_{rr}\left(r,\,\theta,\,\Sigma_1',\beta'\right)=\frac{\Sigma_1'}{\sqrt{2}}\left\{\beta'\left[1-\left(\frac{R}{r}\right)^2\right]+\right.$$
$$\left.+\left[1-4\left(\frac{R}{r}\right)^2+3\left(\frac{R}{r}\right)^4\right]\cos 2\theta\right\}=\Sigma_1'\,S_{rr}'(r,\,\theta,\,\beta')\,, \tag{2.37}$$

$$\sigma_{\theta\theta}\left(r,\,\theta,\,\Sigma_1',\beta'\right)=\frac{\Sigma_1'}{\sqrt{2}}\left\{\beta'\left[1+\left(\frac{R}{r}\right)^2\right]+\right.$$
$$\left.+\left[1+3\left(\frac{R}{r}\right)^4\right]\cos 2\theta\right\}=\Sigma_1'\,S_{\theta\theta}'(r,\,\theta,\,\beta'), \tag{2.38}$$

$$\tau_{r\theta}\left(r,\,\theta,\,\Sigma_1'\right)=\frac{\Sigma_1'}{\sqrt{2}}\left[1+2\left(\frac{R}{r}\right)^2-3\left(\frac{R}{r}\right)^4\right]\sin 2\theta=\Sigma_1'\,S_{r\theta}'(r,\,\theta)\,. \tag{2.39}$$

Clearly, both σ_{rr} and $\sigma_{\theta\theta}$ are maximized for $\theta=\{0,\,\pi\}$ when $\Sigma_1'>0$, whereas $\tau_{r\theta}$ is null along these two azimuths. Therefore, fracture is expected to develop along the directions $\theta=\{0,\,\pi\}$ and in pure Mode I.

By virtue of Irwin's relation [3], the energetic balance upon fracture can be fully characterized by means of only the Mode I Stress Intensity Factor K_I. Analytical estimates of K_I for a single radial crack along $\theta=0$ or $\theta=\pi$ (asymmetric cracking) and for two antipodal twin cracks along $\theta=0$ and $\theta=\pi$ (symmetric cracking) can be found in [69]. Nonetheless, the latter breakage mechanism is more energetically convenient since the corresponding K_I is higher for equal single-crack length a. Therefore, symmetric cracking as represented in Fig. 2.4 is expected for every case here studied. Likewise, the corresponding expression for K_I is as in Eqs. (2.40) to (2.43), where $\xi=a/\left(a+R\right)$.

$$K_I\left(a,\,\Sigma_1',\,\beta'\right)=\Sigma_1'\sqrt{\pi a}\,F_{\beta'}\left(a,\,\beta'\right) \tag{2.40}$$

$$F_{\beta'}\left(a,\,\beta'\right)=\sqrt{2}\left[F_0(\xi)+\frac{\beta'-1}{2}\,F_1(\xi)\right] \tag{2.41}$$

$$F_0(\xi)=0.5\,(3-\xi)\left[1+1.243\,(1-\xi)^3\right] \tag{2.42}$$

$$F_1(\xi)=1+(1-\xi)\left[0.5+0.743\,(1-\xi)^2\right] \tag{2.43}$$

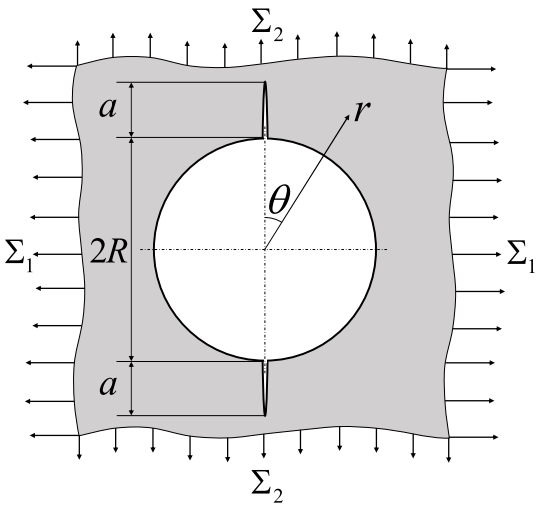

Fig. 2.4 Schematic representation of the symmetric cracking stemming from a circular hole in a biaxially loaded plate.

Expressions above show that the loading biaxiality can considerably change the conditions for fracture in terms of the stress and energy release rate. Particularly, Table 2.1 details the ranges of β' leading to different sign and trend evolutions of the hoop stress $\sigma_{\theta\theta}$ along r with $\theta = \{0, \pi\}$, as well as of K_I with respect to a. Therein, $+$ or $-$ signs stand for traits of positive or negative function values, whereas $\nearrow$ or $\searrow$ represents increasing or decreasing trends. Likewise, the sequence of symbols from left to right indicate the evolution of the considered characteristic as either r or a grows. For the sake of clarity, Table 2.1 is graphically complemented by the plots in Fig. 2.5.

Table 2.1 Dependence of $\sigma_{\theta\theta}$ and K_I with β'

$\boldsymbol{\sigma_{\theta\theta}}$				$\boldsymbol{K_I}$			
$\boldsymbol{\beta'}$ **ranges**	**Sign**	**Trend**	**Tag**	$\boldsymbol{\beta'}$ **ranges**	**Sign**	**Trend**	**Tag**
$(-\infty, -6)$	$-$	$\nearrow$	A1	$(-\infty, -2)$	$-$	$\searrow$	B1
$(-6, -2)$	$-$	$\searrow\nearrow$	A2	$(-2, -1)$	$+-$	$\nearrow\searrow$	B2
$(-2, -1)$	$+-$	$\searrow\nearrow$	A3	$(-1, -0.194)$	$+$	$\nearrow\searrow\nearrow$	B3
$\left(-1, 6-4\sqrt{3}\right)$	$+-+$	$\searrow\nearrow$	A4	$(-0.194, \infty)$	$+$	$\nearrow$	B4
$\left(6-4\sqrt{3}, 0\right)$	$+$	$\searrow\nearrow$	A5				
$(0, \infty)$	$+$	$\searrow$	A6				

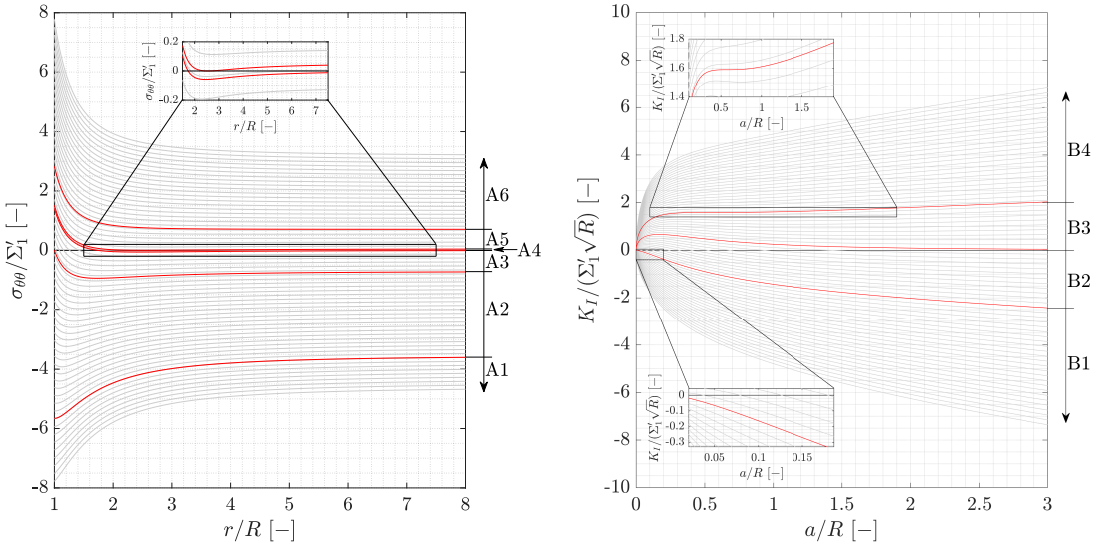

(a) (b)

Fig. 2.5 Graphic representation of the dependence on β' of: (a) $\sigma_{\theta\theta}$ and (b) K_I.

2.4.2 Implementation of the Phase Field fracture model

The numerical implementation of the PFM in a Finite Element context was performed in the Open Source computational framework FEniCSx [72–76]. The original setup defined in Fig. 2.3a was modified according to Figs. 2.6. Geometry-wise, this consisted in relaxing the original hypothesis of an infinitely large plate to just being considerably larger than the hole (at least $L/R \sim 40$). The setup's vertical symmetry was also exploited to reduce the computational cost while keeping the prospective crack far from the model boundaries. On the other hand, the original Neumann boundary conditions were substituted by Dirichlet ones to avoid issues in the quasi-static resolution upon fracture-caused softening. Only for infinite domains such a change is rigorous in the sense of not affecting the resultant predictions. However, given that $L >> R$, it is still deemed a reasonable approximation herein. Values of the remote stresses at failure Σ_{1f} and Σ_{2f} were then computed out of the corresponding reaction forces right before the "instant" of crack onset, i.e. whenever α reached a close-to-one threshold anywhere in Ω. To ensure capturing properly the localization bands of α, the mesh was refined in the prospective cracking regions so that the characteristic element size was $\ell/7$ therein.

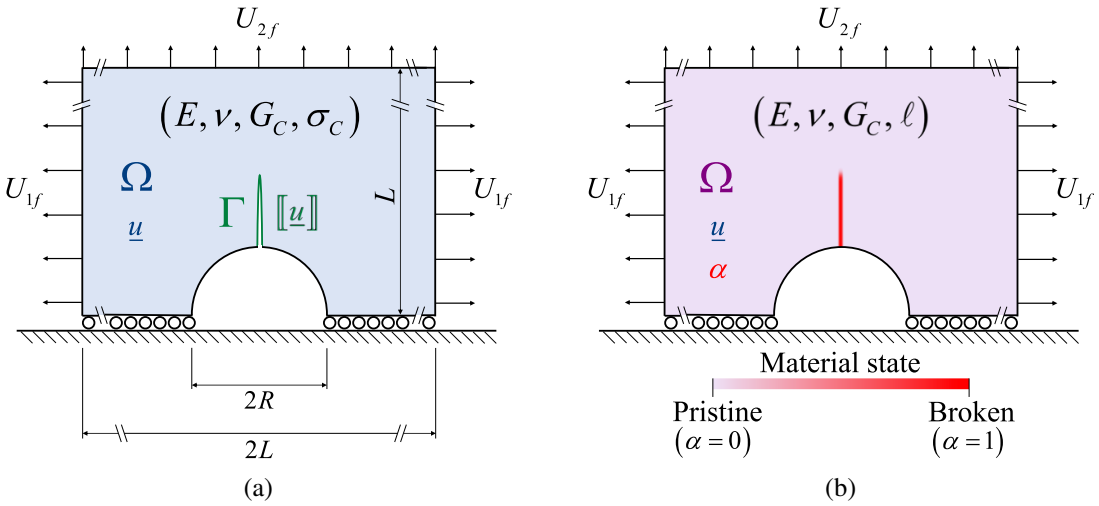

Fig. 2.6 Crack onset in a biaxially loaded large plate containing a circular hole: (a) Schematic descriptions of the actual failure event and (b) of the PFM approximation.

The PFM resolution algorithm used was iterative on two levels: on one hand, the prescribed displacements were gradually increased at each time step up to the failure onset; on the other, the staggered principles were alternatively minimized until convergence was achieved. Such a condition was assessed at the end of each alternate minimization iteration through two different ideally-vanishing L2-norms: (i) that of the variation in α with respect to the previous iteration, and (ii) that of the displacement problem residual upon substitution of the latest estimates for the $\underline{u}$ and α fields. For more details on this resolution algorithm, please refer to Appendix A.

Moreover, all simulations were herein conducted using the AT1 model so as to avoid both AT2's lack of linear elastic behaviour for low stresses and the numerical difficulties of implementing the PF-CZM. Regarding the strain energy decompositions instead, only the Standard and the No-Tension proposals were considered: the former provides the reference for total fracture, while the latter is the most promising choice for modelling only-tensile cracking. For the sake of conciseness, the Deviatoric and Cleavage-Deviatoric decompositions were herein neglected for their marginal improvement in the strength asymmetry with respect to the Standard model.

For the AT1 model, the intrinsic strength can be determined from the loss of stability of the corresponding PFM's homogeneous solution [26]. For instance,

considering the Standard decomposition and a plain ($R = 0$) biaxially loaded domain, one gets the following elliptical-shaped intrinsic locus of failure states:

$$\Sigma'_{1f}(\beta')\big|^{\text{Std}}_{R=0} = \sqrt{\frac{3G_C E}{8\ell\,(1+\nu)}\frac{1}{1+(1-2\nu)\,\beta'^2}}\,, \tag{2.44}$$

where it holds that $\Sigma'_2 = \beta'\Sigma'_1$. Particularizing Eq. (2.44) to uniaxial traction conditions ($\beta' = 1$, see Fig. 2.3b) yields the corresponding apparent tensile strength $\sigma_C^{\text{Std}} = \sqrt{3G_C E/\left[8\ell\,(1-\nu^2)\right]}$ after reverting the transformation in Eq. (2.35). For the No-Tension decomposition instead, the expression for $\Sigma'_{1f}(\beta')\,|^{\text{NT}}_{R=0}$ writes as:

$$\Sigma'_{1f}(\beta')\big|^{\text{NT}}_{R=0} = \begin{cases} \sqrt{\dfrac{3G_C E}{8\ell\,(1+\nu)}\dfrac{2\,(1-\nu)}{(1-2\nu)\,(1+\beta')^2}} & \text{if } -1 \le \beta' < \dfrac{1}{1-2\nu} \\ \sqrt{\dfrac{3G_C E}{8\ell\,(1+\nu)}\dfrac{1}{1+(1-2\nu)\,\beta'^2}} & \text{if } \dfrac{1}{1-2\nu} \le \beta' \le \infty \end{cases}, \tag{2.45}$$

and the corresponding model-dependent apparent tensile strength is $\sigma_C^{\text{NT}} = \sqrt{3G_C E\,(1-\nu)\,/\left[8\ell\,(1+\nu)\,(1-2\nu)\right]}$, which is always larger than σ_C^{Std}. It results evident from Eqs. (2.44) and (2.45) that the No-Tension decomposition also features total fracture for $\beta' \ge 1/(1-2\nu)$, and so its intrinsic failure locus is piecewise elliptical. Besides those cases, the corresponding failure locus straightens so that it coincides with the vertical line $\Sigma_{1f} = \sigma_C^{\text{NT}}$ in the baseline loading space $(\Sigma_1 - \Sigma_2)$. Furthermore, Eq. (2.45) is smooth all along, meaning that the elliptical trait is tangent to the vertical one at $\beta' = 1/(1-2\nu)$. Lastly, no failure is foreseen by the No-Tension decomposition for purely compressive straining states, i.e. when $\beta' < -1$.

In view of the regularization nature of the PFM, the set $(E,\, \nu,\, G_C,\, \ell)$ of properties and parameters was herein kept constant; hence, the apparent tensile strength σ_C and the plane strain Irwin's length $l_{ch} = G_C E/\left[(1-\nu^2)\sigma_C^2\right]$ were dependent on the energy decomposition used. Table 2.2 reports the particular numerical values used for the PFM simulations, which mostly correspond to those used in [64] for PMMA.

Results in Fig. 2.7a correspond to the PFM simulations under uniaxial tensile conditions ($\beta' = 1$), and they show that the Standard and the No-Tension decompositions predict an almost identical normalized transition from holeless ($\Sigma_{1f}/\sigma_C^i = 1$)

Table 2.2 Material properties and modelling parameters used for the Phase Field simulations.

E	ν	G_C	ℓ	σ_C^{Std}	l_{ch}^{Std}	σ_C^{NT}	l_{ch}^{NT}
[MPa]	[−]	[MPa · mm]	[mm]	[MPa]	[mm]	[MPa]	[mm]
2300	0.3	0.461	0.025	132.20	0.067	146.32	0.054

to large hole ($\Sigma_{1f}/\sigma_C^j = 1/3$) failure regimes. Note that the superindices of σ_C and l_{ch} indicate the use of different normalizations for each decomposition. Anyhow, these results highlight that for predominantly tensile conditions, decomposing the strain energy density becomes significantly less important.

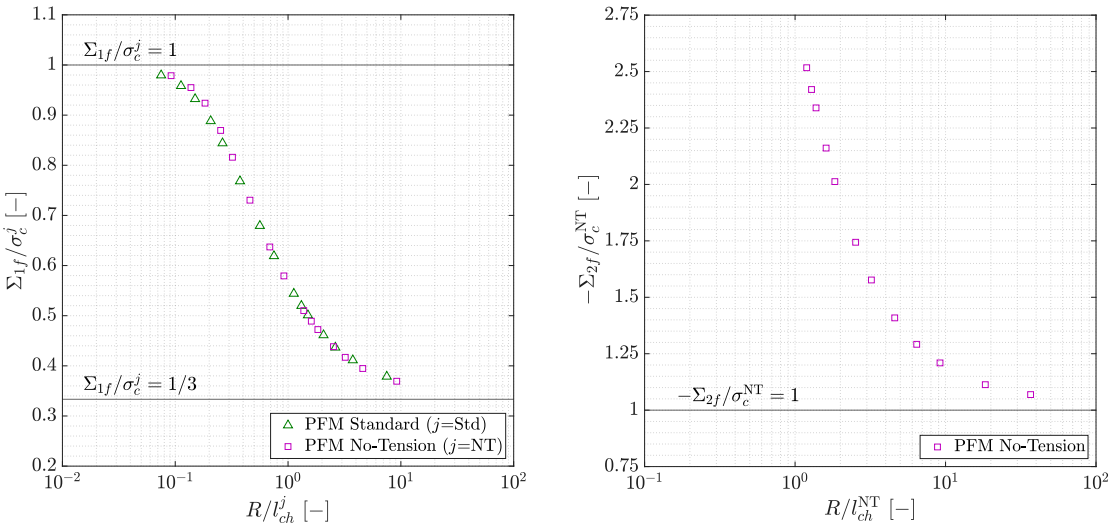

(a) (b)

Fig. 2.7 Crack onset predictions by the PFM for: (a) uniaxial tension, and (b) uniaxial compression loadings.

For uniaxial compression ($\beta' = -1$) instead, proper decomposition of the strain energy is required to avoid unrealistically predicting failure in compressed regions. Due to this, only the No-Tension decomposition is implemented for that loading, and the resultant predictions are shown in Fig. 2.7b. Regarding the failure size-effect, it results that $\Sigma_{2f}/\sigma_C \approx -1$ for very large holes, and this ratio monotonically increases in absolute value as R decreases. For $R \lesssim l_{ch}^{\text{NT}}$ however, the occurrence of crack onset was no longer clearly identifiable since it became dependent of the numerical threshold for α used to acknowledge crack onset. Such an occurrence might be

attributed to a shielding effect in the development of α for small enough values of R, which causes the tensioned region to become of the order of magnitude of the regularization length ℓ.

Failure onset predictions under biaxial loadings are then reported in Figs. 2.8 for the Standard and No-Tension decompositions. Such graphs represent biaxial safety domains, and as such must be read radially: for a given origin-centred spoke the biaxiality ratio is constant, and the loading states are safe if they are closer to the origin than the corresponding failure point $(\Sigma_{1f}, \Sigma_{2f})$. Therefore, the previous plots in Figs. 2.7a and 2.7b can be seen as curves resulting from the intersection between the R-dependent safety domains and the radial directions corresponding to $\beta' = 1$ and $\beta' = -1$, respectively.

The elliptical shape of the $R = 0$ safety domain showcased by the Standard decomposition, i.e. its intrinsic failure locus, reveals evident in Fig. 2.8a. The increase of R eventually turns the safety domains spear-shaped, thus tending to what predicted by a maximum tensile stress criterion. It is noteworthy that the sharp angle of the safety domain at $\beta' \to \infty$ for large holes is due to the change in the azimuths along which cracking occurs, abruptly switching from $\theta = \{0, \pi\}$ when $\Sigma_{1f} > \Sigma_{2f}$ to $\theta = \{\pi/2, 3\pi/2\}$ when $\Sigma_{1f} > \Sigma_{2f}$. Given the large value of R, these two fracture mechanisms are independent and the overall crack onset is obtained as the minimum of the corresponding failure loads, hence the non-smooth safety domain. On the other hand, this independence eventually vanishes as R is reduced, and the abrupt transition is observed to turn smooth when $R/l_{ch}^{\mathrm{Std}} \lesssim 0.5$. It is to be noted that only the predictions for $\beta' > 0$ are shown in Fig. 2.8a since otherwise failure onset would be unrealistically predicted to occur in regions under compression.

For the No-Tension decomposition instead, Fig. 2.8b reveals that spear-shaped safety domains are mostly showcased for every hole size, although with a blunt elliptical "tip" for small values of R. Of course, such a shape is better aligned with tensile dominated fracture than the previous one. Likewise, the above mentioned shielding effect for compression loadings and small holes was observed, whenever $\beta \lesssim -0.7$, for the two smallest values of R considered, namely $R/l_{ch}^{\mathrm{NT}} = 0.014$ and $R/l_{ch}^{\mathrm{NT}} = 0.046$. Consequently, such a phenomenon cannot be exclusively blamed on the fact that the tensioned region vanishes, since this only occurs for $\beta' < 6 - 4\sqrt{3} \approx -0.93$. Another potential culprit for this shielding effect can be found in the non-monotonous evolution of $K_I(a)$ observed for $\beta' < -0.194$, so that

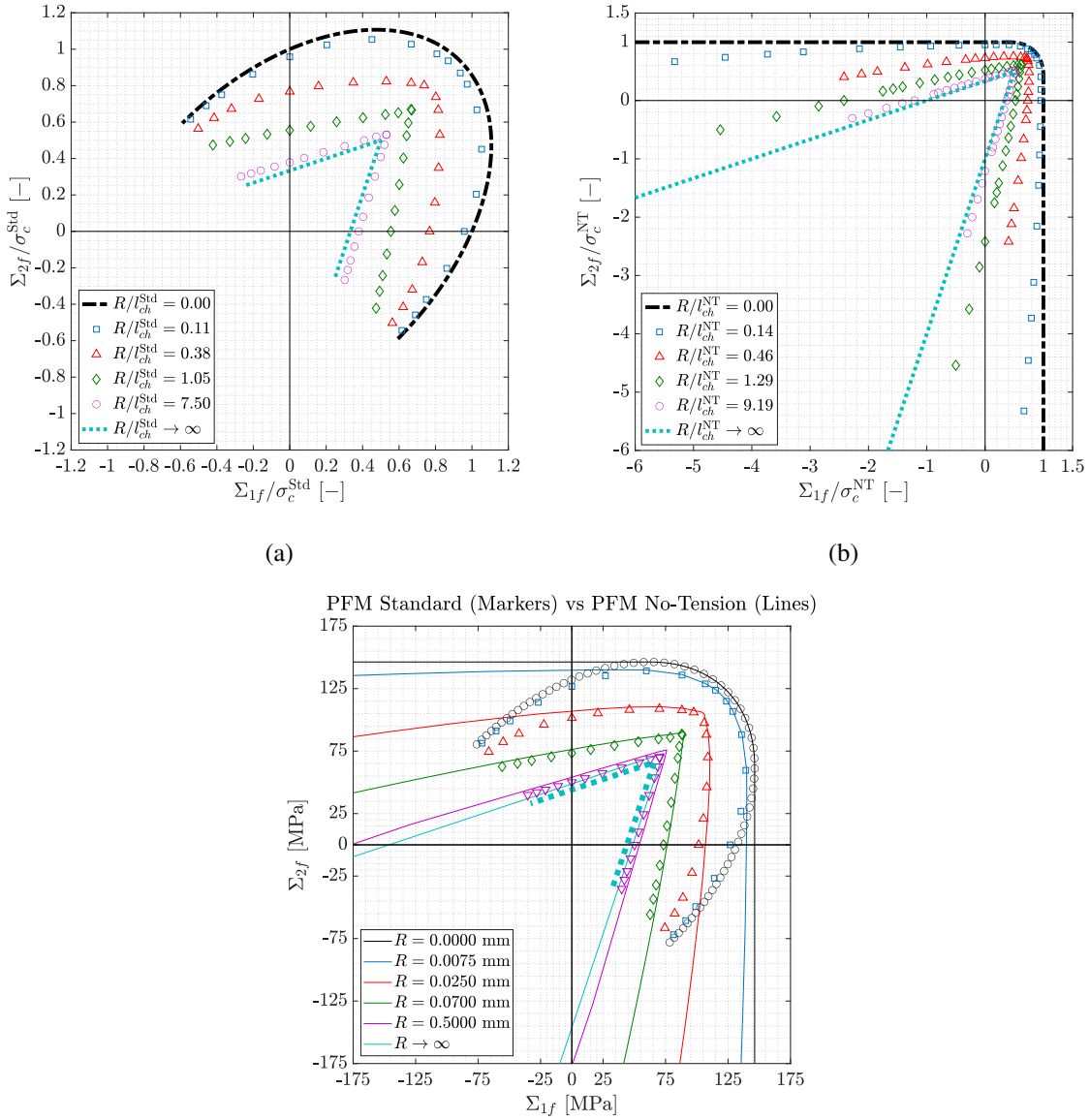

Fig. 2.8 Biaxial safety domains predicted by PFM with: (a) the Standard, (b) the No-Tension, and (c) both decompositions. Matching colours imply same hole radius.

its decreasing trait chokes the development of α for small enough holes and does not allow the regularized crack to onset properly.

Lastly, a direct comparison between the dimensional safety domains predicted by the Standard and the No-Tension decompositions is given in Fig. 2.8c. Upon

sufficiently tensile conditions and small enough holes, both are shown to yield almost identical predictions. As the compressive states gain importance, the two sets of predictions rapidly diverge in the case of small to intermediate hole sizes, yet they remain close for large holes. For these latter cases it holds that $R >> \ell$, which causes the PFM solution to be mainly governed by the tensile hoop stress in the vicinity of the crack onset points, i.e. $\sigma_{\theta\theta}(r = R, \theta = \{0, \pi\})$. This, combined with a radial stress component σ_{rr} that vanishes therein, causes the total and tensile-only fracture behave quite similarly. Indeed, the slight difference observed between the two $R \to \infty$ safety domains is due to σ_C^{NT} being approximately 10% larger than σ_C^{Std} as per Table 2.2.

2.4.3 Implementation of Dugdale's Cohesive Zone Model and results comparison

As proposed in [77], Dugdale's Cohesive Zone Model (CZM) [14] admits a semi-analytical implementation in terms of the failure load and the process zone length. By virtue of the Paris' integral [78], it was demonstrated in [79] that such implementation can be undertaken purely in terms of three Mode I Stress Intensity Factors K_I: one corresponding to the setup under study, plus other two auxiliary cases herein named as Constant Stress Lip (CSL) and Line-Load Edge (LLE) loadings. For the case at hand, these two latter loading scenarios particularize as schematically shown in Figs. 2.9.

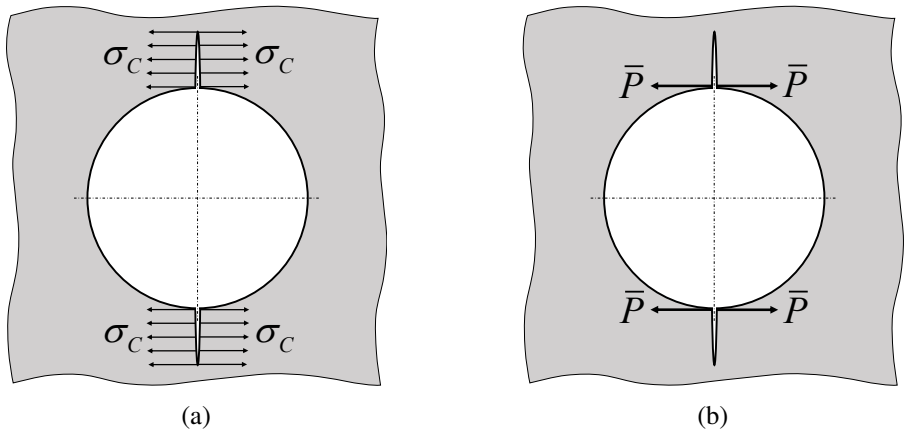

Fig. 2.9 Schematic representations of the (a) Constant Stress Lip and (b) Line-Load Edge auxiliary loading scenarios.

For the CSL loading case, the following approximated expression for $K_I^{\sigma_C}$ was given in [69]:

$$K_I^{\sigma_C}(a, \sigma_C) = \sigma_C \sqrt{\pi a}\, F_{\sigma_C}(a) \,, \tag{2.46}$$

$$F_{\sigma_C}(a) = 1 + (1-\xi)\left[-0.137 + 0.258\,(1-\xi)^2 - 0.4\xi^2\,(1-\xi)\right] . \tag{2.47}$$

For the LLE loading scenario, the approximated expression for $K_I^{\bar{P}}$ was determined through the interpolation between its known values for the limit cases of an edge and a Griffith crack [80], resulting in:

$$K_I^{\bar{P}}(a, \bar{P}) = \frac{\bar{P}}{\sqrt{\pi a}} F_{\bar{P}}(a) \,, \tag{2.48}$$

$$F_{\bar{P}}(a) = 2.594 \left(\frac{R}{R+5a}\right)^2 + 2\left[1 - \left(\frac{R}{R+5a}\right)^2\right] . \tag{2.49}$$

Upon combination of the three different Mode I Stress Intensity Factors defined in Eqs. (2.40) to (2.43) and in Eqs. (2.46) to (2.49), CZM's semi-analytical implementation consists in solving the system of two equations in Eq. (2.50). The two unknowns are the process zone length a_p and the failure load Σ_1'. For the sake of convenience, the numerical implementation is done in the $(\Sigma_1' - \Sigma_2')$ surrogate loading space, while the $(\Sigma_1 - \Sigma_2)$ baseline loading space is used for graphical representations.

$$\text{CZM:} \begin{cases} \dfrac{\Sigma_{1f}'}{\sigma_C} = \dfrac{F_{\sigma_C}(a_{p,f})}{F_{\beta'}(a_{p,f}, \beta')} & \text{(2.50a)} \\[2ex] \dfrac{\Sigma_{1f}'}{\sigma_C} = \dfrac{l_{ch} + 2\displaystyle\int_0^{a_{p,f}} F_{\sigma_C}(a)\, F_{\bar{P}}(a)\, \mathrm{d}a}{2\displaystyle\int_0^{a_{p,f}} F_{\beta'}(a, \beta')\, F_{\bar{P}}(a)\, \mathrm{d}a} & \text{(2.50b)} \end{cases}$$

Eq. (2.50a) results from imposing the Stress Intensity Factor to be null for any cohesive crack of length a_p. Using the superposition principle, such condition is equivalent to determining the crack length $a = a_p$ for which $K_I(a_p) = K_I^{\sigma_C}(a_p)$. Therefore, for a given loading intensity Σ_1', Eq. (2.50a) determines the corresponding length of the process zone a_p. On the other hand, Eq. (2.50b) imposes that the opening displacement at the mouth of the process zone $(r = R)$ is equal to the critical value G_C/σ_C at the instant of failure. As such, simultaneous fulfilment of these two

equations yields the CZM predictions for the failure load Σ'_{1f} and the critical process zone length $a_{p,f}$.

The safety domains predicted by CZM are shown in Fig. 2.10 alongside those of the PFM with the No-Tension energy decomposition. For the latter set of results, failure stresses and hole radii are normalized with σ_C^{NT} and l_{ch}^{NT}, respectively. This comparison shows that, despite the intrinsic differences between the PFM and the CZM, a proper choice of the former's energy decomposition leads to failure onset predictions that match nicely those of the later in a wide range of failure conditions. Remarkably, the curved shape of PFM's safety domains for $R \sim 0$ and $\beta' \to \infty$ is in better agreement with experimental evidence than CZM's quasi-right angle [81, 82].

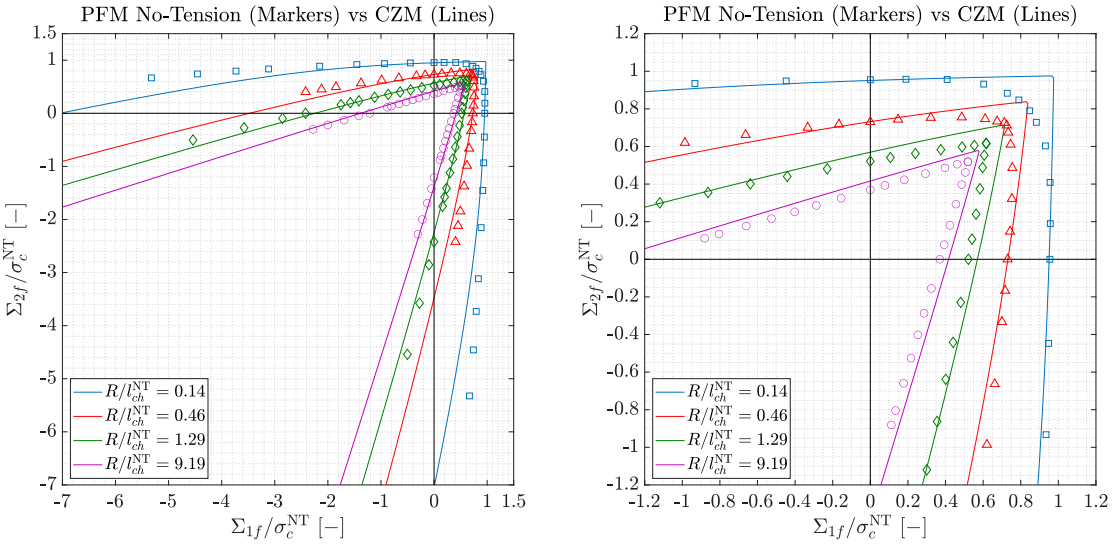

(a) (b)

Fig. 2.10 (a) Comparison of the safety domains predicted by the PFM No-Tension and the CZM, and (b) close-up centred at the loading space origin.

2.5 Conclusions

The Phase Field fracture model was comprehensively described herein in a quasi-static context. After a constant development spanning ever since the introduction of the variational approach to brittle fracture, this framework has proven to be theoretically robust and versatile. Its variational nature and continuous primary

fields allows for straightforward numerical implementation in the context of Finite Elements, unlike many other approaches to fracture. Likewise, the wide range of modelling choices available allows for replicating several fracturing behaviours. All of these advantages have lately rendered the Phase Field modelling of fracture one of the main cornerstones of the computational Fracture Mechanics community.

Specifically, it was herein proven that for the comprehensive benchmark study on the crack onset from a circular hole under biaxial loading conditions, the Phase Field fracture model is able to yield crack onset predictions matching those of the well established Dugdale's Cohesive Zone Model when the former uses the No-Tension energy decomposition and the AT1 model. This is of great importance for the present thesis, for it covers the modelling of dynamic fracture wherein the mechanical information is spread through waves that lead to complex combinations of traction and compression stress states. Hence, this chapter served not only to introduce the underlying concepts behind the Phase Field fracture model, but also to pre-emptively assess the existent modelling choices with view to a subsequent implementation in dynamic contexts.

Chapter 3

Dynamic Phase Field fracture model[1]

3.1 Introduction

Although the Phase Field fracture model was initially conceptualized as a regularized variational framework for quasi-static fracture (see e.g. [46, 47]), its energy-based definition allows for easily incorporating the inertial effects in the governing principles. Hence, the resultant dynamic Phase Field fracture model can inherit the previously discussed advantages of the quasi-static counterpart, while having its applicability extended to a much broader range of conditions. Among the many strengths of the Phase Field fracture model, its ability to inherently reproduce complex fracture phenomena results of special importance in a dynamic context, where the branching, coalescence and kinking of cracks commonly occur, and the propagating pressure waves often lead to complex tensile-compressive stress states.

In this regard, the first relevant developments of the dynamic Phase Field fracture model can be found in the complementary works by Bourdin, Larsen and co-Authors [27, 28]. These eminently fundamental studies managed to prove that their proposed time-discretized dynamic Phase Field fracture model converges to the continuous solution as the temporal discretization gets finer, and so the total energy in the system is asymptotically conserved. Likewise, simple numerical experiments were conducted for show that the dynamic Phase Field fracture model can reproduce some

[1] Part of the work described in this chapter has been published in: Chao Correas, A., Reinoso, J., Cornetti, P., Corrado, M. (2024). On the (lack of) representativeness of quasi-static variational fracture models for unstable crack propagation. *J Mech Phys Solids* 186, 105573.

experimentally observed aspects of fast-propagating fracture, such as the dynamic cracks branching or the upper bounded crack tip velocity.

Leaving the purely theoretical aspects aside and striding for an algorithmically convenient formulation instead, two similar but independent proposals derived the governing principles for the dynamic PFM from the Euler-Lagrange equations [83, 84]. Analogously to the resolution procedure introduced for the quasi-static Phase Field fracture model [24], both approaches strongly imposed the irreversibility condition through the use of history variables. Likewise, the monotonic resolution of the coupled motion/damage governing principle was therein dropped in favour of a staggered scheme. The obtained simulation results were once again reported to reproduce complex dynamic crack propagation phenomena without the need of ad-hoc criteria. Another heuristic dynamic PFM was proposed in [85], where the staggered governing equations were derived from the "reversible" Hamilton's principle and the irreversibility of fracture was strongly imposed through Dirichlet boundary conditions, which applied wherever the phase field reached a certain threshold.

Going back to rigorous formalisms, the use of variational inequalities to account for the irreversibility of fracture within the context of Hamilton's principle was initially proposed in [86] and further developed in [29]. This methodology allowed for a theoretically robust representation of dynamic fracturing events, yet at the cost of increased complexity implementation-wise. The computational cost of resolving the numerical problem was also thoroughly heeded therein, and advanced techniques such as parallel computing were successfully exploited in an aim to render the approach more applicable. Overall, the authors concluded that the variational-inequality-based dynamic Phase Field fracture model could indeed be practical to investigate real dynamic brittle fracture.

Thereafter, many studies have delved into the capability of the Phase Field fracture model to reproduce and provide insights concerning different aspects of dynamic fracture. For instance, crack microbranching in glass-like materials was thoroughly studied in [31], eventually concluding that it is primarily a 3D instability effect. Furthermore, the evolution of the crack tip velocity in a dynamic fracturing process was extensively investigated in [30] under linear elastic and brittle assumptions. Therein, it was reported that the dynamic Phase Field fracture model is able to capture the well-known apparent toughening for increasing crack tip velocities, it being the

main responsible for the observed dynamic branching once a critical value of energy release rate is reached. Different theoretical and algorithmic aspects of simulating cohesive dynamic fracture with the Phase Field fracture model were covered in [87], including case studies on the Kalthoff–Winkler experiments [88] or the stochastic fragmentation of a thick cylinder. Likewise, the inclusion of hydrogen embrittlement considerations into the dynamic Phase Field fracture model was explored in [89], proving that higher material brittleness favours increased dynamic crack branching. Dropping the assumption of linear elasticity, the dynamic fracturing of pre-strained hyperelastic materials was instead studied in [32], and a novel dynamic Phase Field fracture model formulation was proposed on the basis of modifying how the kinetic energy interacts with the phase field. Using this new approach, the dynamic Phase Field fracture model could be implemented for non-linear materials where the conventional formulation was reported to not function properly. Besides, the authors were able to reproduce complex experimental findings observed in non-linear brittle gels, such as the ultra-high-velocity oscillation. Lastly, aiming at the study of failure in composite glass structures, the interaction between dynamic bulk fracture and cohesive interfaces was studied in [90], showing the tight interrelation between both phenomena and the resultant crack patterns obtained.

In this context, the present chapter will be devoted to developing the conventional formulation of the dynamic Phase Field fracture model, and then couple it with an explicit time integrator. The resultant numerical approach will then be utilized for studying the phenomena of fragmentation in a biaxially pre-strained 2D glass pane that is punched in the middle. In particular, the effect of the pre-straining intensity and biaxiality will be depicted in detail, showing that indeed the dynamic Phase Field fracture model is inherently able to capture very complex crack phenomena.

3.2 The dynamic Phase Field fracture model

Let us now recall the quasi-static PFM presented in the previous chapter and, following the developments in [29], generalize it to the dynamic context in Fig. 3.1. In order to account for the inertial effects, the mass density ρ is required in addition to the aforementioned properties and parameters, i.e. E, ν, G_C, σ_C and ℓ. Besides, dropping the quasi-static hypothesis allows t to retrieve its physical meaning as the actual temporal coordinate of the time-dependent evolution.

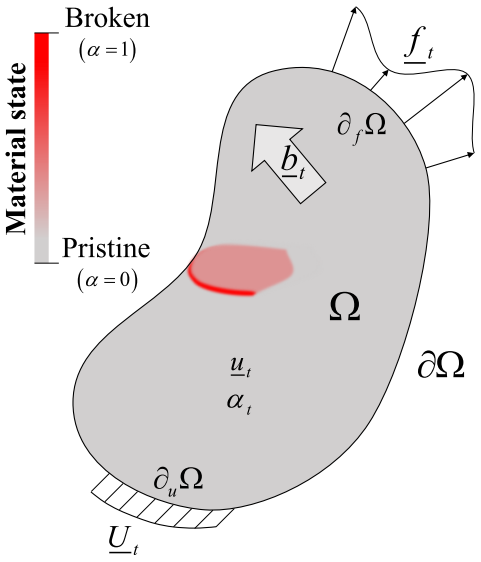

Fig. 3.1 Illustration of the Phase Field approximation to a generic dynamic fracture problem.

Differently from the quasi-static PFM, the dynamic counterpart can deal with non-null prescribed forces without any issue. Therefore, the energy of the structural system now includes the kinetic $\mathscr{K}$, strain $\mathscr{E}_{\text{str}}$ and fracture $\mathscr{E}_{\text{frac}}$ components, as well as the work done by the prescribed external forces $\mathscr{W}_{\text{ext}}$. Mathematically, each of these terms gets defined as:

$$\mathscr{K}\left(\dot{\underline{u}}_t, t\right) = \frac{1}{2}\int_{\Omega} \rho\, \dot{\underline{u}}_t \cdot \dot{\underline{u}}_t \,\mathrm{d}\underline{x}, \tag{3.1}$$

$$\mathscr{E}_{\text{str}}(\underline{u}_t, \alpha_t) = \int_{\Omega} \psi\Big(\underline{\underline{\varepsilon}}(\underline{u}_t), a_{\text{PF}}(\alpha_t)\Big)\,\mathrm{d}\underline{x}, \tag{3.2}$$

$$\mathscr{E}_{\text{frac}}(\alpha_t) = \int_{\Omega} \frac{G_C}{c_w}\left(\frac{w_{\text{PF}}(\alpha_t)}{\ell} + \ell\,\nabla\alpha_t \cdot \nabla\alpha_t\right)\mathrm{d}\underline{x}, \tag{3.3}$$

$$\mathscr{W}_{\text{ext}}(\underline{u}_t, t) = \int_{\Omega} \underline{b}_t \cdot \underline{u}_t \,\mathrm{d}\underline{x} + \int_{\partial_f\Omega} \underline{f}_t \cdot \underline{u}_t \,\mathrm{d}\underline{x}, \tag{3.4}$$

where $\dot{\underline{u}}$ stands for the velocity field, and the acceleration field will be instead represented by $\ddot{\underline{u}}$. As introduced in the previous chapter, the admissibility condition for the fields $\underline{u}_t$ and α_t can be weakly imposed by forcing them to belong to the sets V_t and B_t, respectively (see Eqs. (2.11) and (2.12)). Furthermore, since $\dot{\underline{u}} = \mathrm{d}\underline{u}/\mathrm{d}t$ and $\ddot{\underline{u}} = \mathrm{d}^2\underline{u}/\mathrm{d}t^2$, if $\underline{u}_t$ is admissible so are the associated velocity and acceleration fields from a theoretical standpoint. On the other hand, Hamilton's principle states that for any dynamic evolution along the time interval $T = [0, t']$, the admissible

variations $\delta\underline{u}$ and $\delta\alpha$ belong to the evolution spaces V_0^T and B_0^T defined in Eqs. (3.5) and (3.6), respectively. It is to be noted that ∂T represents the extrema of T, i.e. the instants $t = 0$ and $t = t'$.

$$\mathrm{V}_0^T = \left\{ \delta\underline{u} : \Omega \times T \to \mathbb{R}^N \;\middle|\; \begin{array}{l} \delta\underline{u} = \underline{0} \;\; \forall \underline{x} \times t \in \partial_u \Omega \times T \;\; \text{and} \\ \delta\underline{u} = \underline{0} \;\; \forall \underline{x} \times t \in \Omega \times \partial T \end{array} \right\} \tag{3.5}$$

$$\mathrm{B}_0^T = \left\{ \delta\alpha : \Omega \times T \to [0,1] \;\middle|\; \begin{array}{ccc} \delta\alpha = 0 & \forall \underline{x} \times t \in \partial_\alpha \Omega \times T & \text{and} \\ \delta\alpha = 0 & \forall \underline{x} \times t \in \Omega \times \partial T & \text{and} \\ 0 \leq \alpha_\tau \leq \alpha_t + \delta\alpha \leq 1 & \forall \underline{x} \times \tau \in \Omega \times [0,t) & \end{array} \right\} \tag{3.6}$$

The energetic terms defined in Eqs. (3.1)-(3.4) can be combined per Eq. (3.7) to obtain the generalized Lagrangian $\mathscr{L}$ of the system. In turn, the integral over T of the latter functional yields the space-time action integral $\mathscr{A}$ of the system evolution as shown in Eq. (3.8).

$$\mathscr{L}\left(\underline{u}_t, \dot{\underline{u}}_t, \alpha_t, t\right) = -\mathscr{K}\left(\dot{\underline{u}}_t, t\right) + \mathscr{E}_{\mathrm{str}}\left(\underline{u}_t, \alpha_t, t\right) + \mathscr{E}_{\mathrm{frac}}\left(\alpha_t, t\right) - \mathscr{W}_{\mathrm{ext}}\left(\underline{u}_t, t\right) \tag{3.7}$$

$$\mathscr{A}\left(\underline{u}_t, \dot{\underline{u}}_t, \alpha_t, t'\right) = \int_0^{t'} \mathscr{L}\left(\underline{u}_t, \dot{\underline{u}}_t, \alpha_t, t\right) \mathrm{d}t \tag{3.8}$$

Based on Hamilton's principle for irreversible evolutions, the considered system will follow a path of states $(\underline{u}_t, \dot{\underline{u}}_t, \alpha_t)$ along T for which $\delta\mathscr{A} \geq 0$ holds upon every admissible variation $(\delta\underline{u}, \delta\alpha)$. Developing such variational principle while considering that this must be true $\forall t' > 0$, one can perform some algebraic manipulations and derive the generalized Euler-Lagrange equation of the system as:

$$\begin{aligned} -\frac{\mathrm{d}}{\mathrm{d}t}\left(\mathrm{D}_{\dot{\underline{u}}}\mathscr{L}\left(\underline{u}_t, \dot{\underline{u}}_t, \alpha_t, t\right)\right)\left[\delta\underline{u}\right] + \mathrm{D}_{\underline{u}}\mathscr{L}\left(\underline{u}_t, \dot{\underline{u}}_t, \alpha_t, t\right)\left[\delta\underline{u}\right] + \\ + \mathrm{D}_{\alpha}\mathscr{L}\left(\underline{u}_t, \dot{\underline{u}}_t, \alpha_t, t\right)\left[\delta\alpha\right] \geq 0 \quad \forall \left\{\delta\underline{u}, \delta\alpha\right\} \in \left\{\mathrm{V}_0^T, \mathrm{B}_0^T\right\}. \end{aligned} \tag{3.9}$$

The underlying concept behind Eq. (3.9) is analogous to Eq. (2.13): the structural system follows the path of kinematically admissible states that make $\mathscr{A}$ stationary ($\delta\mathscr{A} = 0$) provided that the irreversibility condition is fulfilled; otherwise, the admissible states must yield a positive first variation of the action ($\delta\mathscr{A} > 0$). However, since the monolithic resolution of the variational principle results arduous, it is commonly staggered into two more easily solvable principles that read:

$$-\frac{\mathrm{d}}{\mathrm{d}t}\left(\mathrm{D}_{\underline{\dot{u}}}\mathscr{L}\left(\underline{u}_t,\underline{\dot{u}}_t,t;\alpha\right)\right)[\delta\underline{u}]+\mathrm{D}_{\underline{u}}\mathscr{L}\left(\underline{u}_t,\underline{\dot{u}}_t,t;\alpha\right)[\delta\underline{u}]=0\quad\forall\delta\underline{u}\in\mathrm{V}_0^T\,,\tag{3.10}$$

$$\mathrm{D}_{\alpha}\mathscr{L}\left(\alpha_t,t;\underline{u},\underline{\dot{u}}\right)[\delta\alpha]\geq 0\quad\forall\delta\alpha\in\mathrm{B}_0^T\,.\tag{3.11}$$

Concerning their physical meaning, Eq. (3.10) represents the condition of dynamic equilibrium for fixed α, whereas Eq. (3.11) controls the evolution of the phase field for a given state of motion. Therefore, the staggering procedure simplifies the resolution by weakening the coupling between the motion and damage aspects of the problem. Still, this is only representative if the best available estimates for each of the fixed fields are fed to the staggered principles (see Section 2.3). As with the quasi-static PFM, the consecutive resolution of Eqs. (3.10) and (3.11) does not guarantee a good approximation to the solution of Eq. (3.9), especially if coarse time discretizations are used. This shortcoming can be mitigated in the dynamic PFM by either using alternate minimization algorithms or small time increments.

Considering the energy components defined in Eqs. (3.1) to (3.4) and developing the derivative terms of the staggered variational principles in Eqs. (3.10) and (3.11), the following governing expressions are obtained:

$$\begin{aligned}\int_{\Omega}\rho\ddot{\underline{u}}_t\cdot\delta\underline{u}\,\mathrm{d}\underline{x}+\int_{\Omega}\underline{\underline{\sigma}}\left(\underline{\underline{\varepsilon}}\left(\underline{u}_t\right);a_{\mathrm{PF}}\left(\alpha\right)\right):\underline{\underline{\varepsilon}}\left(\delta\underline{u}\right)\mathrm{d}\underline{x}=\\ =\int_{\Omega}\underline{b}_t\cdot\delta\underline{u}\,\mathrm{d}\underline{x}+\int_{\partial_f\Omega}\underline{f}_t\cdot\delta\underline{u}\,\mathrm{d}\underline{x}\quad\forall\delta\underline{u}\in\mathrm{V}_0^T\end{aligned}\,,\tag{3.12}$$

$$\begin{aligned}\int_{\Omega}\frac{G_C}{c_w}\left(\frac{1}{\ell}\frac{\partial w_{\mathrm{PF}}(\alpha_t)}{\partial\alpha}\cdot\delta\alpha+2\ell\nabla\alpha_t\cdot\nabla\delta\alpha\right)\mathrm{d}\underline{x}+\\ +\int_{\Omega}\frac{\partial\psi\Big(a_{\mathrm{PF}}(\alpha_t);\underline{\underline{\varepsilon}}(\underline{u})\Big)}{\partial\alpha}\cdot\delta\alpha\,\mathrm{d}\underline{x}\geq 0\quad\forall\delta\alpha\in\mathrm{B}_0^T\end{aligned}\,.\tag{3.13}$$

Therefore, the staggered principles of the dynamic PFM present three different primary magnitudes, namely the displacement $\underline{u}$ and acceleration $\ddot{\underline{u}}$ fields in the dynamic equilibrium equation, added to the phase field α in the damage criterion.

The comparison of Eqs. (3.12) and (3.13) with Eqs. (2.16) and (2.17) reveals the similarities definition-wise between the quasi-static and dynamic PFMs. In particular, the corresponding damage criteria are effectively identical since B_0^T and B_0 collapse $\forall t\notin\partial T$. In contrast, the motion principles change and the quasi-static equilibrium equation from Chapter 2 is just a particularization of the dynamic one. Besides, since

α is fixed in Eq. (3.12), this principle matches the classical governing equation for an elastodynamic problem wherein the elastic properties are inhomogeneous. As such, the resolution of Eq. (3.12) can benefit from the well-established developments in that regard, such as time integration algorithms or optimized dynamic solvers.

3.2.1 Implementation of the dynamic Phase Field Fracture model using explicit time integration

In what follows, the undertaken numerical implementation of the dynamic equilibrium equation in the context of the PFM is detailed. Concerning the time integration algorithm, the explicit version of the well-known Newmark's β-method [91] has been used. This is the most common choice for solving highly-dynamic evolutions of heavy numerical models given its ability to be rendered computationally lightweight. Its basic fundament consists in estimating the time-continuous $\underline{u}_t$ and $\underline{\dot{u}}_t$ fields through the propagation into the future of known punctual-in-time states of motion. In particular, considering a time discretization in which t_i ($i \in \mathbb{N}$) represents the last instant whose state is known, and $\Delta t_i = t_{i+1} - t_i$ is the size of the time step for propagation, the estimates for the displacement and velocity field at t_{i+1} can be written as:

$$\underline{u}_{t_{i+1}} \approx \underline{u}_{i+1}(\ ; \underline{u}_i, \underline{\dot{u}}_i, \underline{\ddot{u}}_i) = \underline{u}_i + \Delta t_i \underline{\dot{u}}_i + \frac{\Delta t_i^2}{2} \underline{\ddot{u}}_i \,, \tag{3.14}$$

$$\underline{\dot{u}}_{t_{i+1}} \approx \underline{\dot{u}}_{i+1}\left(\underline{\ddot{u}}_{i+1}; \underline{\dot{u}}_i, \underline{\ddot{u}}_i\right) = \underline{\dot{u}}_i + \Delta t_i \frac{\underline{\ddot{u}}_i + \underline{\ddot{u}}_{i+1}}{2} \,. \tag{3.15}$$

It is to be noted that the estimated magnitudes are here identified with the indices of the time step they refer to, i.e. i and $i+1$, rather than with the instants t_i and t_{i+1} like their exact counterparts. In particular, the expressions above correspond to the Newmark's "Central difference method", which is an explicit time integrator scheme in that $\underline{u}_{i+1}$ is completely defined in terms of the known motion state at t_i. Likewise, once $\underline{u}_{i+1}$ is known, the estimate α_{i+1} can be determined through the Eq. (3.13). On the other hand, the velocity estimate $\underline{\dot{u}}_{i+1}$ depends partially on the system state at t_{i+1} through the acceleration estimate, which is unknown *a priori*. However, particularizing the dynamic equilibrium condition in Eq. (3.12) to t_{i+1} and using the known estimate $\underline{u}_{i+1}$, one can write:

$$\begin{aligned}\int_\Omega \rho\, \underline{\ddot{u}}_{i+1} \cdot \delta\underline{u}\, \mathrm{d}\underline{x} + \int_\Omega \underline{\underline{\sigma}}\left(\underline{\underline{\varepsilon}}\left(\underline{u}_{i+1}\right); a_{\mathrm{PF}}\left(\alpha_{i+1}\right)\right) : \underline{\underline{\varepsilon}}\left(\delta\underline{u}\right) \mathrm{d}\underline{x} = \\ = \int_\Omega \underline{b}_{t_{i+1}} \cdot \delta\underline{u}\, \mathrm{d}\underline{x} + \int_{\partial_f\Omega} \underline{f}_{t_{i+1}} \cdot \delta\underline{u}\, \mathrm{d}\underline{x} \quad \forall \delta\underline{u} \in \mathrm{V}_0\end{aligned}, \tag{3.16}$$

wherein $\underline{\ddot{u}}_{i+1}$ is the sole unknown. As such, for a given displacement $\underline{u}_{i+1}$ (and a phase field α_{i+1}), the determination of the estimated acceleration field $\underline{\ddot{u}}_{i+1}$ is straightforward. Subsequently, $\underline{\dot{u}}_{i+1}$ can be calculated through Eq. (3.15). Remarkably, this procedure is almost identical to the conventional explicit approach to elastodynamics were it not for the update of α.

The simplicity of the explicit time integrator comes at the cost of conditional stability in what concerns the time step size Δt. Indeed, for it to be stable, the Courant–Friedrichs–Lewy (CFL) condition [92] in Eq. (3.17) has to be fulfilled, $\omega_{\max}$ being the maximum natural frequency of the system.

$$\Delta t < \frac{2}{\omega_{\max}} \tag{3.17}$$

Therefore, the maximum time step size for the explicit scheme to be stable when applied to a continuum is zero since $\omega_{\max}$ is infinite therein. For discretized domains within the Finite Element context instead, $\omega_{\max}$ is finite and generally increases as the characteristic size of the elements gets smaller. In order to avoid the considerable computational cost of exactly computing of $\omega_{\max}$, the exact CFL condition above is often substituted by the following approximation:

$$\Delta t < \frac{h_{\min}}{\eta\, c}, \tag{3.18}$$

where $h_{\min}$ is the minimum distance between two different nodes, η is a safety factor greater than 1, and c is the speed of sound in the material, which is in turn proportional to $\sqrt{E/\rho}$. Therefore, the approximated stability condition depends on the domain discretization and on the effective elastic properties. As such, the development of α in the dynamic PFM will affect the stability condition, yet turning it less restrictive on the size of Δt. Consequently, the critical value for Δt is safely computed beforehand by assuming pristine conditions all along the domain.

Upon discretization of PFM's dynamic equilibrium condition to a Finite Element context, the continuous fields are transformed into nodal vectors following $\underline{u} \to \mathrm{d}$,

$\underline{\dot{u}} \to \mathsf{v}$, $\underline{\ddot{u}} \to \mathsf{a}$ and $\alpha \to \mathsf{c}$. Likewise, the discretization of the two bilinear forms in the left hand side of Eq. (3.16) yields the mass M and stiffness K matrices, the latter being modulated by the nodal values of the phase field c. Discretizing instead the linear form on the right hand side of Eq. (3.16), the vector of nodal forces f is obtained. Eventually, the unknown vector of nodal accelerations a_{i+1} can be explicitly determined from the discretized dynamic equilibrium condition at t_{i+1} as follows:

$$\mathsf{a}_{i+1} = \mathsf{M}^{-1}\left[-\mathsf{K}_{i+1}(\mathsf{c}_{i+1})\,\mathsf{d}_{i+1} + \mathsf{f}_{i+1}\right]. \tag{3.19}$$

The conventional assembly of M from the associated bilinear form generally leads to a full symmetric matrix, commonly referred to as Consistent mass matrix. If used, the determination of a_{i+1} for a discretized system of N_{DoF} degrees of freedom is of cost $\mathscr{O}\left(N_{DoF}^3\right)$. This, combined with the small Δt required to comply with the CFL condition, implies that the use of fine meshes in explicit models for elastodynamics in general, and dynamic PFM in particular, can lead to a prohibitively high computational cost. To avoid this, the Consistent mass matrix M is often diagonalized, yielding the Lumped mass matrix M_L and reducing the cost of determining a_{i+1} to $\mathscr{O}\left(N_{DoF}\right)$. Different approaches are proposed in the literature to calculate the diagonal counterpart [93], yet the choice herein used writes as:

$$\mathsf{M}_\mathrm{L} = (\mathsf{M}\,\mathsf{1})\,\mathsf{I} \tag{3.20}$$

where $\mathsf{1}$ is a $N_{DoF} \times 1$ vector of ones, I is the $N_{DoF} \times N_{DoF}$ identity matrix. Therefore, Eq. (3.20) lumps the consistent mass matrix M by finding the diagonal one M_L that yields, for a nodal acceleration vector of ones, the same vector of nodal forces. Implementation-wise, this is achieved by assigning to each diagonal term of M_L the sum of all the components within the corresponding row of M. For more details on the dynamic PFM's resolution algorithm, please refer to Appendix A.

3.3 Case study on the post-punch fragmentation of biaxially pre-strained 2D glass panes

The above detailed dynamic PFM will be now exploited to study the fragmentation problem illustrated in Fig. 3.2. The squared domain is initially pristine and under uniform pre-straining so that its deformation state prior to crack nucleation is well-

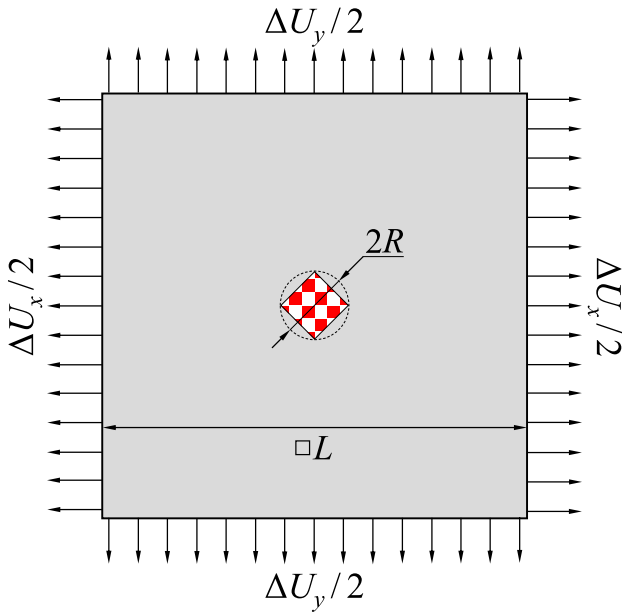

Fig. 3.2 Illustration of the biaxially pre-strained 2D glass pane "punched" in its centre.

defined. At $t = 0$, α is set to 1 (broken state) within the red and white chequered region, which is supposed to mimic the instantaneous punching of the glass pane. Provided a sufficiently intense pre-straining, the localized sudden loss of stiffness causes an abrupt concentration of stresses that eventually triggers fracture, which develops as multiple and interacting cracks that end up fragmenting the pane. In particular, the conducted analysis heeds the effect, according to the dynamic PFM, of the pre-straining intensity and biaxiality in the resultant cracking process. In this regard, the prescribed elongations ΔU_x and ΔU_y relate to the uniform pre-straining state $\underline{\underline{\varepsilon}}_0$ as:

$$\underline{\underline{\varepsilon}}_0 = \begin{pmatrix} \Delta U_x/L & 0 \\ 0 & \Delta U_y/L \end{pmatrix}, \tag{3.21}$$

which in turn can be expressed more conveniently in terms of the pre-straining intensity ε_0 and biaxiality ratio $\beta_\varepsilon = \Delta U_y/\Delta U_x$ as:

$$\underline{\underline{\varepsilon}}_0 = \varepsilon_0 \begin{pmatrix} 1 & 0 \\ 0 & \beta_\varepsilon \end{pmatrix}. \tag{3.22}$$

In order to model a material only damageable in tension, the No-Tension energy decomposition [51] was chosen. Likewise, the AT1 model [25] was used so as to have a reasonable management of the fracture energy term [30] while keeping the

numerical complexity low. Per the results in Section 2.4, this combination proved good predicting capabilities for the evolution of fracture in complex multiaxial stress states. For simplicity, 2D plane strain conditions were assumed in every PFM simulation here conducted.

Regarding the dynamic PFM implementation in a Finite Element context, first order triangular elements with an overall size equal to $\ell/4$ were used. This ensured proper capturing of the solution even upon the high gradients in the regions transitioning from pristine to broken. Moreover, the element size was kept uniform throughout the mesh in order to minimize undesired wave reflections due to localized coarser discretizations. Regarding the material properties and modelling parameters instead, the values in Table 3.1 were used, which in turn correspond to the characteristic mechanical properties of glass.

Table 3.1 Material properties and modelling parameters used for the Phase Field simulations.

ρ	E	ν	G_C	ℓ	σ_C^{NT}
$[\mathrm{Kg/m^3}]$	[MPa]	$[-]$	[MPa · mm]	[mm]	[MPa]
2500	72000	0.2	0.0075	0.09	50.0

3.3.1 Case study A: Effect of the pre-straining magnitude

In order to capture the influence of the pre-straining intensity on the resultant crack patterns, let us consider the setup described in Fig. 3.2 and set its characteristic dimensions to $L = 14$ mm and $R = 0.25$ mm. Likewise, prescribing in-plane hydrostatic traction conditions prior to cracking, i.e. $\Delta U_x = \Delta U_y > 0$, the pre-straining biaxiality is $\beta_\varepsilon = 1$. Under these loading conditions and material properties, the PFM/No-Tension/AT1 homogeneous solution losses its stability at $\varepsilon_0 \approx 3.95 \cdot 10^{-4}$; above this pre-straining intensity α develops prior to the punching. On the other hand, the minimum pre-straining intensity for which post-punch crack propagation is observed was iteratively found to be $\varepsilon_0 \approx 2.4 \cdot 10^{-4}$. Remarkably, the quasi-static resolution of the same problem would reveal this lower threshold to be $\varepsilon_0 \approx 2.57 \cdot 10^{-4}$ instead. Such a difference can be attributed to the inability of the quasi-static model to properly capture the transient evolution right after the localized sudden loss of stiffness. For more details on the differences between the quasi-static and dynamic modelling of fracture, please refer to the comprehensive analysis in Chapter 4.

In order to cover the whole range of pre-straining intensities that lead to post-punching fragmentation, four equispaced values of ε_0 have been simulated, namely $\varepsilon_0 = 2.4 \cdot 10^{-4}$, $\varepsilon_0 = 2.9 \cdot 10^{-4}$, $\varepsilon_0 = 3.4 \cdot 10^{-4}$ and $\varepsilon_0 = 3.9 \cdot 10^{-4}$. The crack patterns obtained right after the first fracturing event are shown in Fig. 3.3, i.e. at the first instant $t > 0$ in which α does not develop anywhere in the domain. After the first cracking event, stress wave reflections were found to eventually resume the growth of α in subsequent cracking events, especially for the highest pre-straining intensities, yet these will be omitted herein.

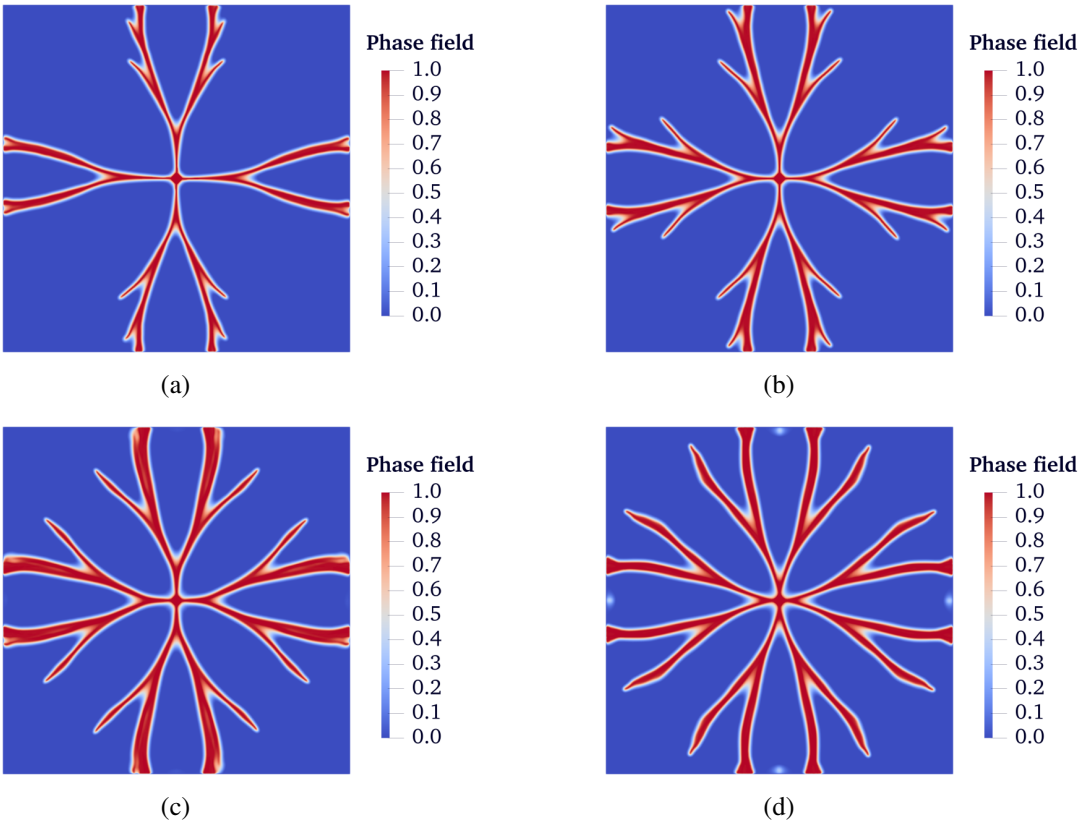

Fig. 3.3 Crack patterns after the first fracturing event obtained for a 2D glass pane under in-plane hydrostatic pre-straining with: (a) $\varepsilon_0 = 2.4 \cdot 10^{-4}$, (b) $\varepsilon_0 = 2.9 \cdot 10^{-4}$, (c) $\varepsilon_0 = 3.4 \cdot 10^{-4}$ and (d) $\varepsilon_0 = 3.9 \cdot 10^{-4}$.

The dependence of the obtained crack patterns with ε_0 results moderate, showing a mostly unvaried cracking mechanism: the initially cruciform crack first splits into the primary branches, which in turn then branch to become the secondary ones (see Fig. 3.4). Likewise, the branching angles were also found to be rather insensitive to ε_0, with approximately 40° and 90° as the primary and secondary branching

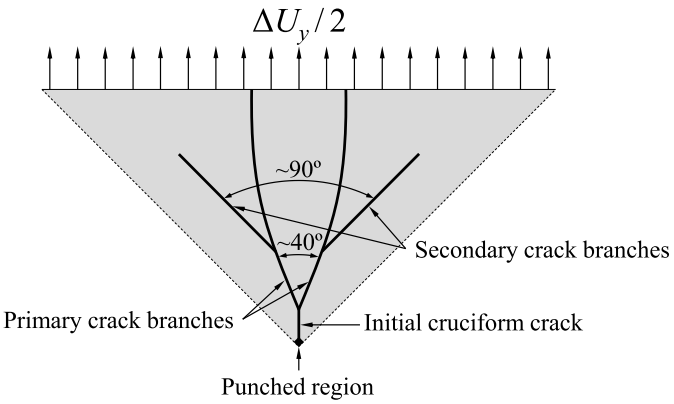

Fig. 3.4 One quarter schematic representation of the crack pattern after the first fracturing event in the hydrostatically pre-strained punched glass pane ($\beta_\varepsilon = 1$).

angles for all cases considered but when $\varepsilon_0 = 2.4 \cdot 10^{-4}$. More into details, the obtained crack patterns show that larger values of ε_0 mainly lead to: (i) the initial cruciform crack branching sooner, (ii) the secondary branches developing further, and (iii) generally thicker smeared cracks. The latter observation was interpreted in the literature as the PFM representation of the micro-branching phenomenon [30], in turn inferring high crack tip velocities. Moreover, the motif behind the two former insights can be identified in the larger strain energy component stored in the domain prior to fracture, which requires more developed dissipation mechanisms. Conversely, when the initial pre-straining is relatively small, e.g. for $\varepsilon_0 = 2.4 \cdot 10^{-4}$, crack growth is more restricted due to its energetic cost, and some shielding effects between branches are observed (see Fig. 3.3a). Overall, the obtained results indicate that the more intense the pre-straining, the more developed the crack patterns, but the general cracking mechanism is maintained in all cases.

The energetic transformations taking place along the first cracking event are reported in Fig. 3.5 for each ε_0 considered. These plots explicitly depict how the strain energy initially stored in the domain gets progressively converted into kinetic and fracture energy components as the cracks develop. Given that the dynamic PFM mostly conserves the total energy in the system [27], the higher the pre-straining, the more energy needs to be dissipated into fracture energy or converted into kinetic energy during fracturing. The system achieves the former effect through crack branching, be it macro or micro, yet the maximum rate of conversion to fracture energy seems upper bounded as ε_0 grows (see Fig. 3.5c). Therefore, intense enough pre-strainings take the system's dissipative fracture power $\dot{\mathscr{E}}_{\text{frac}}$ to saturation, entailing

a sheer growth of inertial effects to cope with the surplus of strain energy released (see Fig. 3.5a). A potential explanation to this saturation regime can be found in the interaction between different crack branches, which can shield further branching and thereby upper limit the system's ability to dissipate energy through $\mathscr{E}_{\text{frac}}$. Lastly, results in Fig. 3.5 show that the increase in ε_0 leads to the cracks propagating faster, in that the first fracturing event is completed in a shorter time interval.

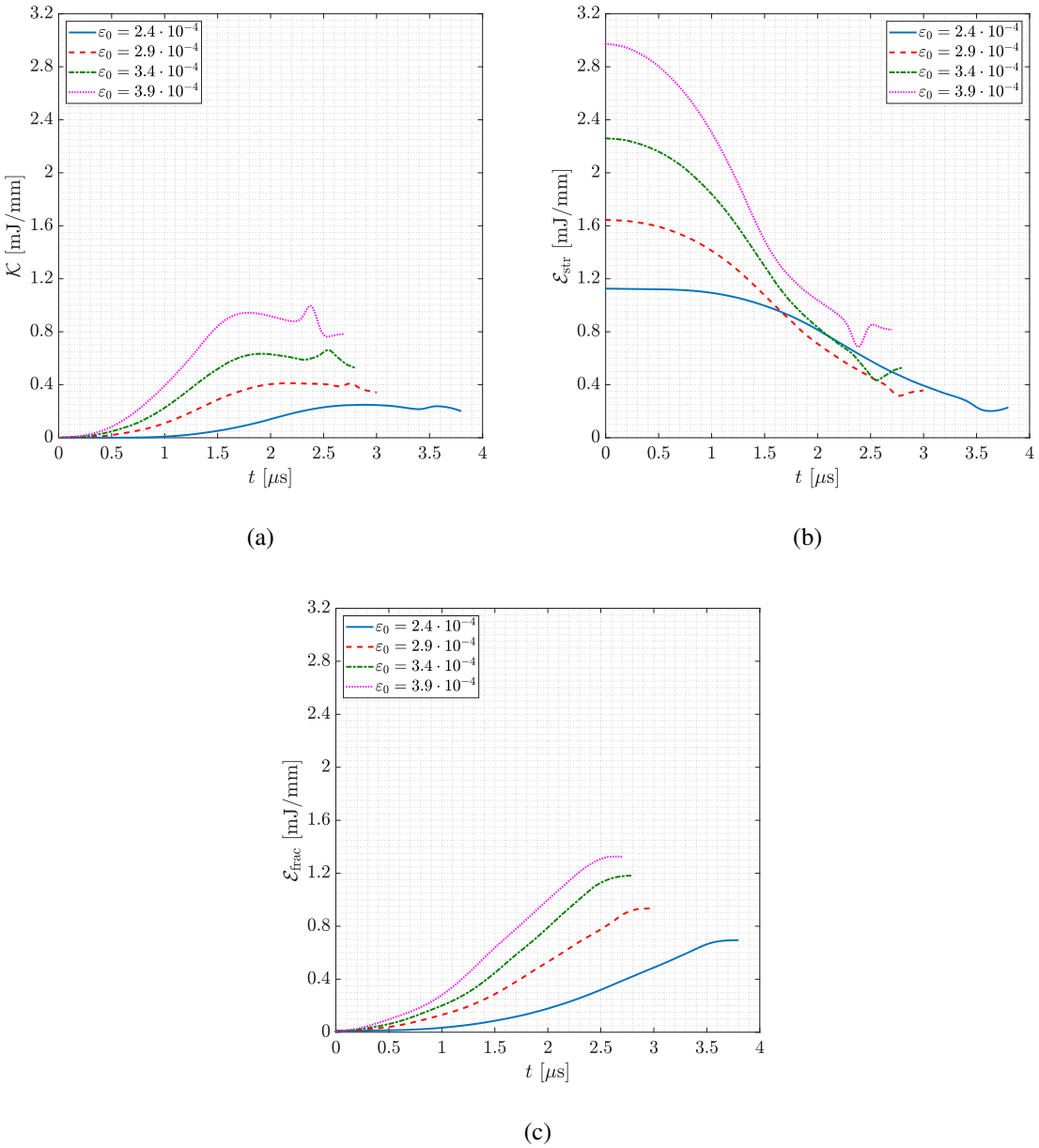

Fig. 3.5 Evolution of: (a) $\mathscr{K}$, (b) $\mathscr{E}_{\text{str}}$ and (c) $\mathscr{E}_{\text{frac}}$ during the first fracturing event of a 2D glass pane under in-plane hydrostatic pre-straining of different intensity.

3.3.2 Case study B: Effect of the pre-straining biaxiality

The analysis above is hereafter complemented by studying the effect of the pre-straining biaxiality β_ε on the glass pane fragmentation. For all cases here considered, the initial strain energy $\mathscr{E}_{\text{str}}^{\circ}$ stored in the domain is kept constant for the sake of coherence. Therefore, for a given hydrostatic pre-straining magnitude of reference $\varepsilon_0(\beta_\varepsilon = 1)$ and biaxiality ratio β_ε, the corresponding pre-straining intensity $\varepsilon_0(\beta_\varepsilon)$ can be determined as:

$$\varepsilon_0(\beta_\varepsilon) = \sqrt{\frac{4(\lambda+\mu)}{(\lambda+2\mu)(1+\beta_\varepsilon^2)+2\lambda\beta_\varepsilon}}\,\varepsilon_0(\beta_\varepsilon = 1)\,. \tag{3.23}$$

Now taking the four different equispaced and positive biaxiality ratios $\beta_\varepsilon = 0.75$, $\beta_\varepsilon = 0.5$, $\beta_\varepsilon = 0.25$ and $\beta_\varepsilon = 0.0$, and $\varepsilon_0(\beta_\varepsilon = 1) = 2.9 \cdot 10^{-4}$ as the in-plane hydrostatic reference, the pre-straining intensities to be here considered are

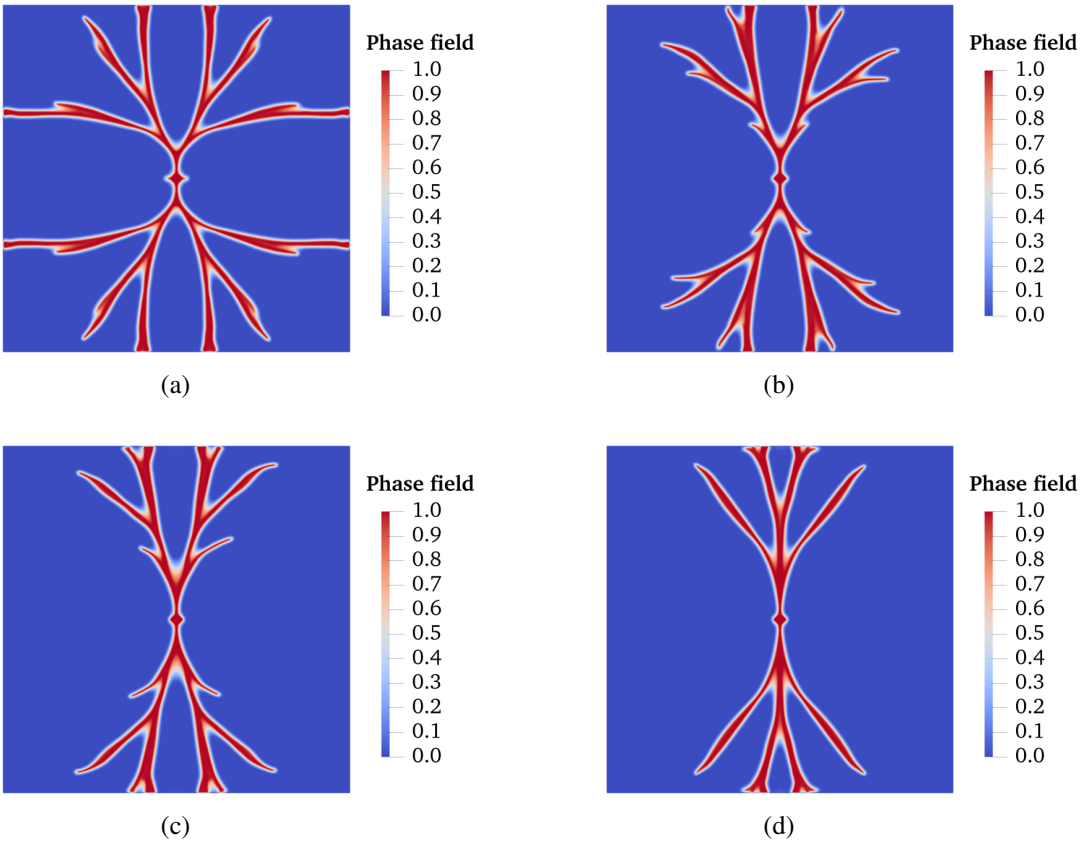

Fig. 3.6 Crack patterns after the first fracturing event obtained for a 2D glass pane under biaxial pre-straining with: (a) $\beta = 0.75$ and $\varepsilon_0 = 3.29 \cdot 10^{-4}$, (b) $\beta = 0.5$ and $\varepsilon_0 = 3.74 \cdot 10^{-4}$, $\beta = 0.25$ and (c) $\varepsilon_0 = 4.21 \cdot 10^{-4}$, and (d) $\beta = 0.0$ and $\varepsilon_0 = 4.59 \cdot 10^{-4}$.

$\varepsilon_0 = 3.29 \cdot 10^{-4}$, $\varepsilon_0 = 3.74 \cdot 10^{-4}$, $\varepsilon_0 = 4.21 \cdot 10^{-4}$ and $\varepsilon_0 = 4.59 \cdot 10^{-4}$. For each of these conditions, the corresponding crack patterns after the primary fracturing event are shown in Fig. 3.6, which are to be compared against Fig. 3.3b.

The most evident change observed for the cases where $\beta_\varepsilon < 1$ is the absence of horizontal crack stems. This reduces the shielding effect on the initially vertical cracks, and allows to reach branching angles as high as $\sim 170^\circ$ in order to dissipate the strain energy coming from the vertical pre-straining (see e.g. Fig. 3.6a). Further reductions in the pre-straining biaxiality lead to smaller crack branching angles, hence implying that β_ε, unlike ε_0, has a significant effect on the crack patterns. It also results interesting to analyse in detail the crack pattern observed in Fig. 3.6d, in which the widest (secondary) crack branching takes place before the narrowest (primary) one, in contrast with the rest of cases here presented (see Fig. 3.7). A potential explanation for this difference lies in that the only horizontal pre-straining,

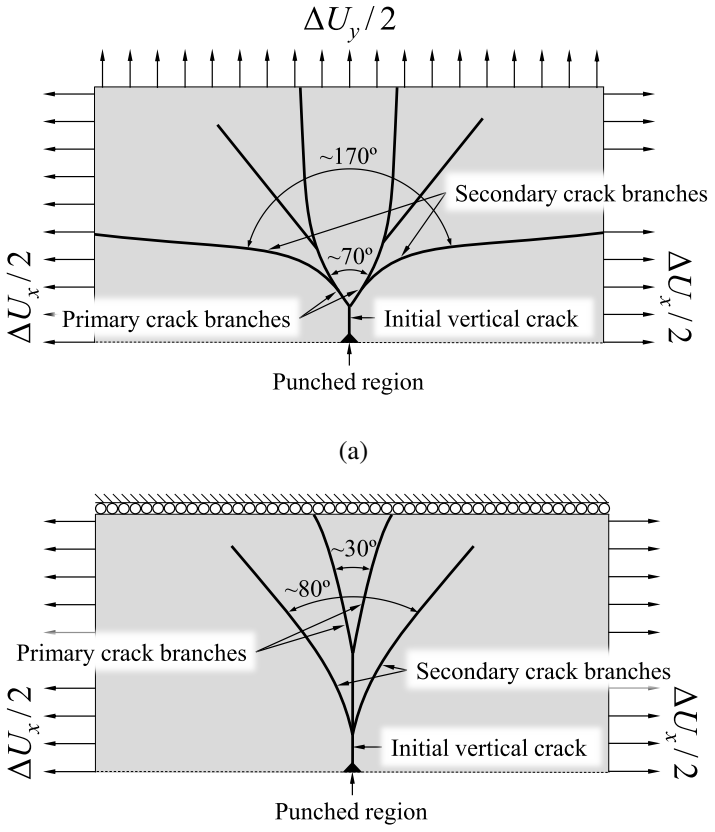

Fig. 3.7 One half schematic representation of the crack pattern after the first fracturing event of the pre-strained punched glass pane for: (a) $\beta_\varepsilon = 0.75$ and $\varepsilon_0 = 3.29 \cdot 10^{-4}$, and (b) $\beta_\varepsilon = 0.0$ and $\varepsilon_0 = 4.59 \cdot 10^{-4}$.

of higher magnitude so as to keep the initial $\mathscr{E}_{\text{str}}$ constant, maximizes the crack driving force in the vertical direction. Therefore, the initially vertical cracks rapidly accelerate, which causes them to branch at an angle $\sim 80^\circ$. Nonetheless, the resultant rate of conversion into fracture energy considering those branches alone would not suffice, and so the system keeps propagating the most-energetically-favourable vertical cracks as well. Eventually, these latter cracks branch at an angle $\sim 30^\circ$ once they reach high enough propagation velocity.

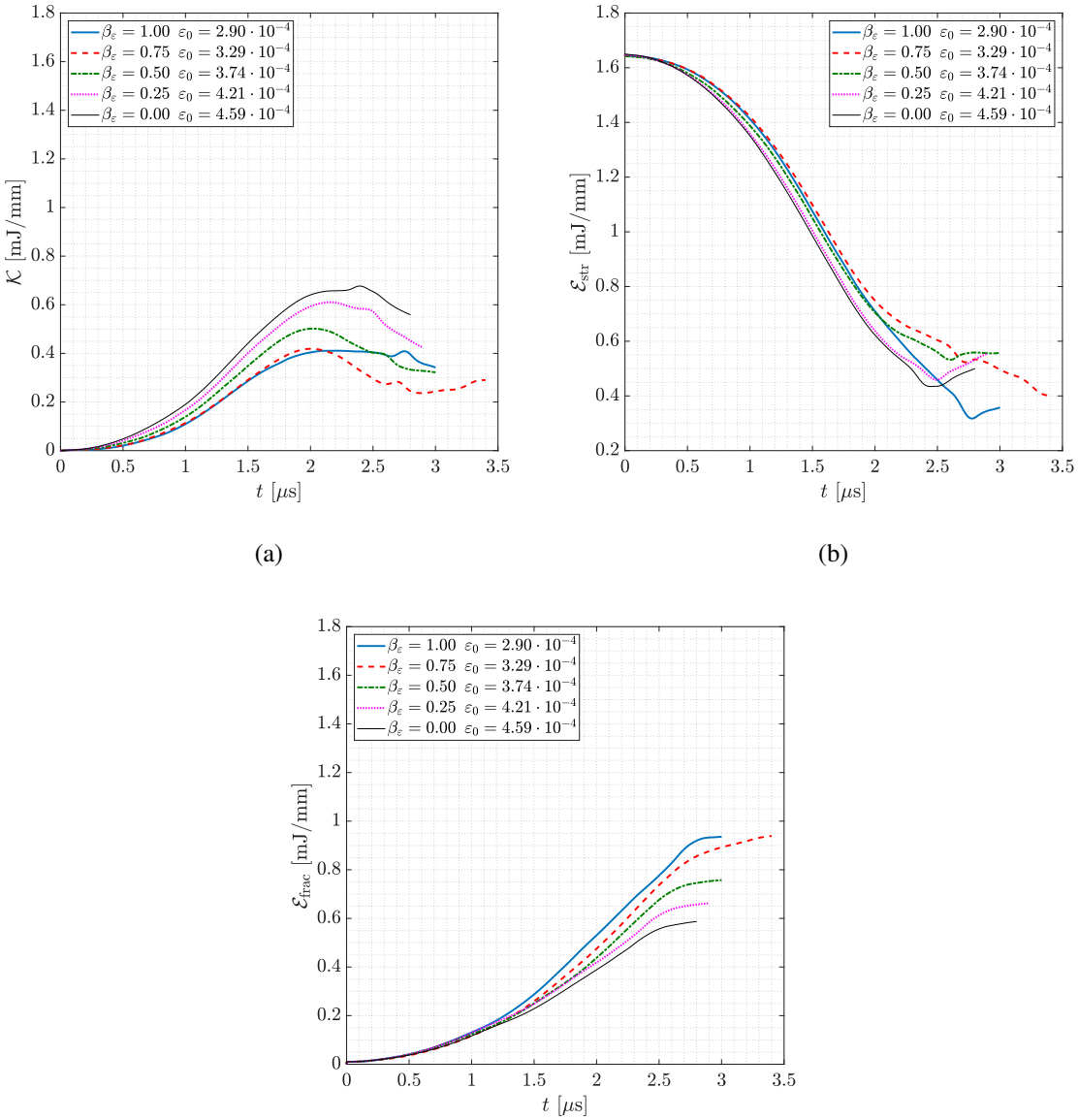

Fig. 3.8 Evolution of: (a) $\mathscr{K}$, (b) $\mathscr{E}_{\text{str}}$ and (c) $\mathscr{E}_{\text{frac}}$ during the first fracturing event of a 2D glass pane under pre-straining of different positive biaxiality.

For the five non-negative ratios of pre-straining biaxiality considered, the energetic transformations obtained along the different primary fracturing events are reported in Fig. 3.8. Once again, it is seen how $\mathscr{E}_{\text{str}}$ is reduced as the domain fractures and $\mathscr{E}_{\text{frac}}$ increases. However, and differently from the case study on the pre-straining intensity, now $\mathscr{E}_{\text{str}}$ is seen to diminish almost identically regardless of the considered β_ε. At the same time, $\mathscr{E}_{\text{frac}}$ becomes smaller in average as $\beta_\varepsilon \to 0$; due to the conservation of total energy, this also implies that $\mathscr{K}$ becomes larger (in average). Moreover, it is seen how the time necessary to complete the first cracking event is non-monotonic with respect to ε_β, the case of $\beta_\varepsilon = 0.75$ taking the longest. In such case, one has to consider that the absence of initially horizontal crack branches, combined with a reasonably large vertical pre-straining, causes the most external branches of the initially vertical crack to curve and become almost horizontal. Therefore, these secondary crack branches follow a considerably long path that leads to longer first cracking events. Besides this exception, the time elapsed for the first cracking event is seen to generally be shortened as the biaxiality is reduced.

In the event of compressive vertical pre-straining, i.e. for $\beta_\varepsilon < 0$, the use of the No-Tension energy decomposition hinders the horizontal development of cracks, and so it reduces the system's capacity to branch. This is clearly seen in the patterns reported in Fig. 3.9, in which $\beta_\varepsilon = -0.25$ and $\beta_\varepsilon = -0.5$, ε_0 being determined from Eq. (3.23). The comparison between the results from Fig. 3.3b and 3.6 with those from Figs. 3.9 reveals much smaller crack branching angles in the latter ones.

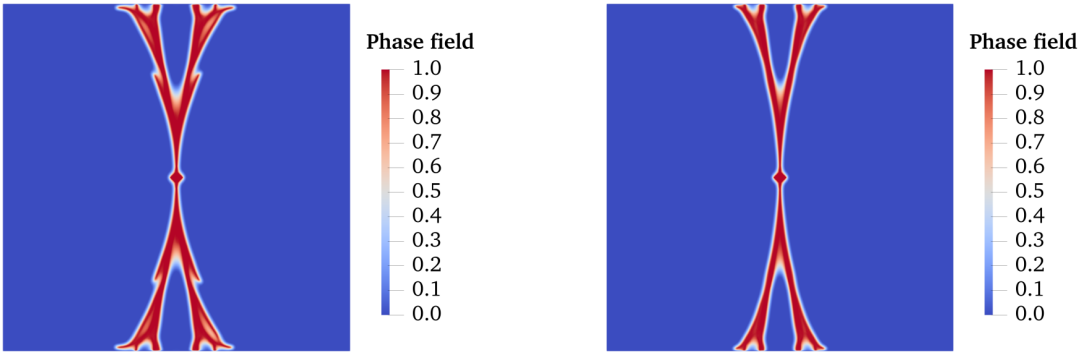

(a) (b)

Fig. 3.9 Crack patterns after the first fracturing event obtained for a 2D glass pane under biaxial pre-straining with: (a) $\beta = -0.25$ and $\varepsilon_0 = 4.74 \cdot 10^{-4}$, and (b) $\beta = -0.5$ and $\varepsilon_0 = 4.59 \cdot 10^{-4}$.

Regarding the energetic transformations that occur for $\beta_\varepsilon < 0$, the limitation in the crack branching capabilities reduces how much energy can be converted into $\mathscr{E}_{\text{frac}}$ (see Fig. 3.10c). Simultaneously, the compressive component of the straining does not participate in the release of energy, and thus the reduction of $\mathscr{E}_{\text{str}}$ as the cracks propagate becomes smaller as β_ε becomes more negative (see Fig. 3.10b).

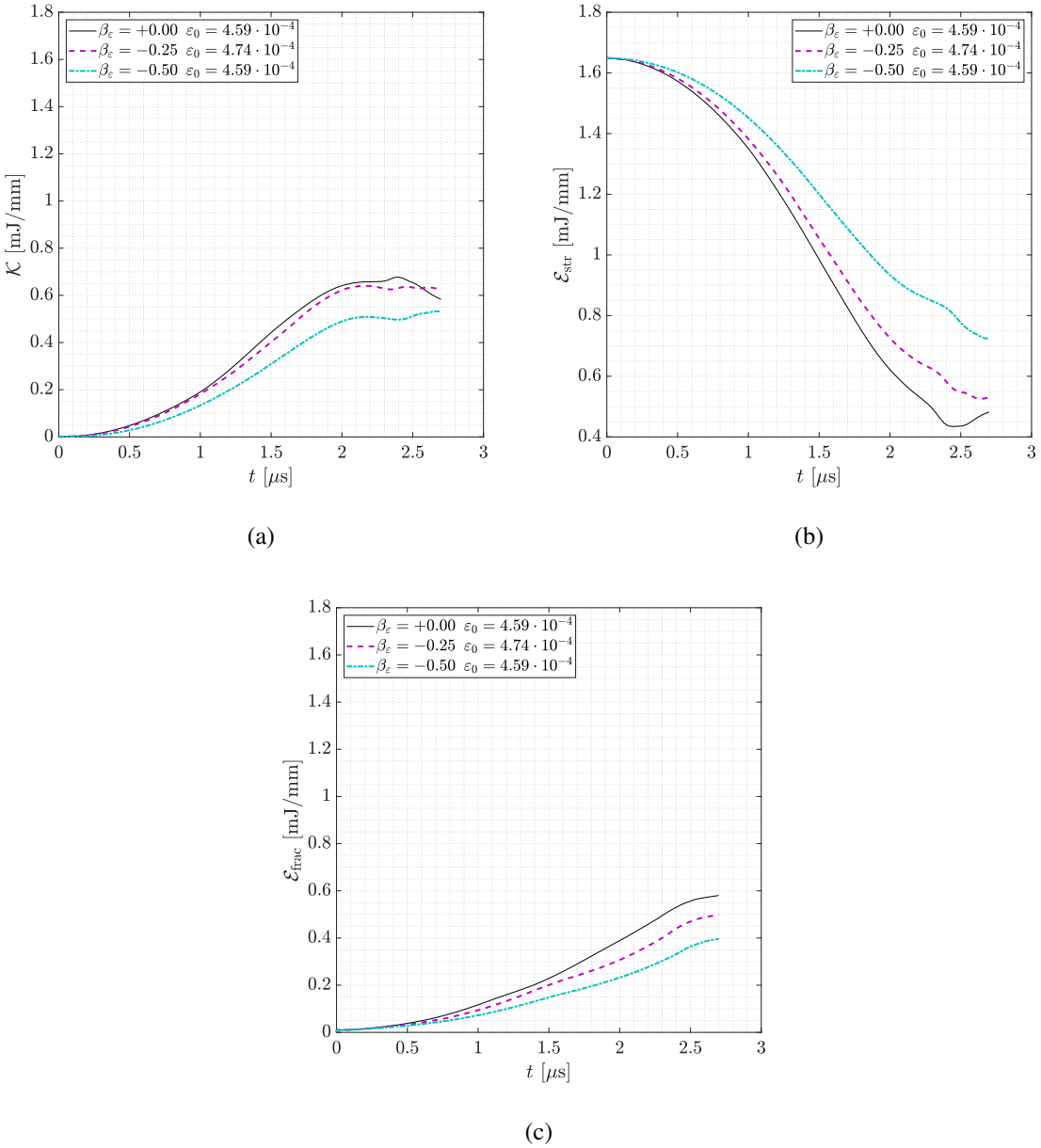

Fig. 3.10 Evolution of: (a) $\mathscr{K}$, (b) $\mathscr{E}_{\text{str}}$ and (c) $\mathscr{E}_{\text{frac}}$ during the primary fracture event of a 2D glass pane under pre-straining of different negative biaxiality.

Overall, these two reductions in the magnitude of the energetic transformations are not balanced: the surplus of energy released during the primary fracturing event decreases as the compressive pre-straining increases. As a result, $\mathscr{K}$ decreases as β_ε becomes more negative as well (see Fig. 3.10a).

3.4 Conclusions

The Phase Field fracture model introduced in the previous chapter has been now particularized and developed into a dynamic context by virtue of Hamilton's principle. In addition to providing the required theoretical framework, i.e. the governing variational principle, the main technical aspects of its numerical implementation using an explicit time integrator have also been covered. Moreover, the potential of the Phase Field fracture model to handle complex fracture phenomena has been exploited to study the post-punching fragmentation of a biaxially pre-strained glass pane. Specifically, two main aspects of the pre-straining have been independently considered: its intensity and degree of biaxiality. The obtained results have revealed that the former feature mainly affects the amount and extension of the crack branches, but it leaves the overall morphology of the crack patterns mostly unaltered. Conversely, the latter pre-straining characteristic was observed to heavily influence the branching angles, with the resultant crack patterns differing considerably from one another. All in all, the dynamic Phase Field fracture model has been explicitly proven to be capable of naturally handling complex bulk fracturing phenomena without additional ad-hoc considerations, hence posing a great advantage over other comparable approaches to fracture.

Chapter 4

Inconsistencies of quasi-static Phase Field fracture models for unstable crack propagations[1]

4.1 Introduction

As seen in the previous chapter, quasi-static loading conditions can lead to highly-dynamic evolutions in the event of unstable fracture. This occurs when the potential energy released as the crack propagates exceeds the dissipative capacity of the system. In such cases, crack growth is no longer driven by an external energy input but by the release of potential energy due to crack growth itself, hence posing an uncontrolled, self-sustained and potentially-catastrophic structural failure event. Therefore, it is paramount to properly understand and model the involved phenomena in order to be able to ensure the safety of critical structural components.

The study of unstable crack growth has been traditionally undertaken by means of quasi-static approaches, and the relevant works were mainly focused on unveiling the solution branches overshadowed by the snap-back or snap-through discontinuities (see e.g. [94, 95]). Such jumps in the overall behaviour occur whenever the strict fulfilment of quasi-static equilibrium leads to a decreasing trait in the loading

[1]Part of the work described in this chapter has been published in: Chao Correas, A., Reinoso, J., Cornetti, P., Corrado, M. (2024). On the (lack of) representativeness of quasi-static variational fracture models for unstable crack propagation. *J Mech Phys Solids* 186, 105573.

function, e.g. the magnitude of the prescribed force or displacement, which conventional control schemes cannot follow. To overcome such a difficulty while remaining in quasi-static equilibrium conditions, several experimental and theoretical works have used non-standard monotonically-increasing measures as inputs for controlling the loading, such as the crack opening displacement [96] or the crack extension itself [97–99]. Other pertinent numerical studies have relied on bespoke resolution techniques, namely the arc-length method [100, 101], in order to be able to follow the unstable solution branches [21].

From an energetic perspective, most of the approaches used to study the details of unstable fracture from a quasi-static standpoint rely on the same concept: the introduction of a factitious mechanism that disposes the excess of potential energy released during crack growth. This way, the originally unstable crack is artificially stabilized, although at the cost of changing the nature of the system under study. On the other hand, if the structural system is kept as-is and unstable fracture is naively modelled in a quasi-static context, the resultant behaviour would correspond to that of infinite viscous dissipation. Either way, the representativeness of quasi-static approaches is seriously undermined upon unstable crack propagations. Indeed, these are essentially dynamic processes whose actual energetic transformations cannot be accurately captured by quasi-static approaches [61]. Remarkably, the study of unstable fracture using dynamic cohesive models was undertaken in [21], and the results were compared to those obtained with a quasi-static model and the arc-length method. However, the particular choice of studied setup precluded capturing all the underlying differences between the predictions obtained with each cohesive framework.

In light of this, the present chapter will be devoted to prove the lack of representativeness of quasi-static approaches when applied to unstable fracture conditions. Particular attention will be paid to the cases where crack propagation encounters an energetic barrier, as well as to those in which the crack patterns are not trivial. To that end, the undertaken analysis is inspired by three different sources: (i) the experimental findings in [102] on the highly dynamic nature of unstable cracking under globally quasi-static conditions; (ii) the empirically observed effect of the energetic barriers for dynamic fracture development [103]; and (iii) the possibility of tailoring crack patterns using stress concentrators [53]. As such, the Phase Field fracture model vests as the ideal candidate for the present analysis, since both quasi-static and dynamic frameworks are available and well-established. For the sake of

conciseness, all the presented outcomes were addressed exclusively from the optic of the Phase Field fracture model; however, most of these apply to other widespread variational approaches to fracture as well, e.g. Cohesive Zone Models or Continuum Damage Mechanics. Bespoke experiments on 3D printed specimens were performed to support the theoretically obtained findings. From the contents of this chapter, it should rest clear that inertial effects are significant upon unstable crack propagation events, even under quasi-static loading conditions, and so only dynamic fracture models can be rigorous, robust and representative of reality in those cases.

4.2 Equivalent spring-mass model of multi-ligament unstable crack propagation

Unstable crack propagation takes place after nucleation whenever the potential energy release rate due to crack growth exceeds its specific energetic cost. Following Griffith's conventional notation, the post-crack-onset instability condition reads as $\partial G/\partial\Gamma > \partial G_C/\partial\Gamma$, with G being the potential energy release rate. The mismatch in the infinitesimal energy balance makes crack growth a self-sustained process that: (i) develops in short lapses of time, and (ii) abruptly changes the system's mechanical configuration. The resulting evolution thereby presents non-negligible inertial effects which have the potential to render quasi-static predictions inaccurate.

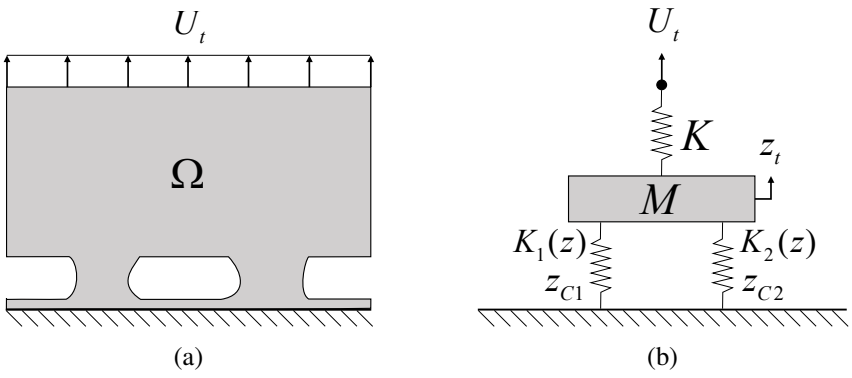

Fig. 4.1 Schematic representation of: (a) a domain with two resisting ligaments that features unstable crack propagation, and (b) its equivalent spring mass model.

The issues arising from quasi-statically modelling unstable fracture can be illustrated with the setup in Fig. 4.1a, where a generic 2D domain under uniaxial

tension presents a resisting section comprised of two ligaments with different overall strength. It being filled with a linear elastic and perfectly brittle material, fracture is confined to develop unstably within each ligament. As such, the system's mechanical response can be first-order approximated by means of the Spring-Mass system in Fig. 4.1b, in which the stiffness of the i-th spring ($i = \{1,2\}$) obeys the following cut-off law:

$$K_i(z) = \begin{cases} K_i & \text{for } z < z_{Ci} \\ 0 & \text{for } z \geq z_{Ci} \end{cases}, \tag{4.1}$$

where K_i is the spring's pristine stiffness and z_{Ci} its ultimate elongation, the loss of stiffness being irreversible. By convention, let us further assume that the spring 1 is the weakest of the two, so that:

$$z_{C2} = z_{C1} + \Delta z_C\,, \tag{4.2}$$

with z_{C1} and Δz_C being strictly positive. Furthermore, U_t evolves quasi-statically and increases monotonically with time, so that the system's only degree of freedom z_t follows the states of quasi-static equilibrium $\tilde{z}_t$ up to the breakage of spring 1. Assuming that such an event occurs at $t = 0$, it results that $z_{t=0} = z_{C1}$ and $U_{t=0} = U_{C1}$. From there onwards, the imposed displacement U_t is frozen so as to avoid introducing extra energy in the system, and therefore:

$$z_t = \tilde{z}_t = \frac{K}{K + K_1 + K_2} U_t \quad \text{for } t < 0\,, \tag{4.3}$$

$$U_t = U_{C1} = \frac{K + K_1 + K_2}{K} z_{C1} \quad \text{for } t \geq 0\,. \tag{4.4}$$

Due to the breakage of spring 1, both the system's mechanical configuration and its state of quasi-static equilibrium $\tilde{z}_t$ change at $t = 0$, meaning that $z_{t\to 0^+} = z_{C1} \neq \tilde{z}_{t\to 0^+}$. This causes the evolution to turn dynamic thereafter, governed by the following well-known initial value problem:

$$\begin{cases} M\ddot{z}_t + (K + K_2)\, z_t = (K + K_1 + K_2)\, z_{C1} \\ z_0 = z_{C1} \\ \dot{z}_0 = 0 \end{cases} \quad \text{for } t \geq 0\,, \tag{4.5}$$

which holds up to the breakage of spring 2, provided that it occurs. Eq. (4.5) admits analytical resolution, yielding the following temporal law for z_t:

$$z_t = (C_0 - C_1 \cos(\omega_0 t))\, z_{C1} \quad \text{for } t \geq 0\,, \tag{4.6}$$

where:

$$C_0 = \frac{K + K_1 + K_2}{K + K_2}\,, \quad C_1 = \frac{K_1}{K + K_2}\,, \tag{4.7}$$

and ω_0 stands for the system's natural frequency:

$$\omega_0 = \sqrt{\frac{K + K_2}{M}}\,. \tag{4.8}$$

As such, at $t = 0$ the system starts an oscillatory harmonic motion of semi-amplitude $C_1\, z_{C1}$ centred at the new state of quasi-static equilibrium $\tilde{z}_{t\geq 0} = C_0\, z_{C1}$. Therefore, neglecting the inertial effects would lead to underpredicting the maximum elongation reached by spring 2. Particularly for a structural system in which $C_0 z_{C1} < z_{C1} + \Delta z_C < (C_0 + C_1) z_{C1}$, the quasi-static analysis would not foresee breakage of spring 2, i.e. z_t reaching z_{C2}, in contrast to what is predicted dynamically.

From an energetic perspective, quasi-static models pursue the minimization of the system's potential energy at each instant. Consequently, the resulting evolutions are constrained neither by the temporal continuity of z_t nor by the conservation of the total energy, yet these two aspects are pivotal for actual massive systems. Indeed, the deformation energy of spring 1 is lost as soon as it breaks, but that of the other two is initially retained. Hence, the dynamic system begins to oscillate with an excess of potential energy in comparison to the new quasi-static equilibrium state, since $z_{t\to 0^+} = z_{C1} \neq \tilde{z}_{t\to 0^+} = C_0 z_{C1}$. This energy surplus fuels the system's oscillatory motion, cyclically exchanging potential and kinetic energy while their sum is conserved. As a result, the dynamic system can reach higher deformations than the quasi-static one, and the former's maximum elongation z_t for $t > 0$ is achieved as soon as all the kinetic energy is reverted back into deformation energy.

Furthermore, Eq. (4.6) shows that the evolution of the dynamic system is continuous in time and governed by the natural frequency ω_0, so that no immediate mechanical responses are possible. When generalized to a continuum, such a condition forces the mechanical information to propagate at a finite material-dependent

velocity c. Nonetheless, the disregard of the concept of time in quasi-static approaches renders "instantaneous" both the diffusion of information and the system's reactions to changes. These simplifications are thus expected to noticeably undermine the representativeness of quasi-static predictions upon unstable fracture, since the crack tip velocity is often on the same order of magnitude than c for such cases.

4.3 Case studies of unstable crack propagation

The preliminary rationale established along the previous subsection is now further developed through detailed analyses based on the PFM and on experiments conducted on 3D printed specimens. Both simulated and real setups were quasi-statically loaded under displacement control in a way that ensures unstable fracture. The placement of different interacting stress concentrators allowed to reproduce the multi-ligament interplay, as well as to modulate the magnitude of the energetic barrier for crack growth. Simulation-wise, the juxtaposition of the quasi-static and dynamic fracture predictions was achieved by using two different PFMs from the instant crack onset gets acknowledged onwards: one quasi-static (QS) and another one dynamic (DYN).

Just as in Section 3.3, the PFM/No-Tension/AT1 combination was here used given its proven good performance in modelling crack development under complex multiaxial stress states. Likewise, every PFM simulation was conducted under the assumption of 2D plane strain conditions. In any case, none of the presented conclusions is exclusive to these modelling choices. Moreover, first order triangular elements of size $\ell/4$ were once again used for domain discretization, without mesh refinement so as to avoid wave reflections caused by coarser elements. The same uniformly fine meshes were used in the quasi-static simulations in order to avoid any distortion that could compromise the comparison with the dynamic solutions.

The considered material properties and modelling parameters are reported in Table 4.1, which are representative of the elastic and ultimate behaviour of the Formlabs® Clear Resin used for the experimental campaign. This material is a thermoset polymer for which cross-linking is photo-triggered. As such, controlled passages of a moving laser beam allows for selective hardening of the resin, eventually generating the 3D specimen layer by layer through the Stereolithography (SLA) technique. The resulting methacrylated polymer presents a mechanical behaviour akin to others commonly used for fracture testing, e.g. PMMA, showcasing strong

non-linearities under heavy loading and a mostly-brittle fracture. In order to reduce the non-linear behaviour, the post-print curing process was performed at 75°C for 60 minutes, following what was reported in [104]. However, the experimental campaign here undertaken serves only as a qualitative validation of the simulations; extensive material characterization procedures or complex constitutive relations are thereby beyond the scope of the present chapter.

Table 4.1 Material properties and modelling parameters used for the PFM simulations.

ρ	E	ν	G_C	ℓ	σ_C^{NT}
$[\mathrm{Kg/m^3}]$	$[\mathrm{MPa}]$	$[-]$	$[\mathrm{MPa \cdot mm}]$	$[\mathrm{mm}]$	$[\mathrm{MPa}]$
1180	2800	0.35	0.4	0.16	65.0

The 3D printed specimens were tested using the DEBEN® Microtest 5kN tensile stage shown in Fig. 4.2. Global quasi-static conditions were ensured by setting the crosshead velocity to 1 mm/min. On the other hand, the specimen thickness was limited to 4 mm by the fixtures, thereby not showcasing pure plane strain conditions. Either way, such a thickness was deemed admissible since the comparison between simulations and experiments is only qualitative.

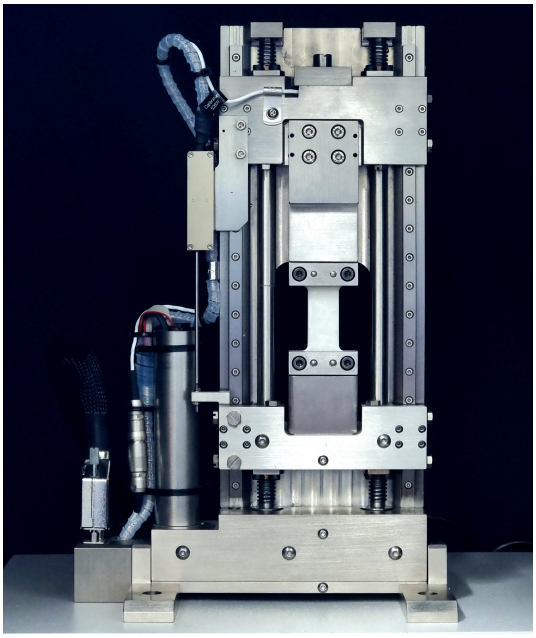

Fig. 4.2 DEBEN® Microtest 5kN tensile stage used for testing the 3D printed specimens.

The load applied to the specimens was measured using the machine's built-in 5 kN load cell, while the elongation was determined via a self-developed virtual extensometer. This optical technique tracked the position of two coloured optical markers, each adhered to one end of the gauge section, allowing to avoid the intrinsic distortion of crosshead displacement readings and maintain the measuring precision in the order of microns and a high accuracy, which resulted essential given the small size of the specimens. For more details on the virtual extensometer technique, please refer to Appendix B.

4.3.1 Case study A: Evidencing the kinetic energy contribution to unstable crack growth

The first case study here presented involves a uniaxially-tensioned specimen that contains a U-notch aligned with a circular hole, as schematically depicted in Fig. 4.3. As such, it represents a straightforward particularization of the generic multi-ligament setup from Section 4.2. There are two main reasons for choosing this particular geometry: (i) the smoothness of the stress concentrators improves both the manufacturing and simulation accuracy, and (ii) the failure sequence is theoretically certain and foreseeable. In particular, this latter characteristic is essential for ensuring the soundness of the comparison between quasi-static and dynamic simulations, as well as with the experiments.

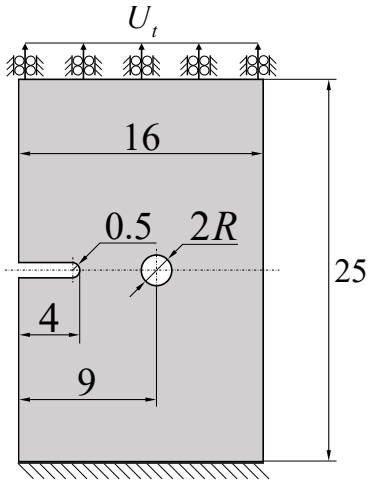

Fig. 4.3 Geometrical definition of the specimen type A. Dimensions in millimetres.

For the given setup, fracture is always expected to nucleate from the tip of the U-notch when $U_t = U_{C1}^{\{QS,DYN\}}$, an event hereafter referred to as primal crack onset (see Fig. 4.4a). Following this, the crack propagates unstably along the first ligament, eventually generating a longer U-notch with radius R once it reaches the hole. Depending on the severity of the new U-notch stress concentration compared with the original's, the elongation at secondary crack onset $U_C^{\{QS,DYN\}}$ (see Fig. 4.4b) will be equal to $U_{C1}^{\{QS,DYN\}}$ or not: the longer (blunter) the U-notch, the higher (lower) its stress concentration. As such, it is the hole radius R what determines the magnitude of the energetic barrier for crack growth, with bigger holes being more difficult to overcome. A parametric analysis on the specimen type A with R as the single free parameter would thus reveal the existence of two differentiated failure regimes: one where both primal and secondary crack onset take place at the same elongation (Regime I), and another in which they do not (Regime II).

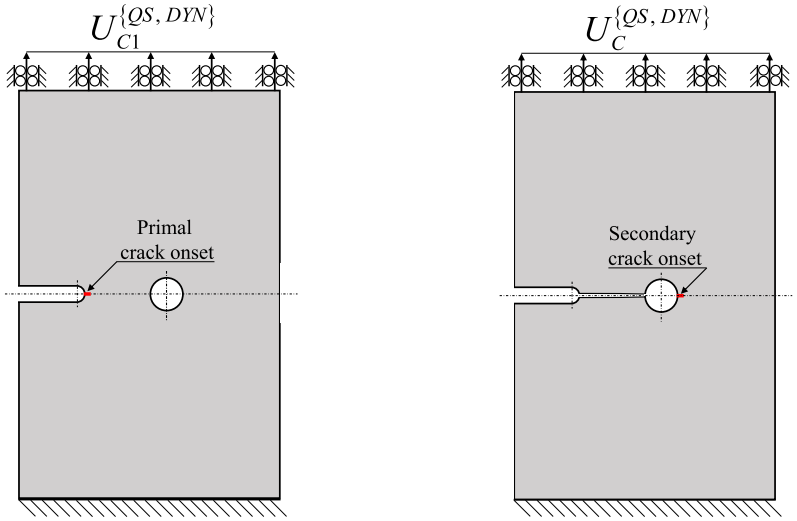

Fig. 4.4 Schematic representation of: (a) the specimen type A state upon primal and (b) secondary crack onset.

The critical elongations that trigger the primal and secondary crack onset according to the quasi-static PFM, namely U_{C1}^{QS} and U_C^{QS}, are depicted in Fig. 4.5a as the frontier between specimen states. This chart should be interpreted vertically from bottom to top, with each iso-R line indicating the evolution of the specimen failure state as U_t increases. From this, the existence of the two distinct failure regimes depending on R is evident, the transition taking place at $R_*^{QS} \approx 0.675$ mm.

For $R < R_*^{QS}$, quasi-static simulations show that the hole does not stop crack propagation, specimen failure thus being in Regime I ($U_{C1}^{QS} = U_C^{QS}$). Conversely for $R > R_*^{QS}$, the hole's energetic barrier becomes large enough to showcase failure in Regime II ($U_C^{QS} > U_{C1}^{QS}$). In these latter instances, U_C^{QS} results to be approximately proportional to a decimal root of R, which is aligned with the literature findings on the failure size-effect from U-notches [105]. On the other hand, the corresponding predictions of the dynamic PFM are presented in Fig. 4.5b. The two differentiated failure regimes are again clear, but now the transition occurs at a significantly larger threshold $R_*^{DYN} \in (1.75, 2.00)$ mm. Remarkably, the dynamic PFM predicts an abrupt transition of the failure regime in contrast with the continuity foreseen by the quasi-static counterpart.

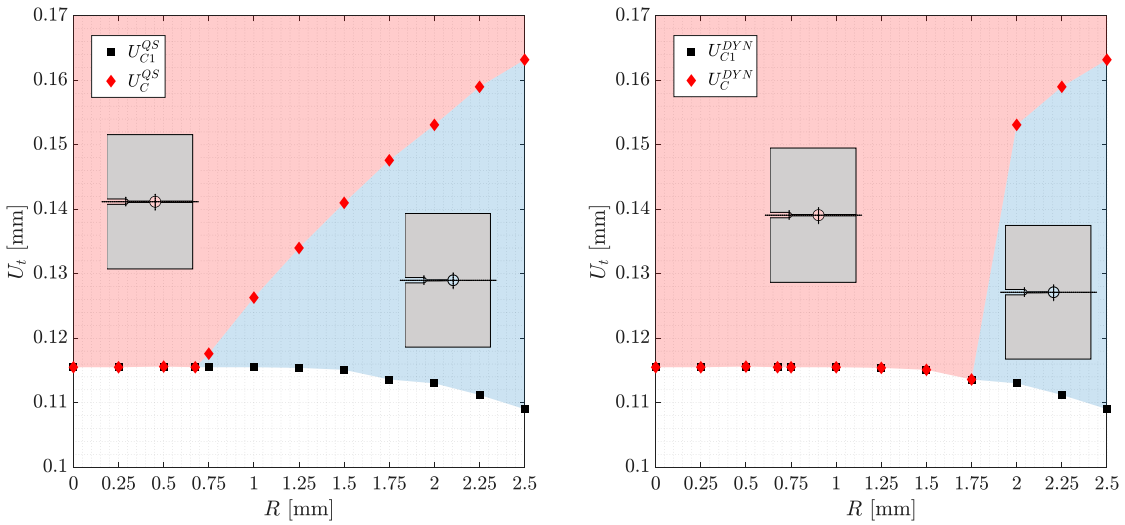

(a) (b)

Fig. 4.5 Specimen type A failure map per: (a) the quasi-static, and (b) the dynamic PFM.

This fundamental difference primarily stems from the energetic transformations that take place during the development of fracture according to each of the two models. Setting $R = 1.5$ mm for instance, the quasi-static PFM predicts the evolution of the energetic components as depicted in Fig. 4.6. Specifically, Fig. 4.6a shows that the behaviour is mostly linear-elastic up to the primal crack onset at $U_t = U_{C1}^{QS}$, when the first ligament breaks completely. Due to the inability of quasi-static models to follow unstable crack propagation events, these "develop" entirely within the AltMin iteration at each time step. In this regard, Fig. 4.6b details the energetic

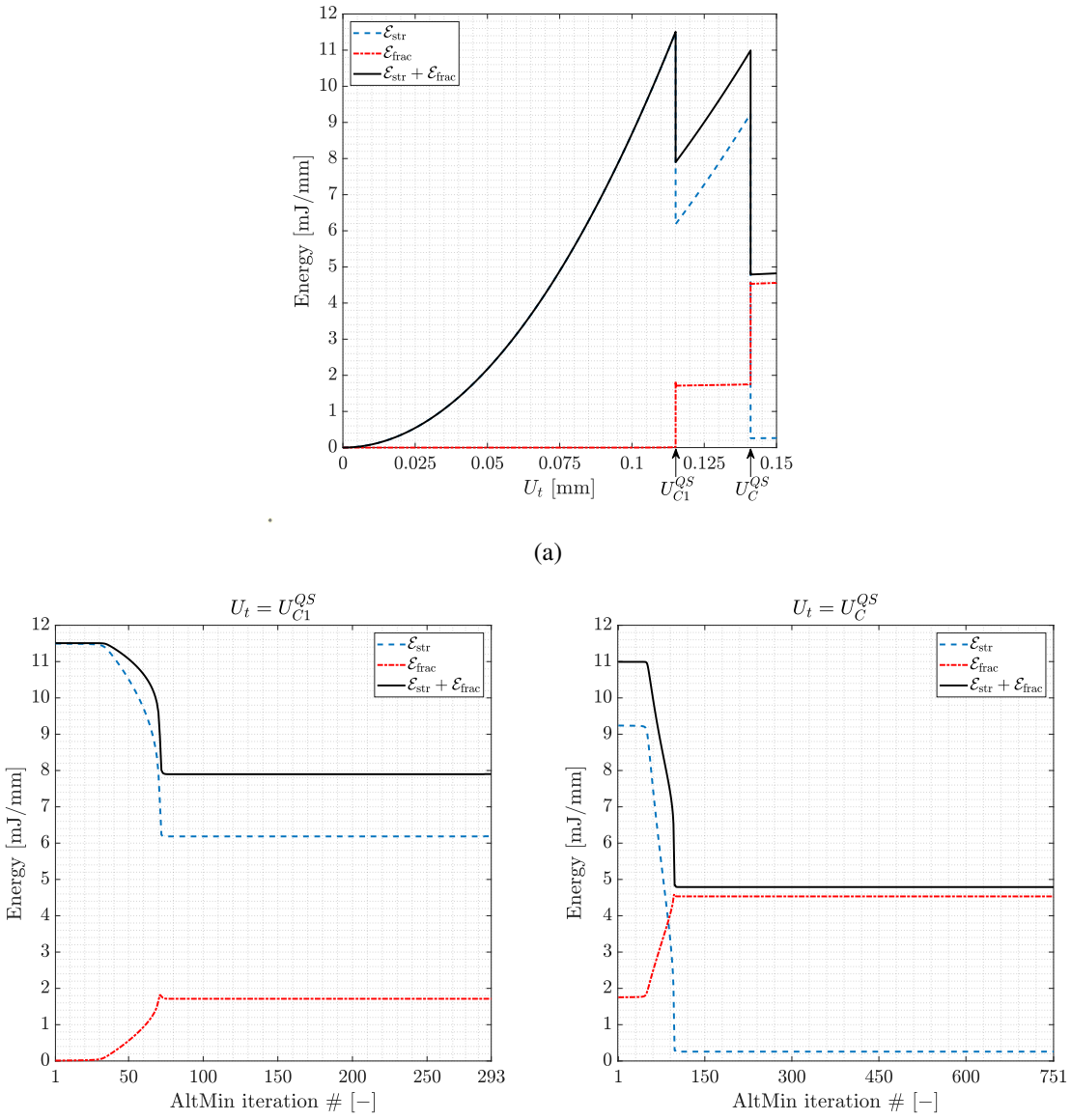

Fig. 4.6 Evolution of the energetic components along the fracturing of a specimen type A with $R = 1.5$ mm per the quasi-static PFM.

transformations occurring within the AltMin scheme for $U_t = U_{C1}^{QS}$. These results clearly show that $\mathscr{E}_{\text{frac}}$ increases and $\mathscr{E}_{\text{str}}$ decreases as the crack "propagates" along the first ligament. However, their variances are unbalanced so that the system's potential energy $\mathscr{E}_{\text{str}} + \mathscr{E}_{\text{frac}}$ has shrunk by 30% once the crack reaches the hole. At this point, the system lacks enough stored energy to trigger the secondary crack onset,

thus halting crack propagation at the hole. Additional strain energy is needed to resume crack propagation into the second ligament, which is achieved by increasing the specimen elongation. Secondary crack onset eventually happens when $U_t = U_C^{QS}$, as described in Fig. 4.6c. Afterwards, the specimen is completely broken, with all the system's energy being in the form of $\mathscr{E}_{\text{frac}}$ but for a small $\mathscr{E}_{\text{str}}$ term arising from the numerically-required non-zero residual stiffness.

As anticipated, quasi-static PFM simulations feature the "snap-back" discontinuity, which is the manifestation of crack instability under displacement control. Traditionally, this has been studied by introducing an artificial mechanism that draws energy out of the system and enables quasi-static equilibrium conditions by stabilizing fracture (see e.g. [97]). This can be accomplished for instance by explicitly controlling the crack extension or the crack mouth opening displacement. Nonetheless, introducing such a energy depletion scheme changes the nature of the modelled system with respect to that under study, thus affecting its representativeness.

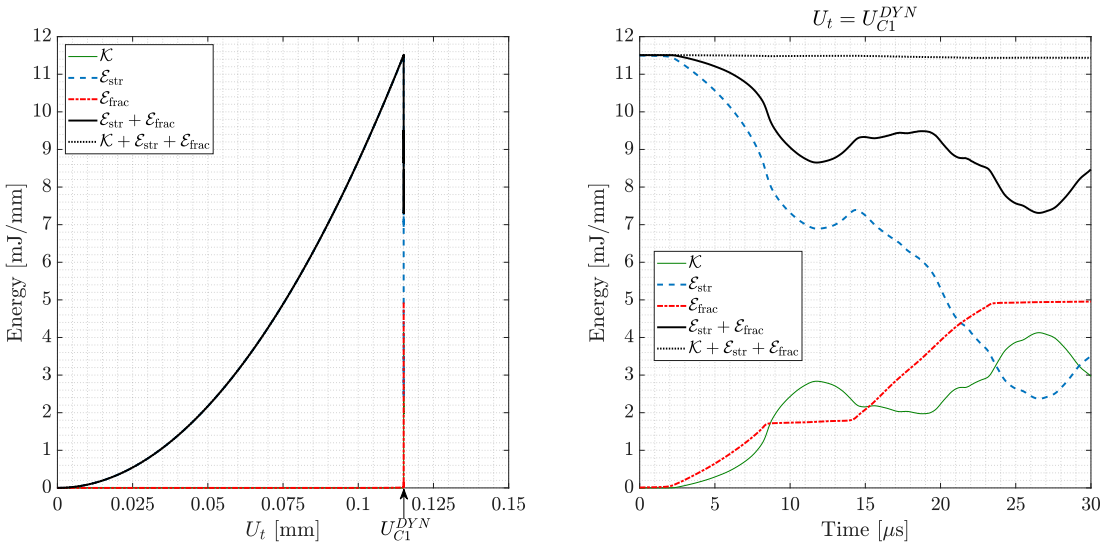

(a) (b)

Fig. 4.7 Evolution of the energetic components along the fracturing of a specimen type A with $R = 1.5$ mm per the dynamic PFM.

An alternative, less intrusive approach to unstable fracture consists in assuming dynamic equilibrium conditions instead. In a temporally continuous framework, the excess of potential energy released during crack growth gets entirely converted

into kinetic energy $\mathscr{K}$, thereby preserving the system's total energy. As demonstrated in [27] however, the dynamic PFM only conserves the system's total energy asymptotically as the time steps vanish. Nonetheless, using a reasonably small time increment leads to almost imperceptible total energy losses as shown in Figs. 4.7 for $R = 1.5$ mm. For comparative purposes, Fig. 4.7a is analogous to Fig. 4.6a, whereas Fig. 4.7b is somewhat the dynamic counterpart to Figs. 4.6b and 4.6c combined, but with the X-axis representing the temporal coordinate of the dynamic PFM.

As anticipated by Fig. 4.5b, the dynamic PFM foresees Regime I failure for $R = 1.5$ mm, thus showcasing a single fracturing event at $U_t = U_{C1}^{DYN} = U_C^{DYN}$ in Fig. 4.7a. The energetic transformations detailed in Fig. 4.7b demonstrate that the system's total energy is mostly conserved during the fracturing process, since the reduction in potential energy is compensated by an increase in kinetic energy. This turns out crucial barely after the crack reaches the hole, when the accumulated kinetic energy begins to revert partially into strain energy (from $t = 11.8\mu$s to $t = 14\mu$s in Fig. 4.7b). Such a partial back-conversion eventually allows the system to overcome the hole's energetic barrier and trigger the secondary crack onset without further specimen elongation.

Moreover, the cases here examined showed that even if both quasi-static and dynamic approaches agree in predicting Regime II failure, the latter still yields larger values of α at the site of secondary crack onset just after crack arrest. This discrepancy can also be traced back to the partial recovery of strain energy, which can still cause α to grow therein in spite of not being enough to nucleate fracture. Nonetheless, the critical elongations U_C^{QS} and U_C^{DYN} turned out to be indiscernibly equal for such cases. This finding aligns with the results reported in [21] for the unstable growth of a cohesive-modelled crack in a cantilever specimen with an array of relatively large circular holes.

Experimental results

The conducted experimental tests were designed to juxtapose the two-ligament unstable fracturing behaviour against the quasi-static secondary crack onset, i.e. the energetic barrier. For this purpose, two main types of specimens with the same value of R were used: one where both ligaments were load bearing (see Fig. 4.4a), and another where only the second was (see Fig. 4.4b). Apart from that difference, both kinds of specimens are identical. As such, if samples from the former group

were to fracture in Regime I at a lesser elongation than those of the latter kind, it would represent indisputable proof that the dynamic effects upon unstable crack propagation are significant.

Overall, twelve specimens type A with $R = 0.5$ mm (nominal) were 3D printed. The actual specimen geometry was designed so that the domain 25 mm overall length corresponded to the initial distance between the optical markers, i.e. the gauge length (see Fig. 4.8). Preliminary experiments revealed that, due to the combined effect of the material high-brittleness and complex behaviour with the presence of surface defects, it was no longer guaranteed that fracture nucleates from the U-notch tip. Towards minimizing the need for post-mortem analyses while ensuring the desired failure sequence, a small incision was performed at the notch tip with a razor blade. This is akin to decreasing the effective radius of the notch, or somewhat like increasing R while maintaining the nominal notch.

Fig. 4.8 Video frame of specimen type A1 with $R = 0.5$ mm (nominal) showing the digital recognition of the green (upper) and red (lower) markers. Each cross represents a marker barycentre (see Appendix B).

The effective reduction of the notch radius was quantified by comparing the fracture load of the two-ligament specimens without (type A) and with the cut (type A1), with four specimens of each kind tested. The adequacy of the failure sequence in the former group was individually verified by post-mortem analyses. The experimental results obtained for the ultimate elongation U_C^{EXP} and force F_C^{EXP} are given in Tables 4.2 and 4.3, which yield that the cut reduced the ultimate force

by an average factor of 3.17. This ratio, combined with a maximum stress criterion and the approximated U-notch stress field from [106], allows to estimate an effective notch radius after the cut of 0.28 mm. Consequently, specimens type A1 can be regarded as equivalent to the $R = 1.75$ mm simulations from Subsection 4.3.1, in that both present the same effective ratio of notch to hole radii.

Lastly, the remaining four specimens form another control group in which only the second ligament was load-bearing (type A2). The corresponding experimental results given in Table 4.4 unequivocally demonstrate, alongside those in Table 4.3, that despite specimens A1 show failure in Regime I, they break at considerably smaller elongations than those of type A2. This provides empirical evidence supporting what was hitherto theoretically asserted, i.e. that dynamic effects upon unstable crack growth are substantial even under quasi-static loadings.

Table 4.2 Experimental results for the specimens type A.

	Specimen #				**Overalls**	
	1	**2**	**3**	**4**	**Avg.**	**CoV %**
$U_{C,A}^{EXP}$ [mm]	0.30	0.35	0.35	0.42	0.36	13.70
$F_{C,A}^{EXP}$ [N]	1540.3	1806.6	1727.9	1983.6	1764.6	10.42

Table 4.3 Experimental results for the specimens type A1.

	Specimen #				**Overalls**	
	1	**2**	**3**	**4**	**Avg.**	**CoV %**
$U_{C,A1}^{EXP}$ [mm]	0.07	0.09	0.11	0.08	0.09	19.00
$F_{C,A1}^{EXP}$ [N]	477.7	577.4	600.7	570.0	556.7	9.73

Table 4.4 Experimental results for the specimens type A2.

	Specimen #				**Overalls**	
	1	**2**	**3**	**4**	**Avg.**	**CoV %**
$U_{C,A2}^{EXP}$ [mm]	0.45	0.36	0.43	0.30	0.39	17.59
$F_{C,A2}^{EXP}$ [N]	984.4	779.8	996.3	761.2	880.4	14.45

4.3.2 Case study B: Revealing the significance of sequential and progressive diffusion of mechanical information

As introduced in Section 4.2, another key aspect to consider upon unstable crack propagation is how the quasi-static and dynamic approaches handle the diffusion of mechanical information within the continuum. In real materials, this takes place through pressure waves that travel at the corresponding speed of sound $c \propto \sqrt{E/\rho}$, thereby implying that any evolving process is inherently dynamic. However, if and only if the rate of every mechanical change in the system is slow enough, one can disregard the dynamic effects and develop predictive models that take advantage of quasi-static simplifications. This condition is not typically satisfied for unstable fracturing conditions however, for the crack tip velocity and c are often of the same order of magnitude in such cases.

In particular, quasi-static models present "instantaneous" transmission of the mechanical information for they disregard the concept of time. This implies that any arbitrarily distant point immediately gets aware of and reacts to changes in the system's mechanical configuration. In the context of unstable fracture, such an immediacy leads to the whole domain changing its deformation state while the crack is growing, which in turn influences both future crack growth and deformation states. In reality, right after fracture nucleation only the immediate vicinity of the new crack receives notice of its growth and starts to adapt to the new configuration. As such, quasi-static approaches predict states that significantly dissent with those physically admissible with regards to the mechanical information diffusion.

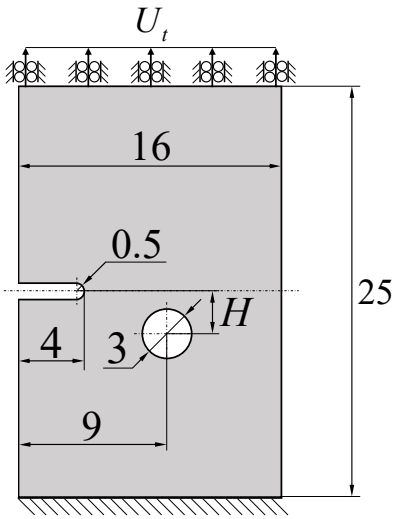

Fig. 4.9 Geometrical definition of the specimen type B. Dimensions expressed in millimetres.

The significance of such an issue will be here examined with the specimen type B defined in Fig. 4.9, which results from modifying a specimen type A with $R = 1.5$ mm by vertically separating the notch and the hole by a distance H. As a result, the interaction between the two stress concentrators becomes more complex, and so do the resultant crack patterns. In this sense, one can anticipate a crack that initially propagates horizontally and then gradually veers towards the hole. For small enough values of H, the crack reaches the hole and the aforementioned competition between halting or resuming crack growth takes place. Otherwise, the crack misses the hole and a single cracking event occurs. This fundamental difference in the resultant fracturing behaviour hinges on the crack's ability to change direction, which is in turn ruled by its interaction with the hole during propagation. Consequently, any delays in how the diffusion of mechanical information is modelled materialize as less pronounced changes of crack direction. As such, differences in this regard have the potential on its own to change whether the crack impinges the hole or not.

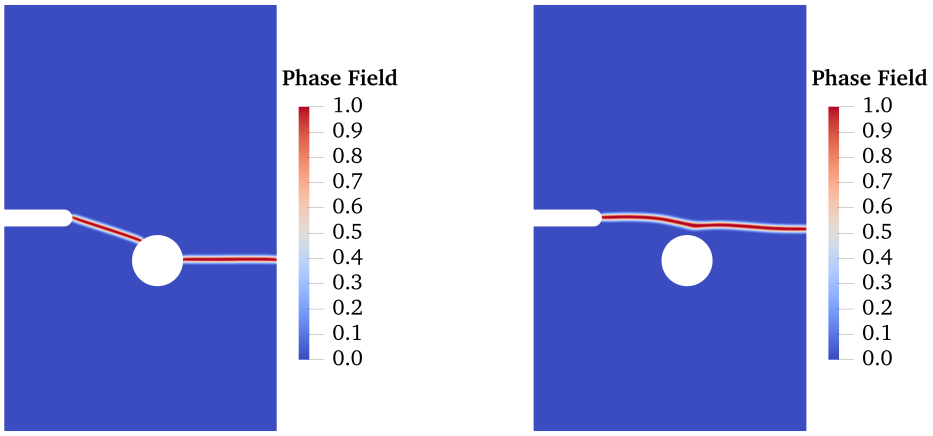

(a) (b)

Fig. 4.10 Crack patterns according to (a) the quasi-static and (b) the dynamic PFM for a specimen type B and $H = 2.5$ mm.

For the specific configuration under study, the quasi-static and dynamic PFM dissent in this sense when $H = 2.5$ mm, as shown in Figs. 4.10. Besides this, it is worth noting that the quasi-static PFM unexpectedly predicts a piecewise straight crack pattern, in contrast to the curved path that emerges when inertial effects are incorporated. A detailed analysis on the underlying reasons behind such a surprising prediction uncovers a significant inconsistency of quasi-static approaches upon

unstable crack growth: the weakening of the essential irreversibility condition of fracture.

As outlined in Section 2.2, the quasi-static PFM pursues the local minimization of the system's potential energy conditioned by an irreversibility constraint on α. However, this crucial admissibility condition is only enforced with respect to previously converged states, and so changes in α occurring within the AltMin scheme at a given time step are reversible. This reveals paradoxical in that the quasi-static PFM is able to "correct" crack patterns from past AltMin iterations as long as convergence is not reached, yet based on information that only becomes available once such states would have been reached.

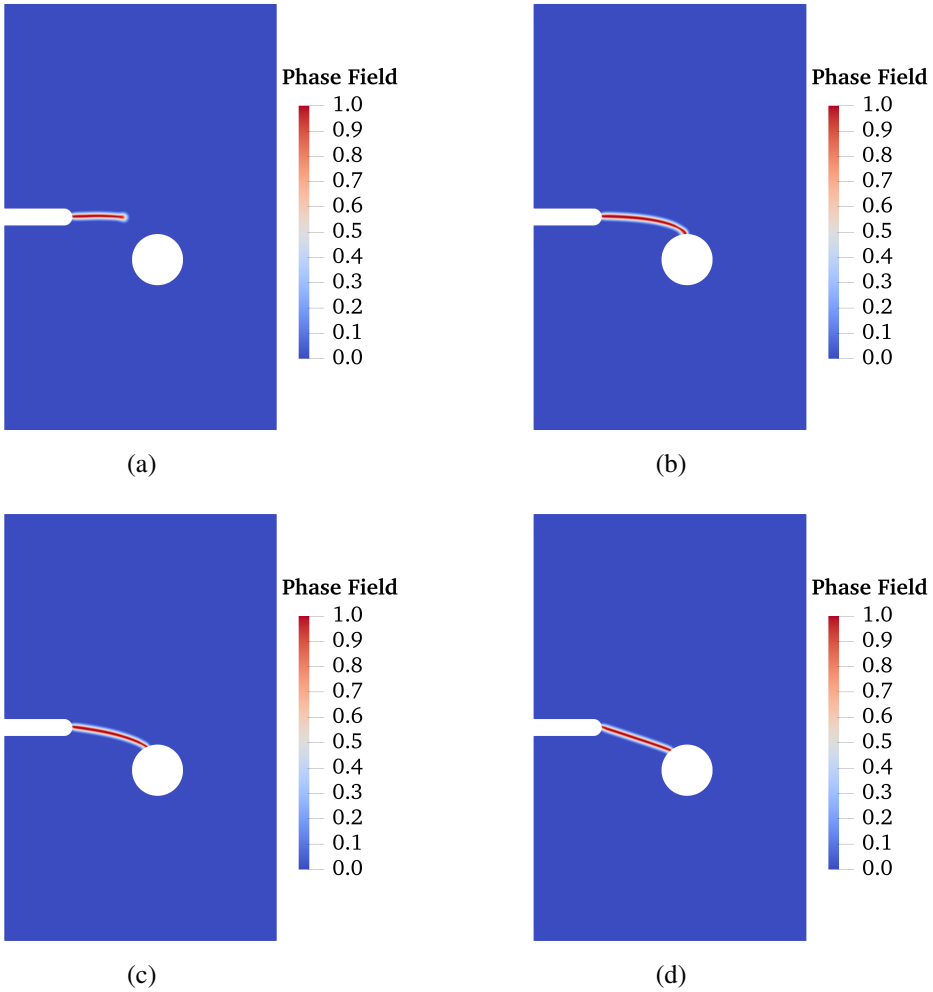

Fig. 4.11 Cracking of the first ligament in a specimen type B with $H = 2.5$ mm as predicted by the quasi-static PFM after: (a) 100, (b) 500, (c) 1500 and (d) 4500 AltMin iterations.

This line of reasoning is supported by the results in Fig. 4.11, which illustrate the crack patterns at various AltMin iterations for the time step where the first ligament breaks, i.e. when $U_t = U_{C1}^{QS}$. As seen in Figs. 4.11a and 4.11b, the crack initially follows the curved path that is expected beforehand, confirming that the deformation state drives the crack to be as such before it impinges the hole. Nonetheless, once the first ligament is completely broken, the curved crack practically results in the same reduction of $\mathscr{E}_{\text{str}}$ as if straight, but it is more expensive in terms of $\mathscr{E}_{\text{frac}}$. At the same time, the irreversibility condition is enforced with respect to the latest converged result prior to crack onset, which was an essentially pristine state. Thereof, it results admissible for the quasi-static PFM to straighten the crack once it has reached the hole, as evident from Figs. 4.11b through 4.11d. This way, the quasi-static system ends up breaking the first ligament with a straight crack, for it is allowed to do so and it leads to a bigger reduction in the potential energy (see Fig. 4.12). The oxymoron reveals evident: while a straight crack is energetically optimal once the first ligament is broken, the deformation state drives the crack to propagate along a curved path from the notch to the hole. Therefore, considering that fracture is irreversible, the straight crack solution can only be achieved by contravening the cause-effect principle.

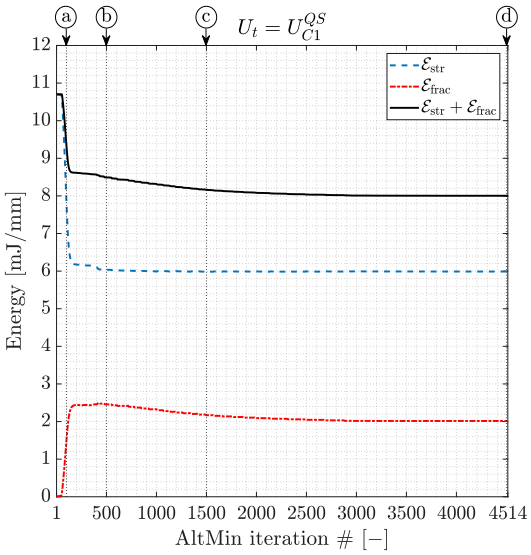

Fig. 4.12 Evolution with the AltMin iterations of the energetic components along the fracturing of the first ligament of a specimen type B with $H = 2.5$ mm according to the quasi-static PFM. Bullet notes on top indicate correspondence with Figs. 4.11.

Experimental results

Although the theoretical discussion above is comprehensive and robust, supporting experimental evidence is also provided herein. In this sense, a single specimen type B with $H = 2.5$ mm, analogous to those numerically simulated, was 3D printed and tensile tested. Following the rationale already presented in Subsection 4.3.1, a slight incision was made at the notch tip with a razor blade. It is noteworthy that the experimentally-obtained crack pattern shown in Fig. 4.13a is not only curved but it also matches closely the prediction by the dynamic PFM (see Fig. 4.13b).

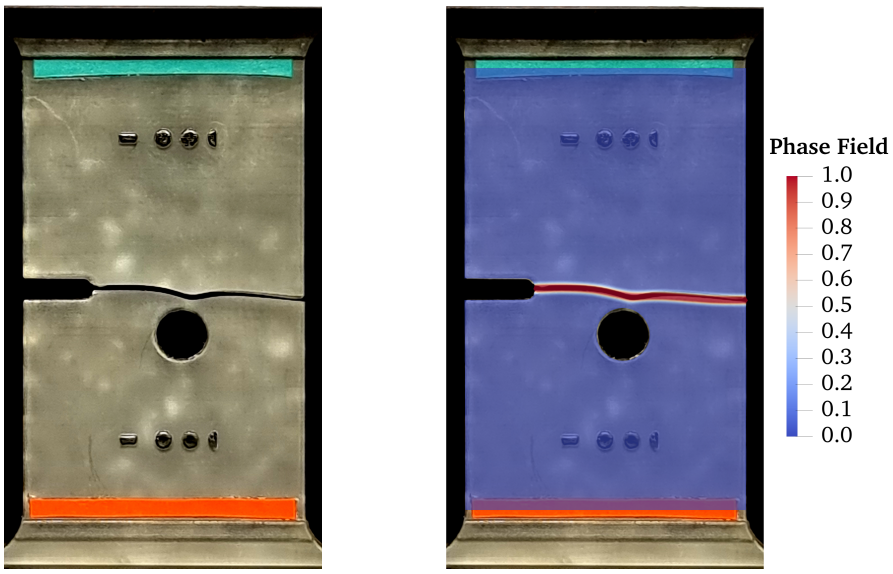

(a) (b)

Fig. 4.13 (a) Picture of the experimental crack pattern of a specimen type B with $H = 2.5$ mm and (b) superposition with the predictions by the dynamic PFM.

4.4 Conclusions

This chapter provides comprehensive theoretical, numerical and empirical evidence proving that the fundamental hypothesis of the quasi-static variational models of fracture does not hold in the event of unstable crack propagation, even when the loading is quasi-static. Consequently, neglecting the inertial effects leads to intrinsically unrealistic models that yield potentially unsafe predictions, as demonstrated with a simplified Spring-Mass model of multi-ligament fracture. This simplistic model

resulted enough to identify the two primary characteristics of quasi-static models that render their fracture predictions unrepresentative: the neglection of the kinetic energy component, and the instantaneous propagation of mechanical information.

Based on these initial observations, two distinct case studies were designed to emphasize each of the two aforementioned shortcomings. The well-established Phase Field fracture model was used since it is capable of dealing with bulk fracture, and both quasi-static and dynamic formulations are available. Additionally, the numerical findings are supported by experimental results from tests on bespoke 3D printed specimens. Out of these comprehensive case studies, three key points should be highlighted:

- The principle of local minimization of the potential energy leads to the prediction of an unrealistic dissipation of energy upon unstable fracture. Often manifested as a snap-back discontinuity if under displacement control, most of this excess of energy is not actually disposed but converted into kinetic energy. This can then partially convert back into strain energy, further driving crack propagation in the presence of energetic barriers. Therefore, quasi-static predictions of unstable fracture are potentially unsafe for they overestimate the system's energy dissipation.

- Assuming quasi-static equilibrium upon rapidly changing evolutions allows to admit states that are unphysical because they require the mechanical information to travel faster than the speed of sound in the material. This assumption severely undermines the accuracy of the resultant crack patterns, and so, of the predicted unstable fracturing behaviour.

- The inability of quasi-static approaches to follow unstable crack propagation significantly weakens the robustness of the essential irreversibility condition for fracture and leads to admit as solutions states that violate the cause-effect principle.

To conclude, it is important to consider that the limitations observed in the quasi-static predictions are not unique to the Phase Field fracture model, but are common to many variational approaches to fracture. This, combined with the prevalence of unstable fracturing in real-world structures, even under quasi-static loading conditions, underscores the importance of the findings described in this study.

Chapter 5

Finite Fracture Mechanics[1]

5.1 Introduction

Despite its huge potential in the modelling of complex fracture processes, the Phase Field fracture model carries a considerable computational cost. At the same time, certain structural applications deem any degree of failure inadmissible, thereby making it enough to have crack nucleation criteria. In this regard, the prediction of failure onset from brittle and similar materials has classically been tackled by frameworks either based on local stress values or on infinitesimal energy balances. These two approaches are somewhat complementary in that those of the former kind work only for non-singular geometries, while sufficiently intense singularities in the elastic solution are a must for the latter ones. Cases in between, i.e. moderate stress raisers, are thereby out of reach for traditional crack onset criteria. All the more so, none of these formulations could explain the experimentally-observed size-effect of failure in plain geometries (see e.g. [107]).

In this context, Leguillon [39] theorized that failure onset is not an infinitesimal but a finite phenomenon whose occurrence is subjected to the simultaneous fulfilment of non-local stress and energy conditions. As such, the coupled criterion of Finite

[1]Part of the work described has been previously published in: **(i)** Chao Correas, A., Corrado, M., Sapora, A., Cornetti, P. (2021). Size-effect on the apparent tensile strength of brittle materials with spherical cavities. *Theor Appl Fract Mech* 119, 103120; and **(ii)** Chao Correas, A., Sapora, A., Reinoso, J., Corrado, M., Cornetti, P. (2023). Coupled versus energetic nonlocal failure criteria: A case study on the crack onset from circular holes under biaxial loadings. *Eur J Mech A Solids* 101, 105037.

Fracture Mechanics was born, which subsequently proved to be all-round robust in predicting crack onset, be it for plain, notched, slightly-cracked, or largely-cracked geometries. Following this same coupling paradigm, an analogous yet different formulation for the coupled criterion was later proposed by Cornetti and co-Authors in [40]. These two contributions are widely regarded as the main pillars of the modern Finite Fracture Mechanics framework.

Ever since its introduction, Finite Fracture Mechanics has proven versatile to deal with failure onset in the presence of widely varied stress raisers and quasi-static conditions. Concerning pure brittle failure in a linear elastic context, the approach has been successfully applied to singular geometries such as sharp cracks [108], V-notches [40, 109, 110], Penny-shaped cracks [77], rhomboidal holes [111], and squared holes [112], to mention but a few. Non-singular stress concentrators have also been at the centre of relevant investigations, as implementations are available for circular holes [113–115, 70], U-notches [116] and elliptical holes [117], among others. Crack nucleation in more complex multi-phase materials has also been tackled by Finite Fracture Mechanics, which has been used to predict interfacial delamination [118, 119], as well as the macroscopic failure of composite laminates [120–122] and concrete structures [123]. Dropping the hypothesis of linearity in the material behaviour to include more general laws, the approach was extended to hyper-elastic materials [124]. The showcased robustness of Finite Fracture Mechanics in predicting crack onset has been as well ascertained through comparisons with the Cohesive Zone Model [77, 79, 125] and the Phase Field fracture model [126, 80].

The present chapter serves as an introduction to the Finite Fracture Mechanics approach in a quasi-static context. In such regard, the generalized formulation is first put forward and then particularized per the proposals in [39] and [40]. The approach is then implemented to study the failure size-effect when it stems from a spherical void embedded in a uniaxially tensioned domain, which poses a relatively straightforward failure scenario. The obtained crack onset predictions are validated against the well-established Dugdale's Cohesive Zone Model, experimental results and atomistic simulations. On the other hand, the particularities of the Finite Fracture Mechanics approach upon intricate conditions for failure are evidenced through the case study of crack onset from circular holes under biaxial loadings. Once again, the resulting predictions are benchmarked against Dugdale's Cohesive Zone Model, which was already introduced in Subsection 2.4.3. As such, an indirect comparison with the Phase Field fracture model is also here undertaken.

5.2 The Finite Fracture Mechanics approach to quasi-static crack nucleation

The Finite Fracture Mechanics (FFM) framework [39, 40] posits that crack initiation is an instantaneous event that develops in finite spatial increments. Such a criterion hypothesizes that failure triggers at the minimum loading intensity for which both stress and energetic conditions are simultaneously fulfilled over any prospective crack growth surface. Rigorously speaking, no assumption on the size or shape of the critical finite surface is required *a priori*, which poses a great advantage in comparison with other comparable non-local failure criteria, namely the Theory of Critical Distances [38] or Quantized Fracture Mechanics [37]. Nonetheless, it should be pondered that FFM's theoretical robustness is not kept implementation-wise, since its resolution is quite arduous whenever the crack onset mechanisms are not well-defined.

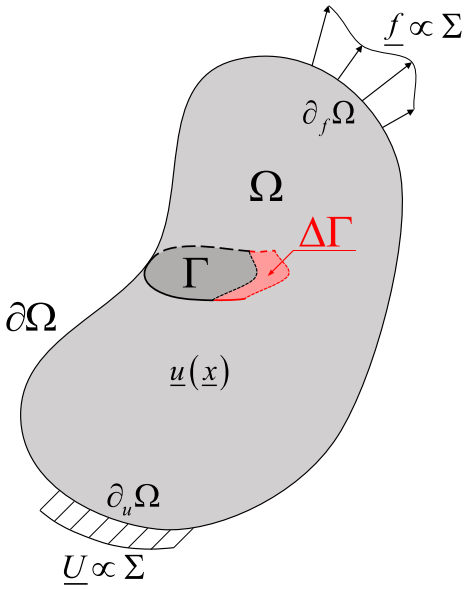

Fig. 5.1 Schematic representation of a fracture mechanics problem with the finite crack growth highlighted.

To write FFM's failure criterion in mathematical terms, let us consider the generic N-dimensional fracture problem in Fig. 5.1. There, $\Delta\Gamma \in \mathbb{R}^{N-1}$ represents any potential finite crack growth and Σ is a parameter governing the loading intensity, be it an imposed displacement, a concentrated force or distributed pressure. In its

original state ($\Delta\Gamma = \emptyset$), the domain Ω sees a stress field $\underline{\underline{\sigma}} \propto \Sigma$ and has a potential energy $\mathscr{P} \propto \Sigma^2$. Given a finite crack growth $\Delta\Gamma$, the system's potential energy varies as $\Delta\mathscr{P} \propto \Sigma^2$ due to the changes in the domain's mechanical configuration. Based on this, FFM defines two necessary and sufficient inequality conditions for failure: one based on the pre-cracking stress $\underline{\underline{\sigma}}$, and another related to the release of potential energy during the finite crack growth $\Delta\mathscr{P}$. Therefore, the corresponding set S of combinations of Σ and $\Delta\Gamma$ that could potentially trigger failure generically writes as:

$$\mathrm{S} = \left\{ \Sigma \times \Delta\Gamma \in \mathbb{R} \times \mathbb{R}^{N-1} \left| \begin{array}{l} h\left(\underline{\underline{\sigma}}(\Sigma), \Delta\Gamma\right) \geq \sigma_C \quad \text{and} \\ g\left(\Delta\mathscr{P}\left(\Delta\Gamma, \Sigma\right)\right) \geq G_C \end{array} \right. \right\}, \tag{5.1}$$

with h and g being two monotonically increasing functions with respect to each of their corresponding inputs. Among all the combinations of Σ and $\Delta\Gamma$ that belong to S, FFM identifies the one minimizing Σ as that actually triggering fracture, and so:

$$\left(\Sigma_f, \Delta\Gamma_f\right) = \underset{(\Sigma, \Delta\Gamma) \in \mathrm{S}}{\arg\min} \left(\Sigma\right). \tag{5.2}$$

With respect to the particular choices of the non-local conditions for fracture, two main variants exist: the original pointwise-stress proposal [39] and the averaged-stress modification [40]. In both cases, the finite energy balance is identical, their difference residing instead in the non-local stress condition. In what follows, these two variants will be referred to as FFM-orig and FFM-avg, respectively, whereas the FFM acronym will be reserved for the Finite Fracture Mechanics framework as a whole. For the sake of simplicity, only pure Mode I crack onset conditions will be considered in what follows (including throughout Chapter 6).

5.2.1 Original formulation

The original FFM formulation [39] requires that, for failure to occur, the pre-failure crack opening stress component σ must point-wise meet or exceed the material tensile strength σ_C throughout $\Delta\Gamma$. At the same time, failure can only occur if the decrease of potential energy $\Delta\mathscr{P}$ is at least equal to the energy consumed by the finite crack growth $\Delta\Gamma$. Therefore, the resulting set $\mathrm{S}_{\mathrm{orig}}$ of Σ and $\Delta\Gamma$ combinations

for which FFM-orig reckons failure to be feasible is defined as:

$$\mathrm{S_{orig}} = \left\{ \Sigma \times \Delta\Gamma \in \mathbb{R} \times \mathbb{R}^{N-1} \left| \begin{array}{cc} \sigma(\underline{x}, \Sigma) \geq \sigma_C \ \ \forall \underline{x} \in \Delta\Gamma & \text{and} \\ \Delta\mathscr{P}(\Delta\Gamma, \Sigma) \geq G_C \mathscr{H}^{N-1}(\Delta\Gamma) & \end{array} \right. \right\}, \tag{5.3}$$

where $\mathscr{H}^{N-1}$ represents the $N-1$-dimensional Haussdorf measure of $\Delta\Gamma$.

5.2.2 Averaged stress formulation

The other major FFM formulation [40] couples the Neuber-Novozhilov [35, 36] non-local stress condition with the above presented finite energy balance. In this context, FFM-avg theorizes that it is the average of σ all along $\Delta\Gamma$ that has to exceed σ_C, rather than its punctual values therein. The averaged-stress condition can be thereby deemed weak as opposed to the strong requirement of the original FFM variant. As such, the former yields more conservative failure predictions, i.e. lower values of Σ_f. The corresponding failure admissibility set $\mathrm{S_{avg}}$ therefore writes as:

$$\mathrm{S_{avg}} = \left\{ \Sigma \times \Delta\Gamma \in \mathbb{R} \times \mathbb{R}^{N-1} \left| \begin{array}{cc} \displaystyle\int_{\Delta\Gamma} \sigma\left(\underline{x}, \Sigma\right) \mathrm{d}\underline{x} \geq \int_{\Delta\Gamma} \sigma_C \, \mathrm{d}\underline{x} & \text{and} \\ \Delta\mathscr{P}\left(\Delta\Gamma, \Sigma\right) \geq G_C \mathscr{H}^{N-1}\left(\Delta\Gamma\right) & \end{array} \right. \right\}. \tag{5.4}$$

The underlying concept behind the averaged stress condition is to require the net force exerted by σ along $\Delta\Gamma$ to be at least equal than if a constant stress σ_C was applied over the same region. Such an averaged stress condition has proven advantageous with respect to the original proposal when applied to small-sized specimens [108], for which FFM-orig yields unrealistic predictions.

5.3 Case study on the crack onset from a spherical void in an uniaxially tensioned domain

The presence of a spherical void in an uniaxially tensioned and infinite domain (see Fig. 5.2a) causes the effective strength to diminish per the resulting stress concentration. The non-null stress gradient additionally entails that the strength reduction is

dependent on the pore size, a phenomenon that cannot be explained by local stress-based failure criteria. On the other hand, the geometry not being singular precludes the use of infinitesimal energetic approaches such as Linear Elastic Fracture Mechanics, even though these do reproduce the size-effect of failure. These limitations can be overcome by coupling non-local stress and energy conditions, which in turn enable capturing the size-effect of failure even for non-singular geometries.

For the case at hand, the stress field solution in the surroundings of the spherical cavity of radius R was given in [127]. The maximum crack opening stress pertains to the void's equator $(z = 0)$, wherein the distribution of σ_{zz} is as follows:

$$\sigma_{zz}(r,\Sigma_1)|_{z=0} = \Sigma_1 \left[1 + \frac{4-5\nu}{14-10\nu} \left(\frac{R}{r}\right)^3 + \frac{9}{14-10\nu} \left(\frac{R}{r}\right)^5 \right] = \Sigma_1 \, S_{zz}(r) \; , \quad (5.5)$$

for an imposed remote stress Σ_1 along the z direction. As it usually occurs for axisymmetric problems, the stress field depends on the material Poisson's ratio ν.

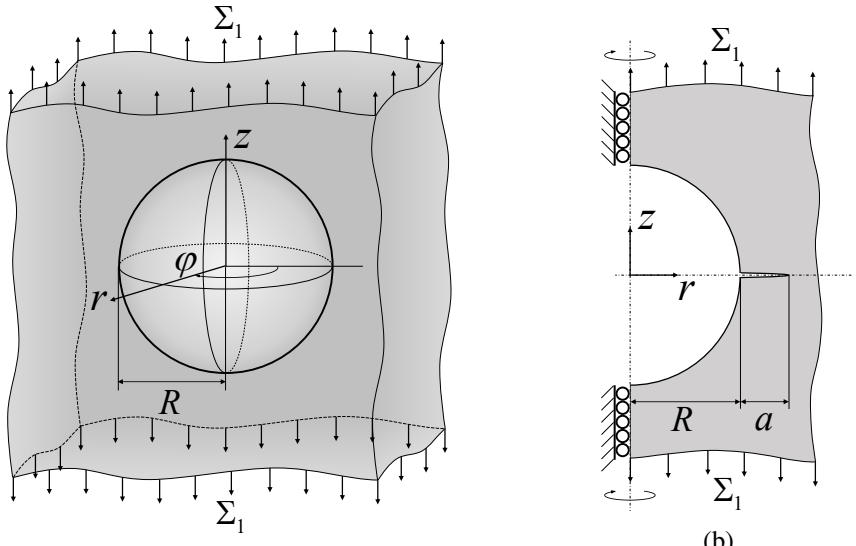

Fig. 5.2 Schematic representation of: (a) a spherical void in an infinite tensioned body in 3D and (b) its axisymmetric reduction featuring an annular crack.

Given the axial symmetry of the problem with respect to the z-axis, every internal magnitude is independent of the angular coordinate φ. As a consequence, also the crack growth is expected to be axisymmetric and to develop as annular cracks surrounding the void equator. This entails that the only degree of freedom for crack

growth is its width a, thus leaving the axial-symmetric reduction of the 3D cracking problem as in Fig. 5.2b.

Considering failure to develop as annular cracks in the equator plane leads to pure Mode I failure conditions. By virtue of Irwin's relation ($\{G, G_C\} = \{K_I, K_{IC}\}^2/E'$, where $E' = E/(1-\nu^2)$ for plane strain), the infinitesimal reduction of potential energy upon growth of an annular crack of width a can be thereby determined from only the corresponding Mode I Stress Intensity Factor K_I. By simplifying the interpolation procedure from [128], the following approximated expression for $K_I(a)$ was given in [79]:

$$K_I(a, \Sigma_1) = \Sigma_1 \sqrt{\pi a} F_{\Sigma_1}(a, R) \tag{5.6}$$

$$F_{\Sigma_1}(a) = \left(\frac{R}{R+5a}\right)^2 F_0 + \left[1 - \left(\frac{R}{R+5a}\right)^2\right] F_1(a) \tag{5.7}$$

$$F_0 = 1.122 \frac{27-15\nu}{14-10\nu} \tag{5.8}$$

$$F_1(a) = \frac{2}{\pi}\sqrt{\frac{a+2R}{a+R}}\left[1 + \frac{1}{2}\left(\frac{R}{a+R}\right)^2 + \frac{3}{7-5\nu}\left(\frac{R}{R+a}\right)^4\right] \tag{5.9}$$

where F_0 is the shape factor for an edge crack subjected to a remote tensile stress equal to the maximum stress concentration, i.e. at the pore equator, and F_1 is the shape function of a Penny-shaped crack to which the stress distribution σ_{zz} from Eq. (5.5) is applied over the corona $r \in [R, R+a]$.

5.3.1 Implementation of the Finite Fracture Mechanics approach

Particularizing to the axisymmetric case under study and $\Sigma_1 > 0$, the FFM formulation presents two scalar degrees of freedom: the remotely imposed tensile stress Σ_1, and the finite growth of the annular crack Δa. Eq. (5.5) shows that the governing pre-cracked stress component σ_{zz} monotonically decreases with r, whereas Eqs. (5.6) to (5.9) reveal that the annular crack Stress Intensity Factor K_I monotonically increases with a. All of this combined entails a huge simplification of the FFM formulation, since it means that the solution of the conditioned minimization problem always lies at the intersection of the stress and energy admissibility frontiers, i.e. where both conditions are strict equalities. As a result, the FFM approach here particularizes

into a system of two equations with two unknowns: the remote stress at failure Σ_{1f} and the critical finite crack length Δa_f.

For the FFM-orig formulation, the monotonically decreasing stress field allows only enforcing $\sigma_{zz}|_{z=0}$ to be equal to σ_C at $r = R + \Delta a$. Recalling Irwin's relation on the other hand, the energy condition can be written in terms of K_I and the corresponding fracture toughness K_{IC}, both of them squared. The Hausdorff measure of the finite crack growth $\mathscr{H}^2(\Delta\Gamma)$ here represents the in-plane area of a circular corona with inner and outer radii equal to R and $R + \Delta a$, respectively. Hence, the particularization of the FFM-orig approach writes as:

$$\text{FFM}-\text{orig}: \begin{cases} \sigma_{zz}\big(R+\Delta a_f, \Sigma_{1f}\big)\big|_{z=0} = \sigma_C \\ \displaystyle\int_0^{\Delta a_f} 2\pi\,(R+a)\,K_I^2\big(a,\Sigma_{1f}\big)\,\mathrm{d}a = \pi\left(\Delta a_f^2 + 2R\Delta a_f\right)K_{IC}^2 \end{cases}. \tag{5.10}$$

Each of the equations above can be expressed with explicit dependence to the weakening ratio Σ_{1f}/σ_C and the critical finite crack advance Δa_f by performing some algebraic manipulations, which result in:

$$\text{FFM}-\text{orig}: \begin{cases} \dfrac{\Sigma_{1f}}{\sigma_C} = \dfrac{1}{S_{zz}\big(R+\Delta a_f\big)} \\ \dfrac{\Sigma_{1f}}{\sigma_C} = \sqrt{\dfrac{\left(\Delta a_f^2 + 2R\Delta a_f\right) l_{ch}}{2\pi\displaystyle\int_0^{\Delta a_f}\left(a^2+aR\right)F_{\Sigma_1}^2(a)\,\mathrm{d}a}} \end{cases}, \tag{5.11}$$

where $l_{ch} = (K_{IC}/\sigma_C)^2$ is the Irwin's length. For given values of ν, R and l_{ch}, the two unknowns Σ_{1f} and Δa_f can be easily determined by numerical solvers for non-linear systems of equations.

Likewise, the governing system of equations for the FFM-avg approach particularizes to the considered problem as follows:

$$\text{FFM}-\text{avg}: \begin{cases} \displaystyle\int_R^{R+\Delta a_f} 2\pi r\,\sigma_{zz}\big(r,\Sigma_{1f}\big)\big|_{z=0}\,\mathrm{d}r = \pi\left(\Delta a_f^2 + 2R\Delta a_f\right)\sigma_C \\ \displaystyle\int_0^{\Delta a_f} 2\pi\,(R+a)\,K_I^2\big(a,\Sigma_{1f}\big)\,\mathrm{d}a = \pi\left(\Delta a_f^2 + 2R\Delta a_f\right)K_{IC}^2 \end{cases}, \tag{5.12}$$

and after pertinent algebraic manipulations, the corresponding numerically-convenient formulation writes as:

$$\text{FFM}-\text{avg}: \begin{cases} \dfrac{\Sigma_{1f}}{\sigma_C} = \dfrac{\Delta a_f^2 + 2R\Delta a_f}{2\displaystyle\int_R^{R+\Delta a_f} r\, S_{zz}(r)\, \mathrm{d}r} \\ \dfrac{\Sigma_{1f}}{\sigma_C} = \sqrt{\dfrac{\left(\Delta a_f^2 + 2R\Delta a_f\right) l_{ch}}{2\pi\displaystyle\int_0^{\Delta a_f} \left(a^2 + aR\right) F_{\Sigma_1}^2(a)\, \mathrm{d}a}} \end{cases} . \tag{5.13}$$

The normalized failure size-effect predicted by both FFM variants is illustrated in Fig. 5.3a. So as to also show the problem's dependency with the Poisson's ratio, three widely different values are considered therein: the two limit cases of $\nu \approx 0.5$ and $\nu \approx -1$, plus the intermediate $\nu = 0.0$. For each of these, the maximum stress concentration factor $S_{zz}|_{\max}$ is equal to $7/4$, $27/14$ and $13/6$, respectively. Both FFM-orig and FFM-avg agree to predict that $\Sigma_{1f}/\sigma_C(R \to 0) = 1$ and $\Sigma_{1f}/\sigma_C(R \to \infty) = 1/S_{zz}|_{\max}$. For such cases, the extreme values of R degenerate the coupling of stress and energy conditions, and only the values of σ_{zz} at $r \to \infty$ and $r \to R$ govern failure, respectively. For intermediate values of R/l_{ch} instead, failure

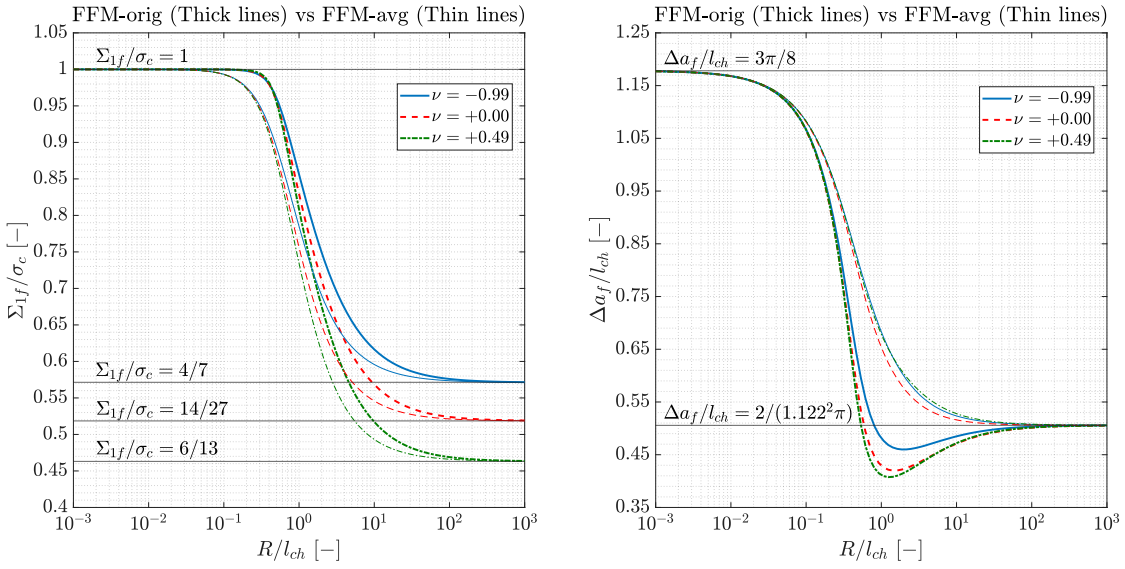

(a) (b)

Fig. 5.3 FFM predictions on the size-effect of: (a) the weakening ratio, and (b) the normalized critical finite crack growth.

is governed by the coupling of both stress and energy conditions, thus resulting in different yet comparable predictions. As expected, FFM-orig predicts higher failure loads than FFM-avg for a given pore radius.

The resultant predictions for the size-effect on the normalized critical finite crack size $\Delta a_f/l_{ch}$ are given in Fig. 5.3b for the same three values of ν. Once again, both FFM variants yield the same predictions for extreme void sizes: $\Delta a_f/l_{ch}(R\to 0) = 3\pi/8$ and $\Delta a_f/l_{ch}(R\to\infty) = 2/(1.122^2\pi)$. These two $\Delta a_f/l_{ch}$ values in turn correspond to those of a vanishing edge crack [40] and an immensely large Penny-shaped crack [77], respectively. Besides, the dependency of Δa_f on ν for a given FFM variant is proven to be minimal whereas it is noticeable between different approaches, the trend with R being non-monotonic (monotonic) for FFM-orig (FFM-avg).

5.3.2 Implementation of Dugdale's Cohesive Zone Model and results comparison

In line with what was done in Subsection 2.4.3, failure predictions by the CZM are used for benchmarking those by the FFM approaches. Approximated expressions for the Stress Intensity Functions corresponding to the auxiliary CSL and LLE loading cases[2] were proposed in [79]. Provided that the present geometry is somewhat the axisymmetric counterpart to that studied in Section 2.4, the limit cases now correspond to an edge crack when $R >> a$ and a Penny-shaped crack when $R << a$. For the CSL loading scenario, the proposed expression for $K_I^{\sigma_C}$ reads:

$$K_I^{\sigma_C}(a,\sigma_C) = \sigma_C\sqrt{\pi a}\,F_{\sigma_C}(a)\,, \tag{5.14}$$

$$F_{\sigma_C}(a) = 1.122\left(\frac{R}{R+2a}\right)^2 + \frac{2}{\pi}\sqrt{\frac{a+2R}{a+R}}\left[1-\left(\frac{R}{R+2a}\right)^2\right]. \tag{5.15}$$

For the LLE loading case instead, the approximated expression for $K_I^{\bar{P}}$ is:

$$K_I^{\bar{P}}(a,\bar{P}) = \frac{\bar{P}}{\sqrt{\pi a}}F_{\bar{P}}(a)\,, \tag{5.16}$$

[2] As introduced in Subsection 2.4.3, CSL and LLE stand for Constant Stress Lip and Line Load Edge loadings, respectively; these two were illustrated in Fig. 2.9 for the analogous case of a 2D circular hole.

$$F_{\bar{P}}(a) = 2.594\left(\frac{R}{R+5a}\right)^2 + \frac{2R}{\sqrt{(a+R)(a+2R)}}\left[1-\left(\frac{R}{R+5a}\right)^2\right]. \tag{5.17}$$

When using the Paris' integral [78], it must be considered that $\bar{P}$ is now applied all along the inner circumference of the annular crack on each lip, and so the resultant force applied per lip is $P = 2\pi R\bar{P}$. Using this relation and performing the pertinent algebraic manipulations, CZM's governing system of equations writes as:

$$\begin{cases} \dfrac{\Sigma_{1f}}{\sigma_C} = \dfrac{F_{\sigma_C}\left(a_{p,f}\right)}{F_{\Sigma_1}\left(a_{p,f}\right)} \\ \dfrac{\Sigma_{1f}}{\sigma_C} = \dfrac{R\,l_{ch} + 2\displaystyle\int_0^{a_{p,f}} (R+a)\,F_{\sigma_C}(a)\,F_{\bar{P}}(a)\,\mathrm{d}a}{2\displaystyle\int_0^{a_{p,f}} (R+a)\,F_{\Sigma_1}(a)\,F_{\bar{P}}(a)\,\mathrm{d}a} \end{cases}. \tag{5.18}$$

Then fixing $\nu = 0.2$, one obtains the normalized size-effect of failure reported in Fig. 5.4 for the FFM-orig, FFM-avg and CZM approaches. The results show that CZM provides even higher failure predictions than FFM-orig, which in turn is the FFM variant closest to CZM. Typically, cohesive laws featuring constant stress lead to failure predictions better in agreement to FFM-orig than to FFM-avg, whereas the opposite occurs for linear softening cohesive laws [77, 129].

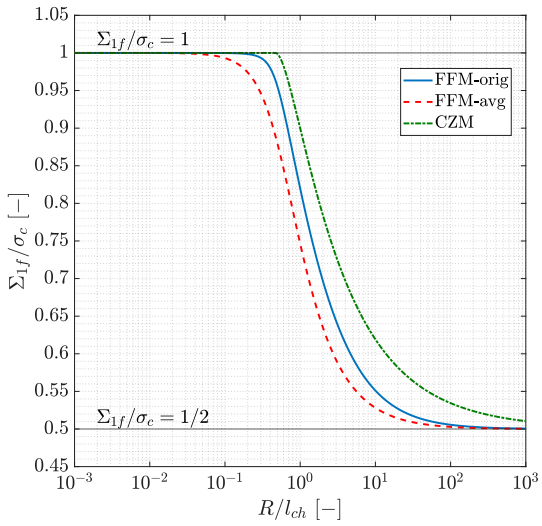

Fig. 5.4 Comparison between the size-effect on the weakening ratio as predicted by FFM and CZM.

5.3.3 Comparison with experiments and atomistic simulations

The effect of pore size and porosity in the ultimate strength of sodium borosilicate specimens under four-point bending was experimentally studied in [130]. To reduce the scatter due to the material's high brittleness, each specimen was sanded using grits with an overall average grain size equal to 17.25 μm. As a result, non-negligible superficial defects were introduced in the specimens, causing the showcased plain strength σ_C to actually be a structural property. On the other hand, no information on the material toughness K_{IC} was given. To estimate it, one can assume that the superficial defects in the specimens are edge cracks of length $a_0 = 17.25$ μm, thus yielding the structural Irwin's length $l_{ch} = 1.122^2 \pi a_0 = 68.22$ μm. Combining this with the reported plain strength $\sigma_C = 82.25$ MPa, the fracture toughness can be estimated as $K_{IC} = 0.68$ MPa$\sqrt{\text{m}}$ (see Table 5.1), which agrees with experimental measures in the literature [131]. The experimental results corresponding to the two lowest specimen porosities available in [130], namely 2% and 5%, are compared with the FFM failure predictions in Fig. 5.5a. In this figure, the pore size uncertainty arises from the experimental results being aggregated in ranges of R, whereas the 95% confidence interval is used to represent the failure load scatter within each pore size range. Such a comparison shows that FFM delivers predictions in reasonable agreement with experiments, especially for the 2% porosity, yet it generally overestimates the actual failure performance.

Table 5.1 Relevant magnitudes used for the comparison of FFM predictions with experimental results.

Reference	[130]	[132]	[133]
Material	Sodium borosilicate	Silicon nitride	$\beta-$silicon carbide
$\boldsymbol{\nu}$	0.20	0.28	0.20
$\boldsymbol{\sigma_C}$	82.25 MPa	735.0 MPa	58.0 GPa
$\boldsymbol{K_{IC}}$	0.68 MPa$\sqrt{\text{m}}$	6.0 MPa$\sqrt{\text{m}}$	1.69 MPa$\sqrt{\text{m}}$
$\boldsymbol{l_{ch}}$	68.23 μm	66.64 μm	8.48 Å
$\boldsymbol{R}$ **ranges**	$[5.0-186.0]$ μm	$[56.0-273.5]$ μm	$[1.17-19.96]$ Å

Another set of relevant experiments consisting in four-point bend tests performed on silicon nitride specimens containing a single spherical pore placed close to the tensile surface are reported in [132]. The given material properties are shown in Table 5.1, and the corresponding comparison with the FFM predictions is shown

in Fig. 5.5b. Once again, FFM shows reasonable agreement with the experimental results, although now these are mostly underestimated. Such a difference could be due to a non-null pore interaction in the previous set of experiments, for instance.

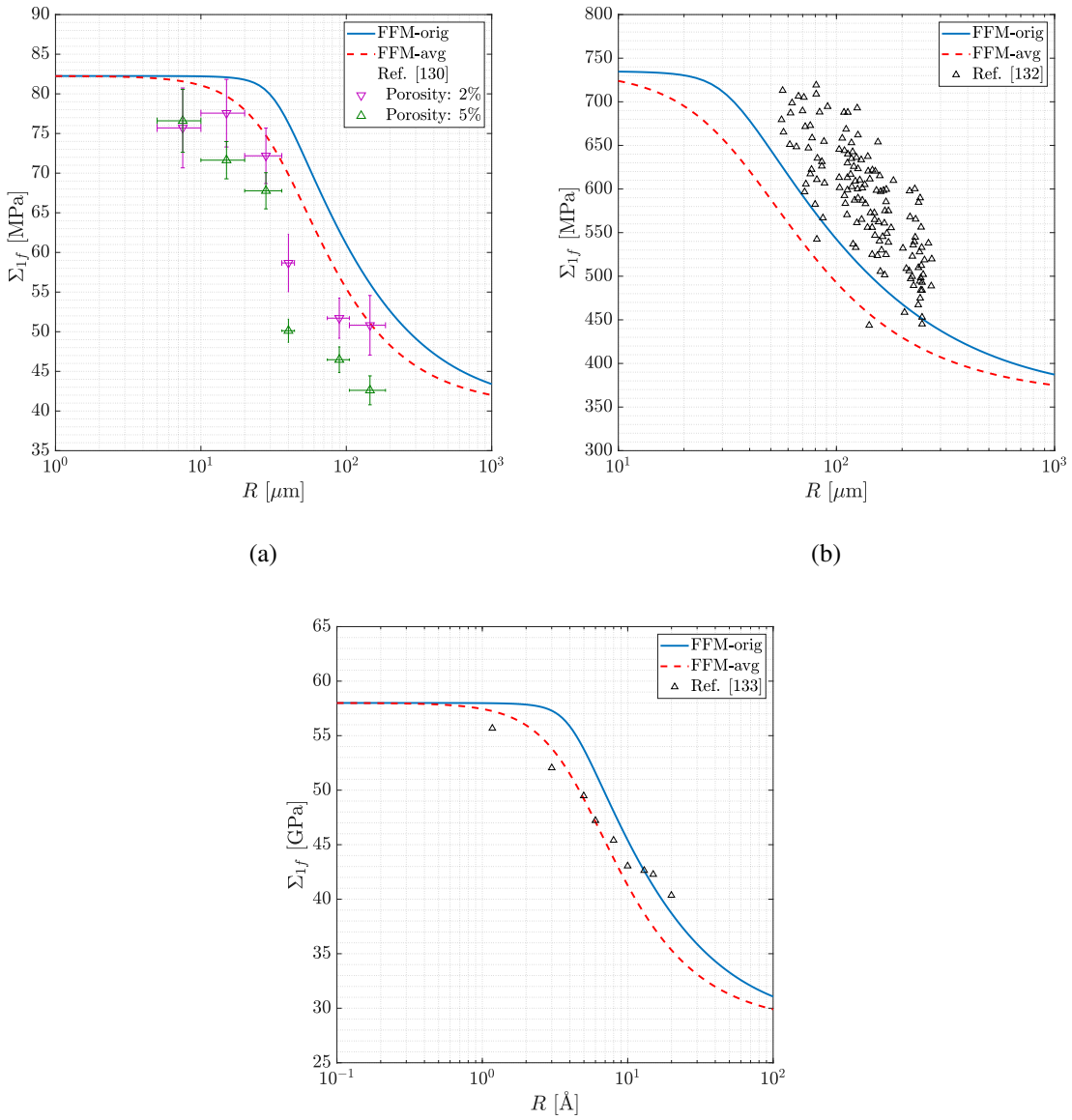

Fig. 5.5 Comparison of the FFM failure predictions with: experimental results from (a) [130] and (b) [132]; and (c) atomistic simulations from [133].

The presented set of experimental results infers that the FFM predicted size-effect of failure stemming from a spherical void is representative of the reality. Nonetheless, the material's high-brittleness combined with the presence of intrinsic defects, among other factors, disrupts the comparison of experimental results with the theoretical predictions. Towards providing a mean of validation devoid of empirical uncertainty, the failure results from atomistic simulations on a β-silicon carbide crystalline lattice that contains a "spherical" void [133] are reported in Fig. 5.5c alongside the FFM predictions. Clearly, at such scales the development of fracture is quantized to the interatomic length, which restricts the possible crack widths as opposed to a continuum setup. Still, the comparison with FFM failure predictions show adequate overall correlation. These results also show that FFM-avg is more accurate for small pore sizes, whereas FFM-orig performs best for larger voids. Remarkably, the properties reported in the reference, and not any fitting parameters, are used for such confront (see Table 5.1).

5.4 Case study on the crack onset from circular holes under biaxial loadings (II)

Let us now retake the (more intricate) case study already introduced in Section 2.4 and implement the FFM approach. As thoroughly described in Subsection 2.4.1, varying the loading biaxiality leads to a wide range of conditions for failure in terms of both the sign and trend distribution of $\sigma_{\theta\theta}$ and K_I (see Table 2.1). As a consequence, FFM's conditioned minimization problem can no longer be simplified into a system of two equations. This setup thereby allows for a much richer evaluation of the FFM framework.

Given that the geometry under study is bidimensional and its failure mechanism is well defined, the only degree of freedom pertaining to the crack is once again its length a (see Fig. 2.4). The biaxial loading is instead governed by the pair of values Σ_1' and β' defined in the surrogate loading space $(\Sigma_1' - \Sigma_2')$ (see Subsection 2.4.1). Taking the latter as an input parameter, Σ_1' and Δa remain as the two unknowns of the FFM approach when particularized to the case at hand. Specifically, FFM-orig states that the set $\mathrm{S_{orig}}$ for which failure stemming from the hole is admissible particularizes as:

$$\mathrm{S}_{\mathrm{orig}} = \left\{ \Sigma_1' \times \Delta a \in \mathbb{R}\times\mathbb{R} \;\middle|\; \begin{array}{l} \dfrac{\Sigma_1'}{\sigma_C} \geq \dfrac{1}{\min\limits_{r\in[R,R+\Delta a]} \left(S'_{\theta\theta}(r,0,\beta')\right)} \quad \text{and} \\ \dfrac{\Sigma_1'}{\sigma_C} \geq \sqrt{\dfrac{l_{ch}\,\Delta a}{\pi \displaystyle\int_0^{\Delta a} a\, F^2_{\beta'}(a,\beta')\,\mathrm{d}a}} \end{array} \right\}. \tag{5.19}$$

Nonetheless, the non-monotonic evolution of $S'_{\theta\theta}$ for $\beta' < 0$, combined with the minimum operator in the stress condition, causes FFM-orig to predict crack onset from very small holes at $\Sigma_{1f}/\sigma_C > 1$ in the baseline loading space $(\Sigma_1 - \Sigma_2)$. For such cases, the trivial hole-less failure solution $\Sigma_{1f}/\sigma_C = 1$ takes over according to FFM's minimization paradigm, and thus FFM-orig expects failure to onset infinitely away from the hole. For the sake of simplicity though, the exhaustive definition of $\mathrm{S}_{\mathrm{orig}}$ is omitted here, and the safety domains corresponding to the crack stemming from the hole are just truncated at $\Sigma_{1f}/\sigma_C = 1$.

On the other hand, FFM-avg yields the following particularization of the corresponding admissibility set:

$$\mathrm{S}_{\mathrm{avg}} = \left\{ \Sigma_1' \times \Delta a \in \mathbb{R}\times\mathbb{R} \;\middle|\; \begin{array}{l} \dfrac{\Sigma_1'}{\sigma_C} \geq \dfrac{\Delta a}{\displaystyle\int_R^{R+\Delta a} S'_{\theta\theta}(r,0,\beta')\,\mathrm{d}r} \quad \text{and} \\ \dfrac{\Sigma_1'}{\sigma_C} \geq \sqrt{\dfrac{l_{ch}\,\Delta a}{\pi \displaystyle\int_0^{\Delta a} a\, F^2_{\beta'}(a,\beta')\,\mathrm{d}a}} \end{array} \right\}, \tag{5.20}$$

which inherently considers the trivial hole-less solution due to the absence of the minimum operator in the stress condition.

The resulting biaxial safety domains are reported in Figs. 5.6, with the ratio R/l_{ch} as a parameter. Leveraging the low computational cost of the FFM approach, Figs. 5.6a and 5.6c illustrate the size-effect of failure through continuous contour plots. Their discretizations at fixed values of R are presented as contour lines in Figs. 5.6b and 5.6d. These figures demonstrate that FFM-orig and FFM-avg provide

comparable predictions for the safety domains: while these are mostly straight for the stress-dominated extreme configurations ($R \to 0$ and $R \to \infty$), they resemble arched curves for the intermediate cases in which the energy balance is relevant.

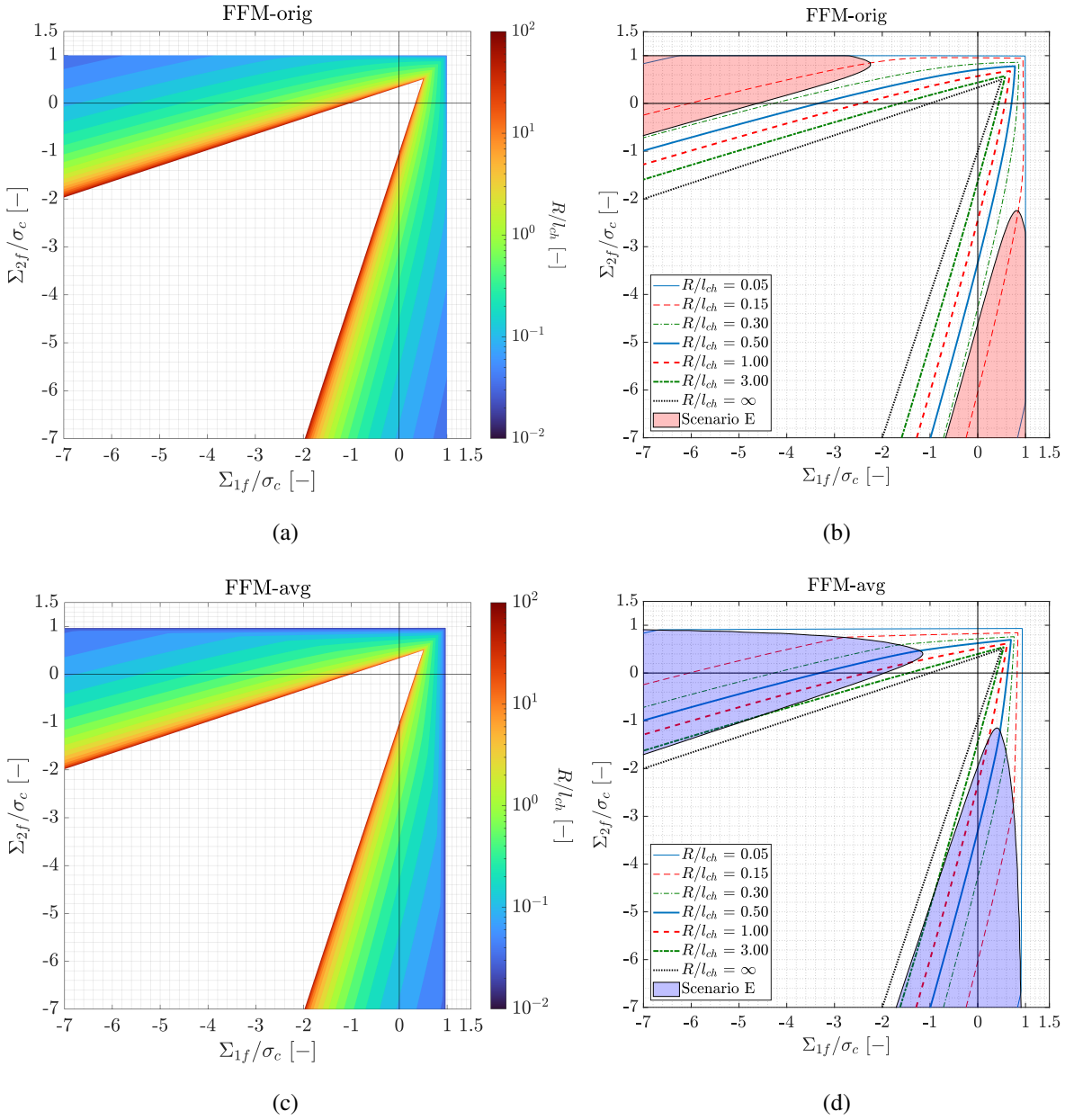

Fig. 5.6 R-dependent biaxial safety domains as predicted by: (a, b) FFM-orig, and (c, d) FFM-avg. Shaded regions indicate that failure onset is predicted to occur in Scenario E; elsewhere Scenario C takes place.

Both FFM approaches show a rather particular behaviour for $\beta' < -0.443$ due to the appearance of a local minimum in the energy condition frontier. In such cases, there exists a particular range of R for which the FFM failure predictions correspond to such a local minimum (Scenario E in Figs. 5.6b and 5.6d). This renders the stress condition irrelevant, and thereby the solutions are governed exclusively by the fracture toughness despite the geometry being non-singular. For values of R outside that particular range, FFM predictions are still governed by both conditions (Scenario C). Such a duality in the nature of FFM crack upon non monotonic frontiers of the energy conditions was also observed in [134] for interfacial cracks surrounding cylindrical inclusions.

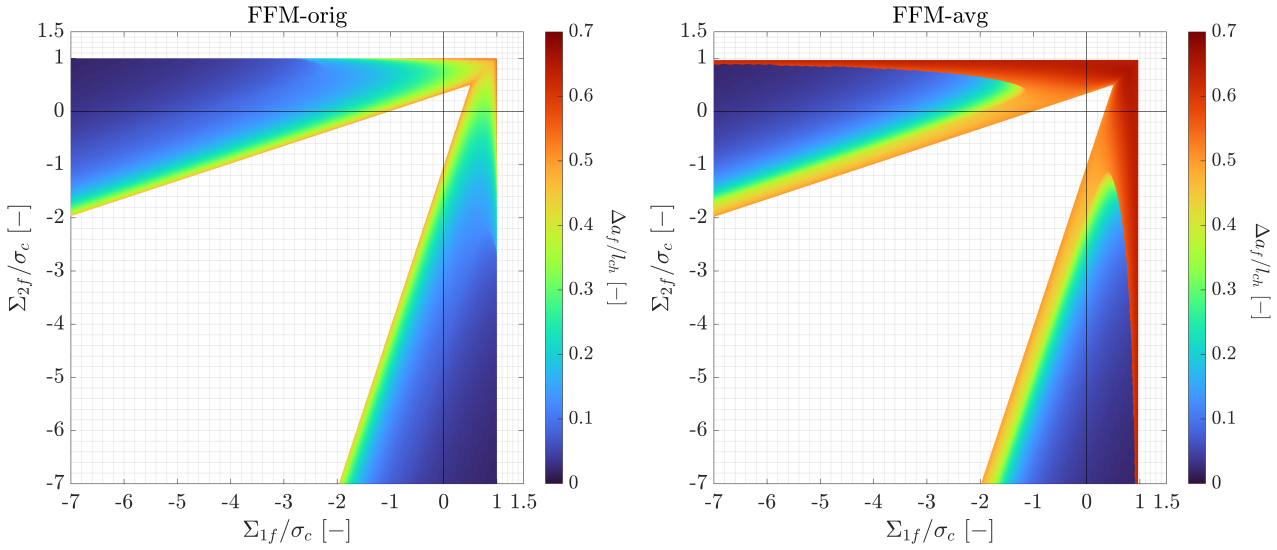

(a) (b)

Fig. 5.7 Evolution of Δa_f as predicted by: (a) FFM-orig, and (b) FFM-avg.

The predictions for Δa_f as the hole size and load biaxiality change are shown in Figs. 5.7a and 5.7b for the FFM-orig and FFM-avg, respectively. Therein, the dependence with R is implicit, in the sense that one should first determine from Figs. 5.6 the failure state $(\Sigma_{1f}, \Sigma_{2f})$ for given R and β', to then individuate the value of Δa_f in Figs. 5.7 that corresponds to such failure state. The evolution of Δa_f is thereby proven to be rather complex within the failure domain. Regardless of the FFM variant considered, larger values of Δa_f are expected towards bi-traction loading conditions or larger hole sizes. On the other hand, Δa_f decreases as the loading becomes more compressive, especially when failure initiation occurs in

Scenario E. The transition between crack onset scenarios also imprints the evolution of Δa_f, which manifests as a discontinuity for smaller holes and as a continuous kink otherwise. A detailed graphical explanation to this difference is given in Figs. 5.8, in addition to representing the complex interplay between the averaged stress and the energy conditions frontiers.

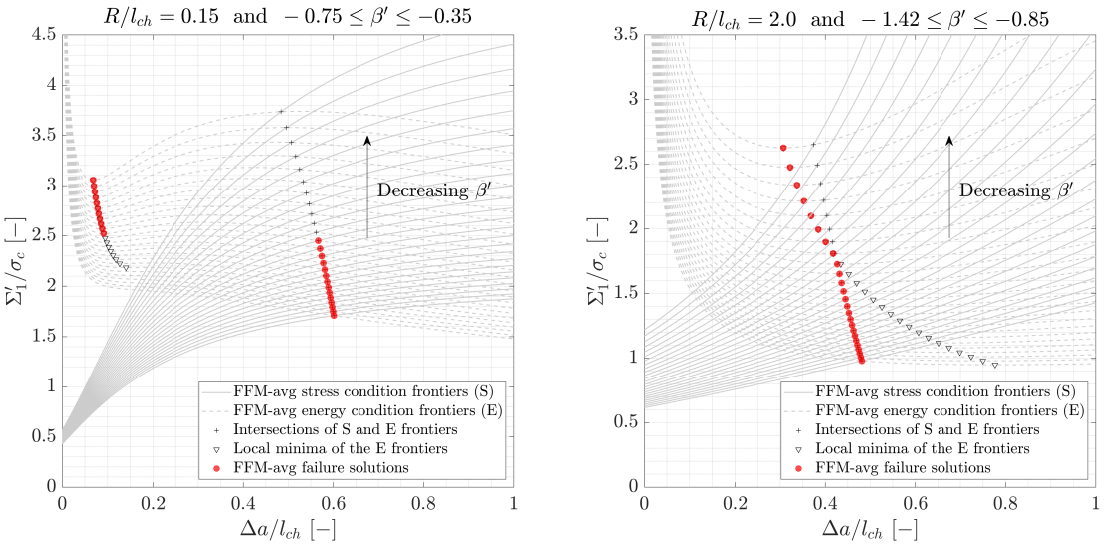

(a) (b)

Fig. 5.8 Details on the evolution of the FFM-avg stress and energy condition frontiers in the surroundings of the transition between Scenario C and E for: (a) small and (b) large holes.

5.4.1 Comparison with Dugdale's Cohesive Zone Model

The biaxial safety domains predicted by the two FFM variants are benchmarked against those by the CZM in Figs. 5.9. Comparisons once again show that FFM-orig is in better overall agreement with CZM than the averaged-stress counterpart. The effect of hole size and loading biaxiality in the FFM versus CZM correlation is also evident: discrepancies are higher for smaller holes and for bi-traction loading conditions. Detailed analyses show that FFM-orig and CZM are closer the more intense the normalized maximum crack opening stress component $\hat{\sigma}_{\theta\theta}$ becomes at the instant of failure (see Eq. (5.21) and Fig. 5.10). These findings are coherent with the closeness between FFM-orig and CZM predictions reported in [77] for crack onset from Penny-shaped cracks ($\hat{\sigma}_{\theta\theta} \to \infty$), and with the relative dissension reported in

Section 5.3 ($\hat{\sigma}_{\theta\theta} \sim 2$). Likewise, given the good agreement showcased in Subsection 2.4.3 between CZM and the PFM when using the No-Tension energy decomposition and the AT1 model, these results indirectly infer that the crack onset predictions by FFM-orig are also in fair agreement with those of the PFM/No-Tension/AT1.

$$\hat{\sigma}_{\theta\theta} = \frac{\sigma_{\theta\theta}(R, 0, \Sigma'_{1f}, \beta')}{\sigma_c} = \frac{\Sigma'_{1f}}{\sigma_c}\sqrt{2}\left(\beta' + 2\right) \tag{5.21}$$

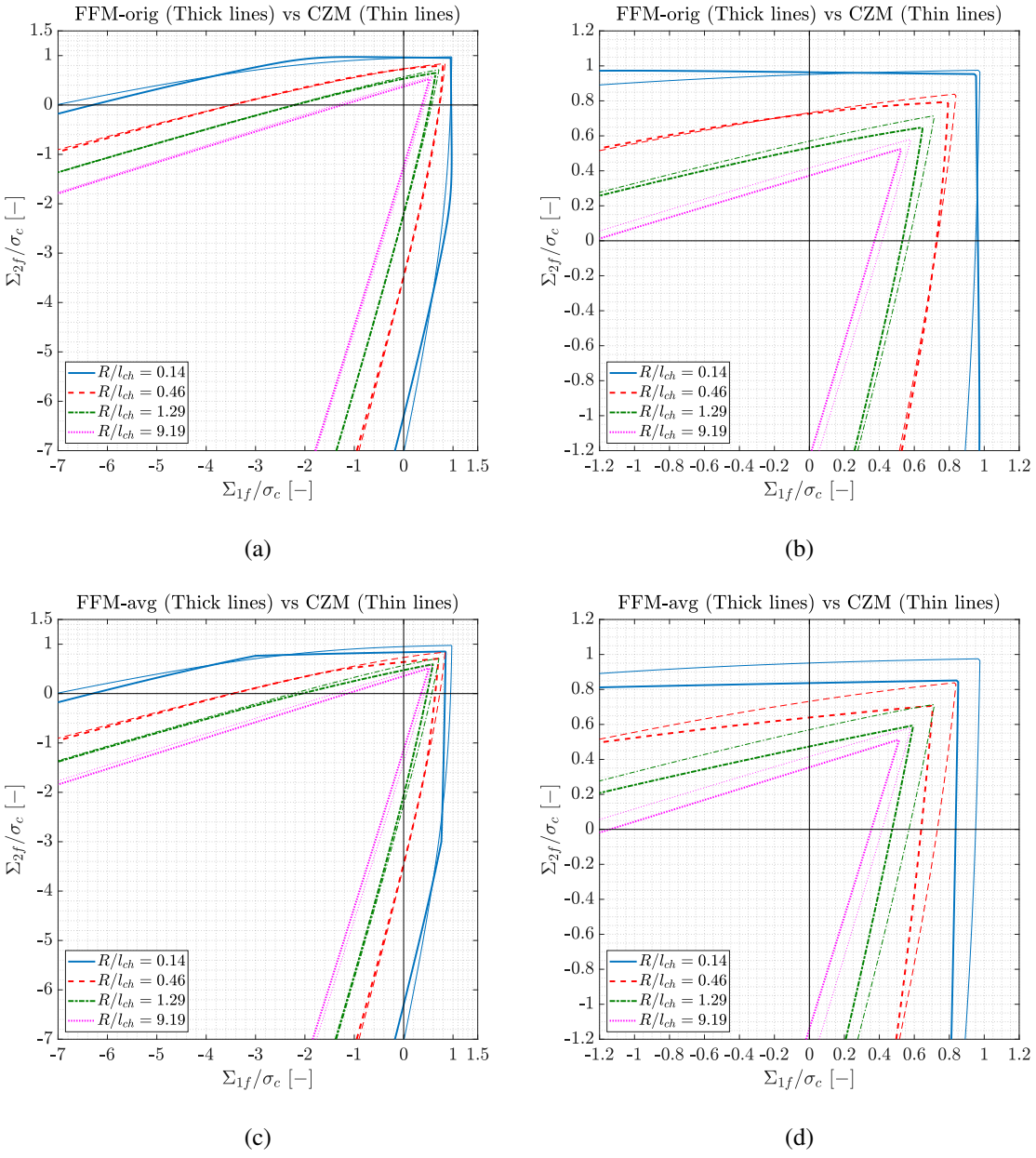

Fig. 5.9 Comparison of the safety domains predicted by CZM with those by: (a, b) FFM-orig, and (c, d) FFM-avg.

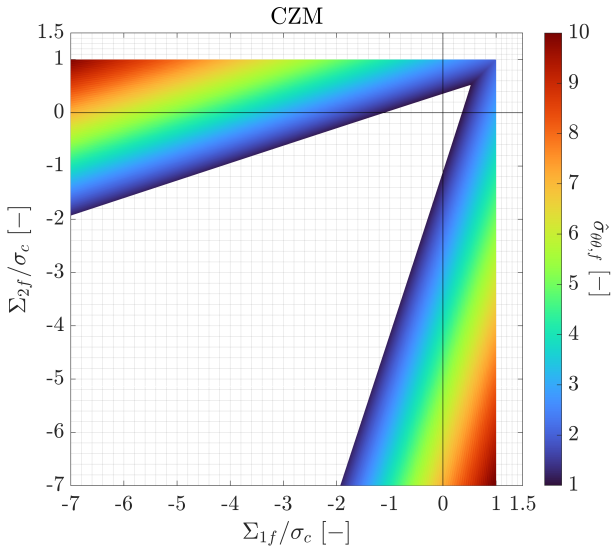

Fig. 5.10 Evolution of $\hat{\sigma}_{\theta\theta}$ along the failure domain according to CZM.

5.5 Conclusions

The Finite Fracture Mechanics framework for predicting quasi-static crack nucleation has been thoroughly presented in this chapter. To that end, the generalized principle of the criterion was first presented and then particularized to each of the two main variants, namely those proposed in [39] and in [40]. The approach was then implemented for predicting the crack onset from a spherical void embedded in an infinite domain subjected to uniaxial remote tension. The simplicity in the evolution of the pre-cracked stress field and the energy release upon fracture rendered this case study a nice demonstrator of the approach predictive capabilities. Therein, good agreement was obtained with respect to Dugdale's Cohesive Zone Model and relevant results from experimental test and atomistic simulations. The application to the much more intricate case of the crack onset from a circular hole under biaxial loading was also here undertaken, and its complexity allowed evidencing some of the approach peculiarities. It is worth to be noted the prediction of a purely-energy-driven crack onset for some loading cases despite the geometry not being singular. Once again, Dugdale's Cohesive Zone Model was used as a vector of validation, against which Finite Fracture Mechanics shows reasonable agreement for

the whole failure domain. Once familiarized with the intricacies and capabilities of the Finite Fracture Mechanics approach for predicting crack onset under quasi-static loading conditions, the foundations for undertaking its extension to dynamic loading conditions are set.

Chapter 6

Dynamic Finite Fracture Mechanics[1]

6.1 Introduction

Despite the extensive development that the Finite Fracture Mechanics approach has undergone in the last years, most of it is confined to purely quasi-static conditions. Indeed, only a few recent exploratory studies have ventured to consider dynamic effects within the Finite Fracture Mechanics framework [135, 136]. Nonetheless, these were mostly focused on the localized dynamic effects arising from the crack nucleation and propagation themselves rather than from the loading.

With regard to the prediction of failure under dynamic loadings, many criteria have been proposed in the literature as dynamic extensions of well-established quasi-static approaches. For instance, the "Classical dynamics approach" (see [137]) posits that the strength and toughness are material rate-dependent functions. These properties are thereby obtained from coupon testing first and then extrapolated to more complex failure scenarios. For plain geometries, failure is assessed analogously to the quasi-static Maximum Stress criterion; for singular geometries instead, akin to the Linear Elastic Fracture Mechanics approach. This allows for a simple yet limited dynamic failure criterion whose numerical implementation is straightforward. A well-known framework falling within this category would be the dynamic component of the Johnson-Cook model for elastoplastic materials [42].

[1] Part of the work described has been previously published in: Chao Correas, A., Cornetti, P., Corrado, M., Sapora, A. (2023). Finite Fracture Mechanics extension to dynamic loading scenarios. *Int J Fract* 239, 149–165.

A slightly more developed stress-based criterion was introduced in [44] as a dynamic reformulation of the Theory of Critical Distances [38]. Through non-local assessment of the stress condition for failure, different limitations of the classical approaches to fracture are sorted out while keeping the approach simple. Its increased versatility allows its implementation to different notched specimens, and comparisons with dynamic experimental results revealed errors in the $\pm 20\%$ range [44, 138]. Still, the use of a material length for the non-local condition precludes its application to small specimens. Likewise, its instantaneous assessment, combined with the use of material functions for the rate-dependency of strength, renders it an eminently empirical criterion.

On the contrary, Petrov and Morozov [43] approached dynamic failure by quantizing both the spatial and temporal nature of the dynamic problem. They proposed that the observed rate dependence of the strength and toughness is only apparent and stems from the temporal inhomogeneity of the stress field. According to this rationale, the dynamic strengthening/toughening represents the temporal counterpart of the failure size-effect observed upon stress concentrations. This allows to consider that the quasi-static measures for the strength and toughness still hold in the dynamic failure regime, their apparent changes being captured instead through the non-instantaneous assessment of a stress condition. In particular, they proposed a modified version of the Neuber-Novozhilov criterion [35, 36] that requires the quasi-static stress and toughness, plus a characteristic time period. This latter property, therein called "incubation time", encapsulates the rate-dependence of the material and gives name to the approach: Incubation Time failure criterion [139]. As such, the dynamic material characterization results considerably less dependent on the post-processing of experimental data. Besides, it proves capable to capture particular phenomena observed in dynamic experiments, such as the post-peak-load failure onset under short pulse loadings [140]. Reasonable accuracy against dynamic experimental results was also observed for crack onset in pre-cracked geometries [43, 141], or for spalling failure [137]. On the downside, the use of a fixed length for the non-local assessment entrains the limited applicability to small specimens.

Following the paradigm of finite spatio-temporal approaches, an energy-based dynamic failure criterion was introduced in [142] under the name of Dynamic Quantized Fracture Mechanics. Therein, the condition for failure is expressed in terms of the dynamic energy released by a finite crack growth integrated along a fixed time period preceding each instant. The criterion thereby results non-instantaneous

and non-local like the Incubation Time failure criterion, and they were even reported to yield similar predictions for the dynamic failure of notched metallic specimens. Nonetheless, its particular energy-based definition proposed leads to a difficult and not-so-robust implementation.

In this context, the versatile Finite Fracture Mechanics approach is believed to have the potential for significantly contributing to the prediction of dynamic failure onset. Thereof, the present chapter presents an extension of the framework to dynamic loadings. In awe of fairness though, this proposal should not be understood as a definitive answer to the modelling of dynamic failure, but as the establishment of a preliminary line of thought that showcases reasonable accuracy against a limited set of experiments. Additional empirical data would thus be required in order to provide a more robust and better understood approach, although the complexity of dynamic testing makes it a challenging endeavour.

6.2 Requisites of a proper dynamic failure criterion

Let us bring back the generic failure onset problem defined in Fig. 5.1, but now assuming that the loading is no longer quasi-static but dynamic. As such, the prescribed displacements and forces along the Dirichlet and Neumann boundaries are $\underline{U}_t$ and $\underline{f}_t$, respectively. Prior to fracture nucleation, the domain Ω undergoes dynamic stressing per $\underline{\underline{\sigma}}_t(\underline{x})$. In the event of an infinitesimal crack growth per $\delta\Gamma$, the energy stored in Ω gets released at a rate $G_{\text{dyn},t}(\delta\Gamma)$. Noteworthy, the latter incorporates variations in potential and kinetic energy due to crack growth [143], hence the "dyn" subindex.

Under these circumstances, one can apply a stress and/or energy-based dynamic failure criterion to predict the instant t_f at which fracture nucleates. However, the representativeness of the resultant prediction is conditioned to the compliance with certain requirements. For instance, given that quasi-static loadings are a particular dynamic case in which $\dot{\underline{f}}_t \to 0$ and $\dot{\underline{U}}_t \to 0$, any proper dynamic failure criterion is ought to be also applicable to quasi-static loadings. Thereof, this mostly obvious first requisite also implies that all the discussions from the literature that regard the representativeness of quasi-static failure criteria also apply to those dynamic, e.g. the necessity of non-local criteria.

The law of conservation of momentum imposes a second requirement to dynamic failure criteria: these cannot be assessed instantaneously and should account for impulses. To illustrate this concept, let us assume the scenario in Fig. 6.1. Therein, the massive domain Ω is composed of two rigid subdomains Ω_1 and Ω_2, in contact through a generic interface $\partial_I\Omega$ that cannot transmit tensile forces. Furthermore, Ω_1 is fixed, whereas Ω_2 is subjected to the distributed dynamic force f_t. This case represents a degenerated tensile failure scenario in which both the material strength and specific fracture energy are null for $\delta\Gamma \in \partial_I\Omega$, and infinite otherwise. Therefore, Ω can be supposed to "fail" once Ω_1 and Ω_2 cease to be in contact along $\partial_I\Omega$. Eventually, this can only happen if a non-null impulse is absorbed by Ω_2, which allows it to change its linear momentum and separate from Ω_1. This condition cannot be captured by instantaneous failure criteria since they do not ensure the conservation of momentum [137].

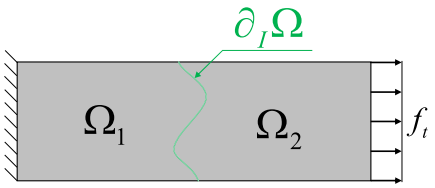

Fig. 6.1 Schematic representation of the domain used for proving that impulses should be accounted for in a robust dynamic failure criterion.

Remarkably, the necessity of non-instantaneous dynamic failure criteria somewhat entails symmetry between the temporal and spatial aspects of the problem: whenever the stress field varies in time (space), failure criteria should be non-instantaneous (non-local) in order to be robust. This spatio-temporal analogy of fracture was already reckoned in [137]. Furthermore, the necessity of non-instantaneous failure criteria is experimentally supported by the findings in [140], wherein failure was observed to nucleate after the peak stress upon short pulse loadings.

Finally, when passing from quasi-static to dynamic loadings one should reinterpret how to predict failure based on the fulfilment of certain conditions. In a quasi-static mindset, failure criteria predict crack nucleation at the minimum load level for which certain conditions are met. Nonetheless, per the irreversibility of fracture and the one-way time flow, this is only acceptable under monotonically increasing loadings. Therefore, in the more generic dynamic case, failure should be

instead assumed to take place at the earliest instant for which the failure conditions are met.

All in all, the necessary (but non sufficient) conditions for a dynamic failure criterion to be robust are:

1. Straightforward applicability to quasi-static scenarios.
2. Non-instantaneous definition that accounts for impulses.
3. Minimization of the time to failure subjected to certain conditions.

6.3 State of the art for dynamic failure criteria

The prediction of failure under dynamic loadings has already been tackled through different approaches in the literature. Upon such conditions, the domain Ω is in dynamic equilibrium of forces, its deformation diffusing through mechanical waves. This feature renders the dynamic cases severely more complex than those quasi-static, generally precluding to have self-similar states scaled by one single intensity parameter akin to Σ in Chapter 5. As a consequence, in what follows let us simplify the dynamic crack onset problem by further assuming that: (i) the Dirichlet boundary conditions are homogeneous, i.e. $\underline{U}_t = \underline{0}$; (ii) the loading comes from a single dynamic Neumann boundary condition $\underline{f}_t \propto \Sigma_t$ applied along $\partial_f\Omega$; and (iii) the prescribed force follows $\underline{f}_{t\leq 0} = \underline{0}$ and $\underline{f}_{t>0} \neq \underline{0}$.

The most simplistic dynamic failure criterion represents the direct extrapolation to dynamic loadings of either the Maximum Stress failure criterion for plain geometries, or the Linear Elastic Fracture Mechanics framework for singular ones. Commonly known as the "Classical dynamics approach" (see e.g. [137]), the condition for failure is locally and instantaneously assessed by comparing relevant measures of the stress field or the stress intensity factors against rate-dependent measures of the strength or toughness as in Eq. (6.1). Moreover, the functions defining these dynamic thresholds are assumed to only depend on the material, and thus can be determined from dynamic coupon testing.

$$\left\{\sigma_{t_f}, K_{It_f}\right\} = \left\{\sigma_C\left(\dot{\Sigma}\right), K_{IC}\left(\dot{\Sigma}\right)\right\} \tag{6.1}$$

Therefore, the application of the "Classical dynamics approach" first requires to determine whether the domain presents a stress singularity, and so its implementation is not consistent for every geometry and loading. Likewise, its definition is local and instantaneous, and the rate-dependent ultimate properties are merely empirical.

The issues arising from a local assessment of the classical dynamic criterion were partially remedied by the Dynamic reformulation of the Theory of Critical Distances (DTCD) [44, 138]. Mimicking the quasi-static criterion [38], a non-local measure of the dynamic stress was instantaneously put against the empirical rate-dependent strength. For instance, in the case of the Line Method for a 2D problem, the DTCD failure criterion writes as:

$$\frac{1}{L\left(\dot{\Sigma}\right)}\int_0^{L\left(\dot{\Sigma}\right)}\sigma_{t_f}(r)\,\mathrm{d}r=\sigma_C\left(\dot{\Sigma}\right)\,, \tag{6.2}$$

where r is a radial coordinate stemming from the critical stress-raiser, and $L\left(\dot{\Sigma}\right)$ is a material and rate-dependent length defined as:

$$L\left(\dot{\Sigma}\right)=\frac{2}{\pi}\left[\frac{K_{IC}\left(\dot{\Sigma}\right)}{\sigma_C\left(\dot{\Sigma}\right)}\right]^2\,. \tag{6.3}$$

The non-local stress condition allows the DTCD to be applied irrespectively to plain or singular geometries, as well as to capture the size effect of failure. On the other hand, its assessment is still instantaneous and it relies on empirical functions for the rate-dependent strength and toughness. Moreover, the used critical length L only depends on the material and the loading, and so the DTCD criterion cannot be applied to specimens that are too small (see e.g. [40]).

A completely different paradigm was proposed by Petrov and Morozov [43] with the Incubation Time (IT) failure criterion. Taking the Neuber-Novozhilov [35, 36] condition as a basis, the IT approach posits that failure in a 2D domain takes place when:

$$\frac{1}{\tau}\int_{t_f-\tau}^{t_f}\frac{1}{d}\int_0^{d}\sigma_t(r)\,\mathrm{d}r\,\mathrm{d}t=\sigma_C\,, \tag{6.4}$$

where τ is the so-called Incubation Time, an additional material property that governs the dynamic dependence of failure. Likewise, r plays the same role as in the

DTCD, and d is a fixed material length defined as:

$$d = \frac{2}{\pi}\left(\frac{K_{IC}}{\sigma_C}\right)^2 . \tag{6.5}$$

Therefore, the IT criterion hypothesizes that the dynamic dependence of failure stems from the temporal inhomogeneity of the stress field, just as its size-effect arises from the presence of stress concentrations. Besides, the dynamic material characterization is reasonably simple for it only comprises the quasi-static strength σ_C and toughness K_{IC}, plus the incubation time τ. This advantage adds up to the non-local and non-instantaneous definition of the criterion, which is also accounting for impulses. Indeed, this is a quite robust approach whose main limitation is its reliance on a constant characteristic length d.

Although many stress-based dynamic failure criteria have been proposed, those energy-based are much more scarce. One of the few proposals in this sense is the Dynamic Quantized Fracture Mechanics (DQFM) [142], whose failure condition in a 2D setup is defined as:

$$\frac{1}{\Delta t}\int_{t_f-\Delta t}^{t_f}\frac{1}{\Delta a}\int_0^{\Delta a} G_{\mathrm{dyn},t}(a)\,\mathrm{d}a\,\mathrm{d}t = G_C\,. \tag{6.6}$$

where a represents the crack length, and Δa and Δt are regarded as crack advance and time quanta, respectively. The similarities between Eqs. (6.4) and (6.6) are evident. Nonetheless, the latter presents limited physical soundness since it averages the energy released upon a crack growing by Δa at each instant $t \in \left[t_f - \Delta t, t_f\right]$, which is not a good estimation of the actual energy released during the prolonged-in-time and cumulative process of finite crack growth. What is more, the resultant mathematical formulation was found to not be robust for certain cases. Besides these drawbacks, both the IT and the DQFM criteria agree in several aspects, such as the spatio-temporal quantification through constant parameters ($d-\tau$ and $\Delta a - \Delta t$) or the assumption that the quasi-static ultimate properties still apply to dynamic fracture onsets.

6.4 Dynamic Finite Fracture Mechanics approach

Per the previous sections, the most promising dynamic failure criterion of those available is the IT [43], yet the use of a fixed assessment length $d \propto (K_{IC}/\sigma_C)^2$ limits its applicability. For quasi-static setups, the FFM approach [39, 40] solved this very same issue of the TCD [38] and QFM [37] criteria by coupling the non-local stress and energy conditions for failure. Hereafter, such a rationale is exploited in order to propose an extension of the FFM framework to dynamic loading conditions (DFFM). As above mentioned though, dynamic loading conditions render structural problems noticeably more complex. This mostly precludes meticulous modelling of the actual dynamic fracturing event through semi-analytical approaches akin to the FFM. Thereof, the following DFFM proposal is aimed at presenting a line of thought upon which to establish a convenient and reasonably accurate tool for preliminarily predicting dynamic failure without actually modelling it in detail.

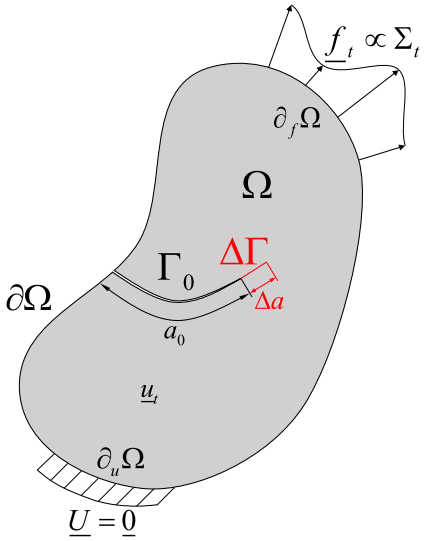

Fig. 6.2 Schematic representation of the generic 2D setup used for the DFFM proposal.

Aiming for a concise proposal, only the FFM-avg variant [40] is here considered for its dynamic extension. Likewise, the generic fracture onset problem from Fig. 5.1 is now restricted to only the 2D case depicted in Fig. 6.2. The prospective crack path is assumed known and parametrized by the arc-length a, a_0 and Δa being the pre-existing crack length and the finite growth, respectively. Besides, the loading is exerted through prescribed forces whose magnitude is proportional to the temporal function Σ_t. Then, under the assumption that there exist the functions $\boldsymbol{\sigma}(\underline{x}, \Sigma_t)$ and

$G_{\mathrm{dyn}}(a, \Sigma_t)$, the proposed DFFM posits failure to be admissible only within the set $\mathrm{S}_{\mathrm{avg}}^{\mathrm{dyn}}$ defined as:

$$\mathrm{S}_{\mathrm{avg}}^{\mathrm{dyn}} = \left\{ t \times \Delta\Gamma \in \mathbb{R}\times\mathbb{R} \;\middle|\; \begin{array}{c} \displaystyle\int_{\Delta\Gamma} \boldsymbol{\sigma}\left(\underline{x}, \langle\Sigma\rangle_{t-\tau}^{t}\right) \mathrm{d}\underline{x} \geq \int_{\Delta\Gamma} \boldsymbol{\sigma}_c \, \mathrm{d}\underline{x} \qquad \text{and} \\ \displaystyle\int_{\Gamma}^{\Gamma+\Delta\Gamma} G_{\mathrm{dyn}}\left(a, \langle\Sigma\rangle_{t-\tau}^{t}\right) \mathrm{d}a \geq \int_{\Gamma}^{\Gamma+\Delta\Gamma} G_C \, \mathrm{d}a \end{array} \right\}, \tag{6.7}$$

where:

$$\langle\Sigma\rangle_{t-\tau}^{t} = \frac{1}{\tau} \int_{t-\tau}^{t} \Sigma_{t'} \, \mathrm{d}t' \,. \tag{6.8}$$

The instant of failure t_f and critical crack growth $\Delta\Gamma_f$ are eventually determined through the following conditioned minimization problem:

$$\left(t_f, \Delta\Gamma_f\right) = \underset{(t,\Delta\Gamma)\in \mathrm{S}_{\mathrm{avg}}^{\mathrm{dyn}}}{\arg\min} \; (t) \,. \tag{6.9}$$

Clearly, the DFFM proposal above relies on the strong assumption that $\boldsymbol{\sigma}(\underline{x}, \Sigma_t)$ and $G_{\mathrm{dyn}}(a, \Sigma_t)$ exist. This implies that the temporal dependence of $\boldsymbol{\sigma}_t$ and $G_{\mathrm{dyn},t}$ exactly follows that of Σ_t, and so these magnitudes can be defined with no explicit dependence on t; however, such a hypothesis is only reasonably true under certain conditions (see Section 6.5). On the upside, all three aforementioned requisites for dynamic criteria are fulfilled. For instance, it is evident from Eq. (6.9) that failure onset is acknowledged at the first admissible instant. Likewise, in the quasi-static limit $\dot{\Sigma} \to 0$, $\mathrm{S}_{\mathrm{avg}}^{\mathrm{dyn}}$ can be turned into $\mathrm{S}_{\mathrm{avg}}$ in Eq. (6.10), which is nothing but the particularization to the case at hand of the failure admissibility set per the well-established FFM-avg approach.

$$\mathrm{S}_{\mathrm{avg}} = \left\{ \Sigma \times \Delta\Gamma \in \mathbb{R}\times\mathbb{R} \;\middle|\; \begin{array}{c} \displaystyle\int_{\Delta\Gamma} \boldsymbol{\sigma}(\underline{x}, \Sigma) \, \mathrm{d}\underline{x} \geq \int_{\Delta\Gamma} \boldsymbol{\sigma}_c \, \mathrm{d}\underline{x} \qquad \text{and} \\ \displaystyle\int_{\Gamma}^{\Gamma+\Delta\Gamma} G(a, \Sigma) \, \mathrm{d}a \geq \int_{\Gamma}^{\Gamma+\Delta\Gamma} G_C \, \mathrm{d}a \end{array} \right\}. \tag{6.10}$$

Furthermore, Eq. (6.8) implies that the evaluation of the criterion is non instantaneous, for it spans along an interval of duration τ preceding each instant. Moreover, $\langle\Sigma\rangle_{t-\tau}^{t}$ can be regarded as a measure of a constant load that generates the same

impulse as Σ_t along the aforementioned time lapse. These considerations allow to establish a two-sided interpretation for τ: mathematically, it represents the time a constant load equal to that of quasi-static failure has to be applied for a crack to nucleate; phenomenologically, it can be seen as the minimum time required for the microcracks to coalesce into a single most-convenient macrocrack. Hence, τ will be hereafter referred to as "Coalescence period". Nonetheless, DFFM does not identify τ as a lower bound for the time to failure, but instead as the minimum value for t_f that allows dynamic fracture to develop as a single crack.

The proposed non-instantaneous energy condition can also be physically interpreted upon the assumption that finite crack onset takes place through the coalescence of microcracks along a finite time interval. This prolonged-in-time energy-releasing process thereby develops under varying-in-time conditions due to the dynamic loading. In order to handle this complex phenomenon in a reasonably simple way, the proposed DFFM determines an effective energy release equal to that if a constant load equal to $\langle\Sigma\rangle_{t-\tau}^{t}$ was applied throughout the coalescence process. As such, the simplified energy balance herein proposed differs conceptually from that introduced in [142], and it does not share the latter's limited physical representativeness.

According to Eqs. (6.7) and (6.10), should the loading magnitude at quasi-static failure be known, namely Σ_f, the corresponding dynamic failure admissibility set $\mathrm{S}_{\mathrm{avg}}^{\mathrm{dyn}}$ could be compactly written as:

$$\mathrm{S}_{\mathrm{avg}}^{\mathrm{dyn}} = \left\{ t \in \mathbb{R} \middle| \langle\Sigma\rangle_{t-\tau}^{t} \geq \Sigma_f \right\} . \tag{6.11}$$

thus meaning that DFFM essentially requires the applied dynamic force magnitude Σ_t to at least generate an impulse equalling $\Sigma_f \tau$ for the dynamic failure onset to occur. Likewise, the equation above implies that $\Delta\Gamma_f$ is rate-independent under the assumptions here made.

6.5 Implementation and experimental validation

The representativeness of the DFFM proposal is hereafter proven through comparison with results from relevant dynamic experiments available in the literature. Aiming for comprehensiveness, the chosen experimental campaigns include failure upon singular and non-singular stress concentrators, as well as upon constant stress distributions

[144–146]. All the considered tests were performed on Laurentian granite, which is a fine-grained rock that allows using reasonably small specimens while keeping the homogeneity assumption. Likewise, it has been reported to showcase linear elastic behaviour and quasi-brittle fracture [147, 148]. On the downside, it presents some variability in the mechanical properties per being a natural and multi-granular material, especially in the fracture toughness [149].

For the relevant experiments, the dynamic loading was reported to be exerted via a modified Split Hopkinson Pressure Bar system (SHPB), which used the pulse shaping technique to yield an almost constant loading rate [150]. This characteristic is often overlooked in dynamic testing despite being essential to ensure the representativeness of the results. Indeed, conventional SHPB systems generate square-like pulses whose loading rate $\dot{P}$ tends to infinity, thereby rendering the interpretation of dynamic test results a very delicate task. Instead, the loading rate is well defined when using the pulse shaping technique, and one can model the prescribed loading up to breakage as:

$$P_t = \begin{cases} 0 & \text{if } \ t < 0 \\ \dot{P}t & \text{if } \ t \geq 0 \end{cases} . \tag{6.12}$$

Furthermore, it was found that using the modified SHPB for coupon testing can actually lead to the specimens showcasing a quasi-equilibrium between the applied and reaction forces that diminish the inertial effects [150]. This allows for the two quasi-static expressions $\sigma(r, P)$ and $K_I(a, P)$ to still hold once the loading is dynamic as per P_t in Eq. (6.12) [151, 152]. On the other hand, the conventional Irwin's relation between K_{It} and $G_{\mathrm{dyn},t}$ still applies for dynamic conditions and stationary cracks [143]. As such, the existence of the functions $\sigma(r, P_t)$ and $G_{\mathrm{dyn}}(a, P_t)$ is ascertained for coupon tests performed with the modified SHPB system, thus enabling the implementation of the above proposed DFFM approach to predict failure onset.

Hereafter, the oncoming sections will particularize the DFFM approach to the two different setups used in the experiments: the Semi-Circular Bend (SCB) and the Brazilian Disk (BD) test depicted in Figs. 6.3. For the former, both notched (NSCB, $a_0 > 0$) and unnotched (USCB, $a_0 = 0$) specimens are considered. Thereafter, the comparison between the DFFM predictions and the dynamic experimental results is undertaken. It is noteworthy that these setups are commonly studied for rock specimens under quasi-static loadings [153–157].

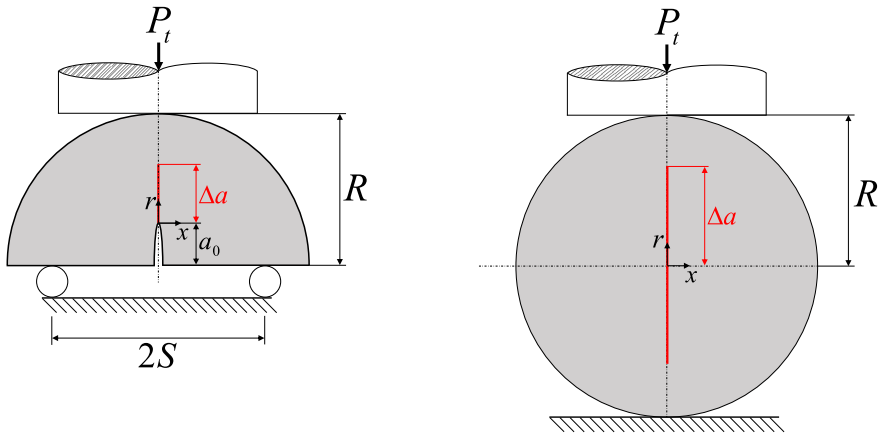

(a) (b)

Fig. 6.3 Geometrical definition of: (a) the SCB and (b) BD specimens.

6.5.1 Semi-Circular Bend test

The SCB test is among the most common procedures for testing rock materials under bending since the specimens can be directly obtained from drilled cores. As shown in Fig. 6.3a, four parameters define the geometry of each test, namely the specimen's radius R, thickness B and initial crack length a_0, in addition to the distance between the support rollers $2S$. On the other hand, the loading is applied through contact on the curved surface, and can be thus approximated by a concentrated force P_t.

Regardless of whether the SCB specimen under consideration is notched or not, the most failure-prone region corresponds to its midplane. For instance, in the case of a straight crack of length a stemming from the flat surface along this plane, K_I can be defined as:

$$K_I(a,P) = \frac{P}{BR}\sqrt{\pi a}\,F(a)\,, \tag{6.13}$$

where $F(a)$ represents a polynomial shape function derived from Finite Element analyses. Please notice that a in Eq. (6.13) encompasses the initial crack length a_0 plus any subsequent crack growth Δa when applied to the case in Fig. 6.3a.

Likewise, for an SCB specimen with an initial crack of length a_0, the crack opening stress component along the specimen's midplane σ_{xx} can be approximated by:

$$\sigma_{xx}(r,P) = \frac{P}{BR}\left[\sqrt{\frac{a_0}{2r}}F(a_0) + s_{xx}(r)\right] = \frac{P}{BR}S_{xx}(r)\,, \tag{6.14}$$

where the term $\sqrt{a_0/2r}F(a_0)$ captures the asymptotic stress field in the surroundings of the crack tip in the case of $a_0 > 0$. The stress field far from the crack is instead governed by the polynomial function $s_{xx}(r)$, which in turn complies with $s_{xx}(r=0)=0$ and is derived from Finite Element analyses.

The performed Finite Element analyses showed that the SCB presents a monotonically decreasing $\sigma_{xx}(r,P)$ and a monotonically increasing $K_I(a,P)$ in both notched and unnotched configurations. As such, the quasi-static FFM-avg failure force P_f and critical crack advance Δa_f can be determined through the following system of two equations:

$$\begin{cases} P_f = \dfrac{\sigma_C BR\Delta a_f}{\displaystyle\int_0^{\Delta a_f} S_{xx}(r)\,\mathrm{d}r} \\ P_f = \dfrac{K_{IC}BR\sqrt{\Delta a_f}}{\sqrt{\pi\displaystyle\int_0^{\Delta a_f}(a_0+a)\,F^2(a_0+a)\,\mathrm{d}a}} \end{cases} . \tag{6.15}$$

Then, applying Eq. (6.11) to the monotonically increasing in time loading from Eq. (6.12), one can obtain the DFFM prediction for the dynamic failure force P_{t_f} in terms of the loading rate $\dot{P}$, which writes as:

$$P_{t_f} = \begin{cases} P_f + \dfrac{\dot{P}\tau}{2} & \text{if } \dot{P} < \dfrac{2P_f}{\tau} \\ \sqrt{P_f}\sqrt{2\dot{P}\tau} & \text{if } \dot{P} \geq \dfrac{2P_f}{\tau} \end{cases} . \tag{6.16}$$

Therefore, the dynamic failure force P_{t_f} is seen to increase monotonically with $\dot{P}$ from its quasi-static value P_f, although not uniformly: for slow enough loadings, P_{t_f} grows proportionally to $\dot{P}$; for higher rates instead, P_{t_f} becomes proportional to $\sqrt{\dot{P}}$. In any case, the evolution of P_{t_f} with $\dot{P}$ is ensured continuous and smooth all along. Dividing both sides of Eq. (6.16) by $\dot{P}$, one can obtain the DFFM prediction for the time to failure t_f as follows:

$$t_f = \begin{cases} \dfrac{P_f}{\dot{P}} + \dfrac{\tau}{2} & \text{if } \dot{P} < \dfrac{2P_f}{\tau} \\ \sqrt{P_f}\sqrt{\dfrac{2\tau}{\dot{P}}} & \text{if } \dot{P} \geq \dfrac{2P_f}{\tau} \end{cases} . \tag{6.17}$$

Just as expected, t_f tends to infinity for very slow loadings, it reducing as $\dot{P}$ grows. Eventually, t_f turns equal to τ when $\dot{P} = \dot{P}^* = 2P_f/\tau$ and triggers the aforementioned change in the rate dependence of failure. In what follows, cases where $t_f > \tau$ will be referred to as Regime I failure, otherwise it will be referred to as Regime II. The underlying differences between these two failure regimes reveal evident after the graphical representations in Fig. 6.4, which illustrate how the non-instantaneous assessment of the DFFM interacts with the piecewise defined load P_t from Eq. (6.12) for different loading rates $\dot{P}$.

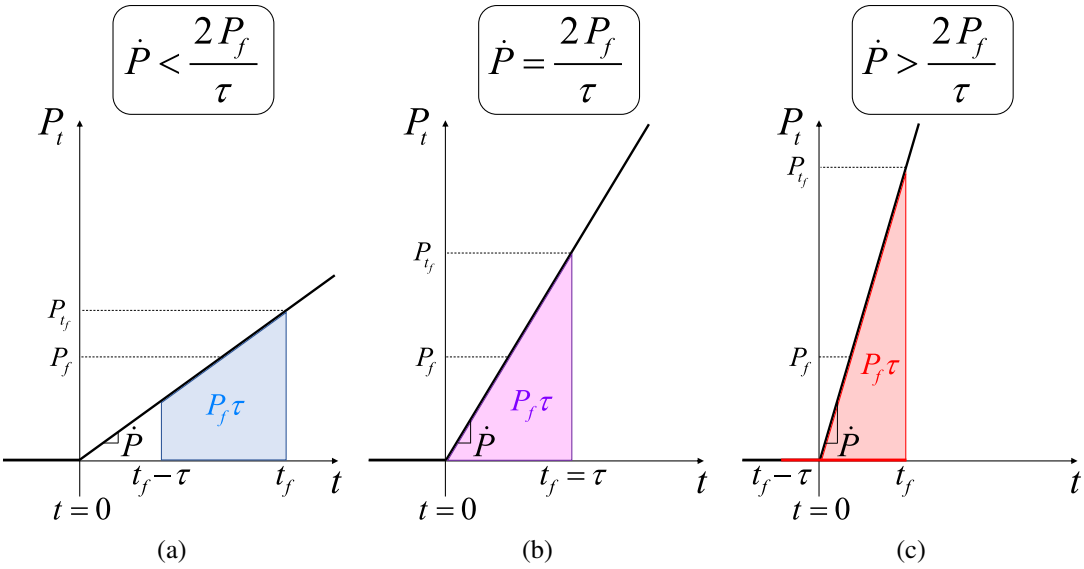

Fig. 6.4 Illustration of the non-instantaneous assessment of the DFFM approach for a dynamic load P_t as in Eq. (6.11) upon failure: (a) in Regime I, (b) in between Regime I and II, and (c) in Regime II.

6.5.2 Brazilian Disk test

Since the SCB test yields a non-constant distribution of the crack opening stress component, it is not suitable for characterizing the tensile strength on its own. Instead, the BD test is commonly used for this purpose given its fairly constant stress field. Once again, BD specimens are obtained directly from a drilled rock core, these being characterized by only its radius R and thickness B. Besides, the loading P_t is applied analogously to that of the SCB (see Fig. 6.3b).

Just as in the SCB case, the midplane is the region most favourable to the appearance of tensile failure. Except from the surroundings of the contact points, the

crack opening stress component σ_{xx} is almost constant and can be approximated as:

$$\sigma_{xx}(P) = \frac{P}{BR}\left(\frac{1}{\pi}\right). \tag{6.18}$$

Hence, the homogeneity in the governing stress component renders the energy condition irrelevant for the determination of the quasi-static failure force P_f according to FFM-avg, which collapses to a maximum tensile stress criterion and yields:

$$P_f = \sigma_C BR\pi. \tag{6.19}$$

If the BD specimen is dynamically loaded per P_t in Eq. (6.12), the DFFM predictions for the rate dependence of P_{t_f} and t_f remain as in Eqs. (6.16) and (6.17).

6.5.3 Material characterization and comparison with experimental results

The experimental results here used for comparison with the DFFM predictions comprise dynamic tests on NSCB [146], USCB [145] and BD [144] specimens. Given that all these three experimental campaigns were conducted using the same material and testing technique, the DFFM predictions would ideally correlate all the test results using a fixed triad $\{\sigma_C, K_{IC}, \tau\}$ of properties. Nonetheless, the natural origin of the rocks and its inhomogeneity introduces certain variability, especially in what concerns the energy release upon fracture (see e.g. [149]). To account for the uncertainty, K_{IC} was independently obtained for the NSCB and USCB sets of experiments, whereas σ_C and τ were concurrently determined and kept constant for all three studied cases.

Per the constant crack opening stress distribution in the BD test, the value for σ_C was directly obtained from the reported P_f by using Eq. (6.19). For the USCB tests, the particularization of Eq. (6.15) allows determining K_{IC} from the values of P_f and σ_C. On the other hand, the experimental result for P_f in the NSCB case was not available in [146], it being instead determined through a best-fitting procedure with the dynamic results. Remarkably, for fixed σ_C and τ, changes in K_{IC} mostly manifests as vertical translations of the predicted failure curve, its shape

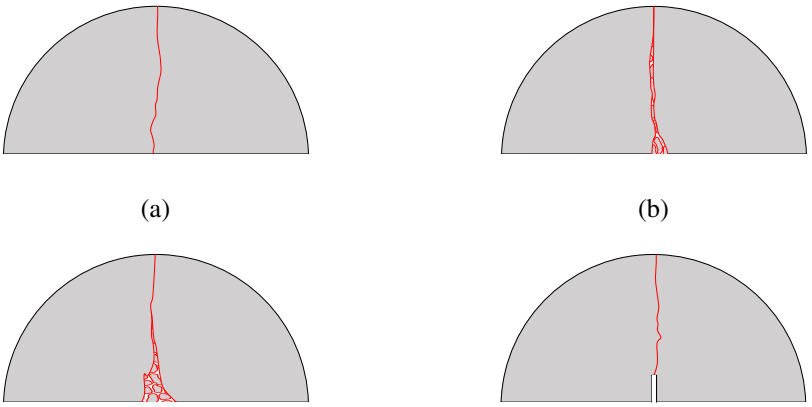

Fig. 6.5 Illustration of the failure patterns of: (a) USCB with $t_f = 64.17\ \mu$s, (b) USCB with $t_f = 40.02\ \mu$s, (c) USCB with $t_f = 31.74\ \mu$s, and (d) NSCB with $t_f = 46.23\ \mu$s. Artwork approximately to scale with respect to figures reported in [145] for the USCBs and [146] for the NSCB.

barely changing. Therefore, the fitting procedure has very limited impact on the representativeness of the comparison between predictions and experiments.

For determining the remaining parameter τ, one should first recall its given physical interpretation, i.e. the minimum time required for microcracks to coalesce into a single macrocrack. Thereof, for smeared stress concentrations such as the USCB test, failure patterns can shift from fracture surfaces to damaged regions as $\dot{P}$ grows (see Fig. 6.5). Still, the DFFM proposal from Section 6.4 relies on the energy released by a sharp crack, thus lacking accuracy to capture diffused damage and potentially affecting the proper determination of τ. To avoid this, a highly localized stress concentration can be used instead, e.g. the NSCB test, which showcases the DFFM-friendly crack-like failure for considerably high loading rates. The use of only NSCB results for determining τ is therefore deemed more adequate. Changes in this parameter for fixed σ_C and K_{IC} result in curves with different slopes but constant quasi-static predictions, thus being somewhat uncoupled from the aforementioned determination of K_{IC}.

Now, for each of the three sets of experiments considered, the geometrical definition and resulting material properties are reported in Table 6.1. Using these, the comparison between the DFFM and the experimental results is given in Fig. 6.6. Per the DFFM hypotheses, only the purely dynamic cases reported in the references

Table 6.1 References, specimen characteristics and material properties used for the comparison between DFFM and experiments.

Reference	**Geometry**	**Dimensions**				**Material properties**		
		B	R	$2S$	a_0	σ_C	K_{IC}	τ
		[mm]	[mm]	[mm]	[mm]	[MPa]	[MPa$\sqrt{\text{m}}$]	[μs]
[146]	NSCB	25	25	27.5	5	12.8	3.2	69.0
[145]	USCB	25	25	27.5	–	12.8	2.9	69.0
[144]	BD	16	20	–	–	12.8	–	69.0

were considered. From these figures, it is evident that DFFM is able to nicely capture the rate dependence of failure when $t_f > \tau$ for all three setups, which clearly proves to be mostly linear.

On the other hand, the agreement between DFFM and experiments is not completely convincing for loading rates yielding $t_f < \tau$: while it is very accurate for NSCB tests, substantial overshooting is observed in both USCB and BD cases. Moreover, the extent of the difference grows with the loading rate, reaching up to 20% for the cases here considered. A potential explanation for this growing disagreement can be found in the aforementioned inadequacy of the DFFM crack-like energy release as opposed to that of the actual damaged region. As seen in Figs. 6.5 (a) to (c), the larger the loading rate, the wider the damaged region in the USCB specimen is. As such, the energy released per unit length of crack onset is noticeably underestimated if a sharp crack is assumed, thus resulting in the overprediction of the failure load. Indeed, if a larger effective energy release per unit crack growth was instead considered, i.e. a larger K_I^2, the failure load predictions would be reduced for a given loading rate, thus better approximating the experimental results.

Lastly, the rate dependence of failure is jointly illustrated for the three considered setups in Fig. 6.6d. Therein, the apparent strengthening ratio P_{t_f}/P_f is shown as a function of the time to failure t_f normalized by τ. This figure suggests that the dynamic dependence of failure is mostly independent of the specimen geometry since all three clouds of points collapse almost perfectly. This result supports the interpretation of τ as a fixed material property, yet much more comprehensive experimental data is required to determine the limitations of this statement.

To conclude, it is natural to wonder how good the approaches presented in Section 6.3 would perform for the cases at hand. For instance, both DFFM and IT

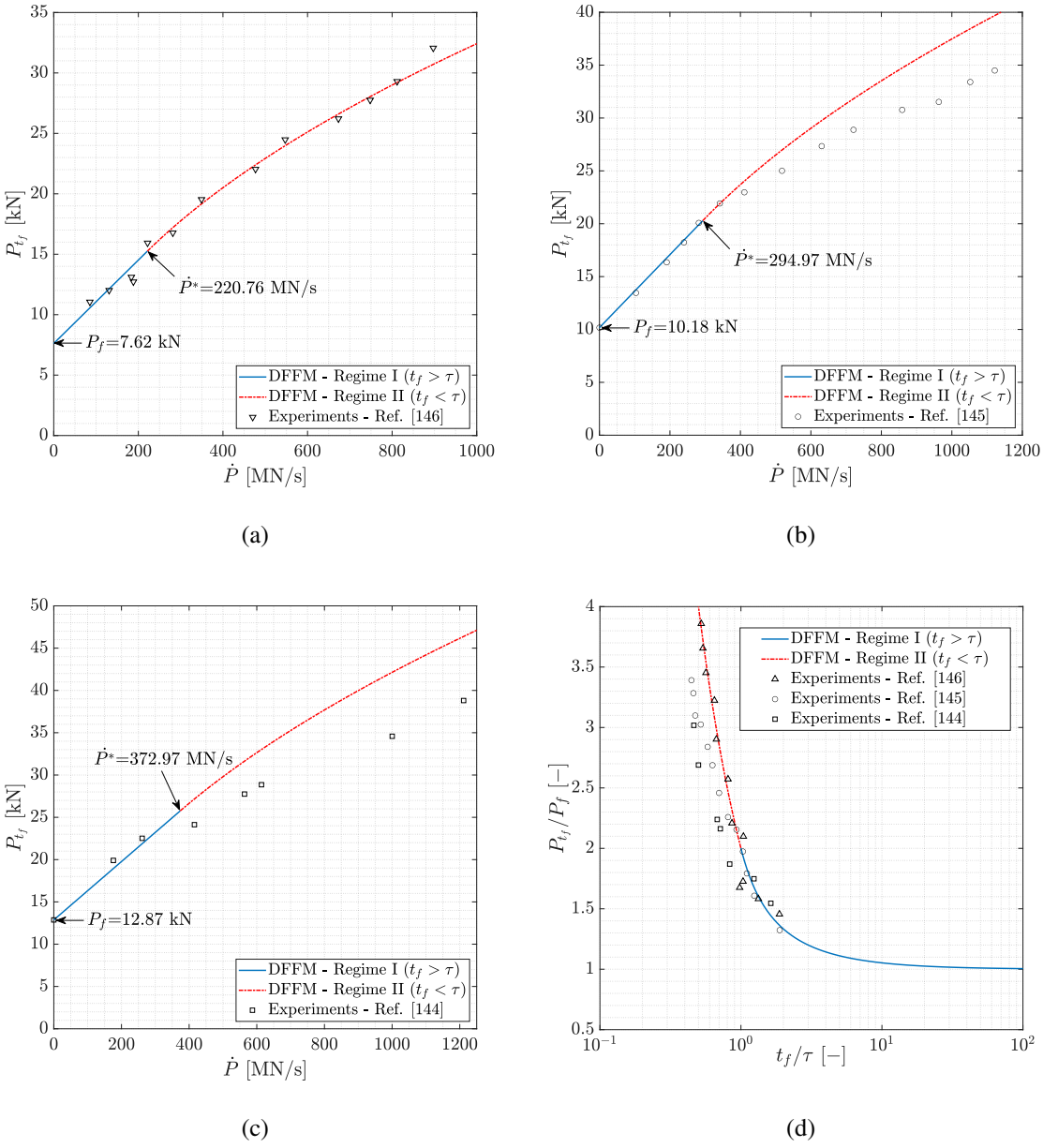

Fig. 6.6 Comparison of the DFFM predictions with dynamic experimental results for: (a) NSCB specimens [146], (b) USCB specimens [145], (c) BD specimens [144], and (d) all three geometries.

criteria yield identical predictions upon the constant stress BD setup. For the SCBs instead, the properties in Table 6.1 would result in the IT's characteristic length d being larger than the specimen itself, hence rendering the approach inadequate. Regarding the DTCD and the "Classical dynamic approaches", the arbitrariness in

the strength/toughness rate dependency functions renders their accuracy a result of proper fitting rather than of model representativeness. Lastly, the DQFM approach was found to only be applicable to certain combinations of the specimen geometry and material properties, otherwise yielding complex values for the failure load. Likewise, the crack growth quanta Δa resulted larger than the specimens themselves if the properties in Table 6.1 are used.

6.6 Conclusions

The extension to dynamic loadings of the Finite Fracture Mechanics approach for crack nucleation has been undertaken. The key point of the present proposal was to regard crack initiation as a process that unfolds over a certain material-dependent time lapse. To account for this, the non-local stress and energy conditions of the quasi-static approach are modified to reproduce the non-instantaneous nature of the problem. Therefore, the proposed dynamic criterion retains the ability of Finite Fracture Mechanics to interplay with the structure at hand, revealing more versatile than previous proposals.

The accuracy of the proposed approach was evaluated by comparing the resultant failure predictions against three different sets of experiments available in the literature. These empirical studies were all conducted on the same material and with similar techniques, thus allowing cross-referencing. Furthermore, the tested geometries showcased very different stress distributions, namely constant profiles, non-singular stress concentrations, and singular stress intensifications. In all three cases, the Dynamic Finite Fracture Mechanics approach was proven to reproduce the experimental results reasonably well. At this point, four main conclusions can be drawn:

- Dynamic Finite Fracture Mechanics predicts two crack nucleation regimes separated by a threshold in the time to fracture. This feature is supported by the empirical evidence on rock specimens: for slow loadings failure is observed to develop as a single crack; whereas for fast loading failure diffuses and multiple cracks are formed.

- For low loading rates yielding a single macrocrack, the rate dependence of failure is captured accurately by the Dynamic Finite Fracture Mechanics approach regardless of the geometry considered.
- At higher loading rates however, the merge of microcracks into a single macrocrack is not complete. This leads to two distinct scenarios depending on the type of stress concentration: for geometries with highly localized stress raisers, failure remains pretty much fracture-like and the Dynamic Finite Fracture Mechanics modelling hypotheses remain mostly valid; for plain geometries instead, the diffusion of failure is more pronounced, thus undermining the validity of a crack-like failure profile. As such, Dynamic Finite Fracture Mechanics' failure load predictions in the former cases resulted considerably more accurate than in the latter.
- The experimental results suggest that the coalescence period does not show a significant dependence on the specimen geometry or the pre-crack stress distribution. These observations bolster the hypothesis that the coalescence period is primarily dependent on the material, at least in the event of self-similar dynamic loading profiles.

Although the Dynamic Finite Fracture Mechanics approach proposed in this study is promising, there are still some unresolved issues that require further study. For example, the current formulation is not sufficiently developed to adequately manage the interaction between static prestressing and dynamic loads, being only applicable to either quasi-static or dynamic scenarios. Similarly, the coalescence period needs to be further characterized for various materials, loading profiles, and specimen geometries. This would provide a more comprehensive understanding of its dependency on the setup characteristics. Eventually, further work is needed towards addressing the generalization to more extreme loading cases where both the stress field and the energy release present an explicit dependence with t besides that of Σ_t, i.e. when these get defined as $\boldsymbol{\sigma}(\underline{x}, \Sigma_t, t)$ and $G_{\text{dyn}}(a, \Sigma_t, t)$.

Chapter 7

Conclusions and Further Research

7.1 Conclusions

The modelling of dynamic fracture by means of the Phase Field fracture model and the Finite Fracture Mechanics criterion has been extensively covered throughout this thesis. Exploiting the complementary nature of the two considered approaches, the understanding of this complex and rather important aspect of failure has been faced twofold, from both a theoretically rigorous and detailed perspective, as well as from an engineering and industrial-like standpoint. Overall, a bottom-up approach to each framework has been followed, always starting from the well-established quasi-static formulations to then progressively adding layers of complexity until eventually reaching the coveted dynamic context.

Particularly for the Phase Field fracture model, its evolution from the inceptual variational revisitation of brittle fracture up to the modern generalized formulation has been covered in the first place so as to provide a solid comprehension of the approach background. Its theoretical framework and weak form were then developed, also providing detailed insights into the resulting modelling degrees of freedom and the peculiarities of the most popular choices of the many available. The great potential of the approach to deal with fracture initiation under multiaxial stress states was ascertained using a simple yet exhaustive benchmark setup: the crack onset from a circular hole under remote biaxial loading. Taking Dugdale's Cohesive Zone Model as a reference for validation, it was observed that the Phase Field fracture model resulted accurate when coupled with the No-Tension energy decomposition and the

AT1 modelling functions. Once conveyed the basic paradigm of Phase Field fracture modelling, the approach was taken to a dynamic context by virtue of Hamilton's principle for irreversible evolutions. The main technical aspects concerning its efficient numerical implementation in a Finite Element environment by using an explicit time integrator were covered. The resulting formulation has been exploited to study the post-punch fragmentation of a biaxially pre-strained glass pane, providing clear evidence of the approach capability to inherently deal with highly-complex crack patterns and dynamic evolutions. Eventually, the quasi-static and dynamic variants of the Phase Field fracture model are juxtaposed in the case of unstable fracture under quasi-static loadings. Through several bespoke case studies that include analytical, numerical and experimental results, it was vehemently proven that quasi-static models of fracture are neither suitable nor safe for reproducing unstable crack growth. As such, the ultimate conclusion from this first thematic block is that any fracturing event is essentially dynamic and that quasi-static simplifications should be carefully applied.

On the other hand, the Finite Fracture Mechanics approach to crack nucleation was used in the aim of providing a cost-effective and robust tool for predicting the happening of failure. Once again, the framework potential to predict crack nucleation was first investigated under quasi-static loading conditions, whereof two scenarios were considered. The first consisted in an infinite uniaxially tensioned domain containing a single spherical void of varying radius, and the Finite Fracture Mechanics was proven to yield reasonable predictions of the size-dependent failure load in comparison with Dugdale's Cohesive Zone Model, as well as with relevant experimental results and atomistic simulations. Furthermore, the considerably more complex study of failure onset from a circular hole under remote biaxial loading was resumed, and the resultant predictions showed fair agreement with those previously obtained. Moving towards the study of failure onset under dynamic loadings, the conventional Finite Fracture Mechanics formulation first required introducing modifications in order to account for the now-significant loading rate. To achieve this in an ordered manner, a high-level discussion on the requirements of an ideal dynamic fracture criterion was first presented and then used for evaluating relevant dynamic failure criteria proposed in the literature. Based on the resultant insights, a proposal for the Dynamic Finite Fracture Mechanics coupled criterion was made by introducing a non-instantaneous assessment in the spirit of the Incubation Time concept. The novel approach was then particularized to certain case studies, and the

subsequent comparison with results from the corresponding dynamic experiments yielded satisfactory agreement.

Of course, albeit it has been attempted that the conducted analyses were detailed and exhaustive, the presented research does not embody a definitive answer to the undertaken task. Instead, it is seen as a solid contribution towards the better comprehension of the complex phenomenon of dynamic fracture and its modelling. In this regard, some of the unresolved questions that are reckoned to be of utter importance are shortlisted in the final section.

7.2 Further Research

In view of the insights acquired during the development of the present thesis, the following still-to-be-addressed aspects have been identified as the most important ones:

- The use of explicit time integrators in the dynamic Phase Field fracture model, although computationally efficient, precludes the use of alternate minimization techniques for solving the staggered variational principles. Hence, whether the obtained results are a good approximation of the actual monolithic solution is actually unknown, and thus a proper analysis on this regard should be conducted. For instance, this can be done by comparing the results from the explicit time integrator against those of an implicit time integrator with alternate minimization. In any case, it is highlighted that per the learnings in Chapter 4 regarding the robustness of the irreversibility condition, very refined temporal resolution is a must for ensuring the representativeness of the fracture predictions, regardless of the stability of the time integrator.

- The experimental validation of the dynamic Phase Field fracture model must be taken considerably further in subsequent studies, for example by including quantitative comparisons, more detailed observations and richer sets of data. Likewise, the use of better comprehended materials behaviour-wise can also improve the quality of the experimental validation. However, it is here reckoned that the best quality information for empirically validating the dynamic fracture models comes from the use of high-speed cameras to visually capture

(and extract *in situ* information of) the actual crack onset and propagation events.

- The proposed formulation of the Dynamic Finite Fracture Mechanics criterion is based upon some strong assumptions on how the dynamic loading relates to the stress field and the release of energy upon fracture. Of course, it should be investigated how to generalize the formulation by dropping such assumptions. Likewise, it remains pending the task of figuring out how to efficiently implement the Finite Fracture Mechanics approach, in both quasi-static and dynamic variants, for the cases where the prospective crack paths are not well defined.

- Just as mentioned above, more comprehensive experimental validation is required in order to further develop the Dynamic Finite Fracture Mechanics approach. In particular, this should cover specimens of different shapes, sizes and materials so as to determine the dependency of the various parameters used (or lack thereof). In this regard, using the modified Split Hopkinson Pressure Bar with the pulse shaping technique is highly recommended for it allows to trim the actual dynamic loading profile exerted on the samples, which is an aspect found to be often overlooked in dynamic experimental campaigns.

While the discussions and contents enclosed in this thesis are fundamentally theoretical, they serve a critical purpose: to assess, develop and refine the modelling tools necessary for the resolution of real-world problems. The knowledge generated herein is thereby not an end in itself, but a leap towards practical applications. Hence, further research activities should be devoted to ensure that these theoretical advancements do get translated into tangible, real-world solutions from which society can benefit.

7.3 Conclusioni (ITA)

La modellazione della frattura dinamica attraverso il modello di frattura del Campo di Fase e il criterio della Meccanica della Frattura Finita è stata ampiamente trattata in questa tesi. Sfruttando la natura complementare dei due approcci considerati, la comprensione di questo aspetto complesso e piuttosto importante della rottura

dei materiali è stata affrontata in due modi, sia da una prospettiva teoricamente rigorosa e dettagliata, sia da un punto di vista ingegneristico e industriale. Nel complesso, si è seguito un approccio dal basso verso l'alto per ciascuna metodologia, partendo sempre dalle formulazioni quasi-statiche ben consolidate per poi aggiungere progressivamente strati di complessità fino a raggiungere infine il contesto dinamico.

In particolare per il modello di frattura con Campo di Fase, la sua evoluzione sin dalla rivisitazione variazionale iniziale della frattura fragile fino alla formulazione generalizzata moderna è stata descritta *in primis* al fine di fornire una solida comprensione del background dell'approccio. Sono stati quindi sviluppati il suo quadro teorico e la forma debole, fornendo anche spunti dettagliati sui gradi di libertà risultanti nella modellazione e le particolari scelte più popolari tra le tante disponibili. Il grande potenziale dell'approccio per affrontare l'innesco della frattura sotto stati di stress multiassiali è stato accertato utilizzando un semplice ma esaustivo test di confronto, ossia analizzando la rottura da un foro circolare sotto carico biassiale remoto. Prendendo come riferimento il Modello di Zona Coesiva di Dugdale, si è osservato che il modello di frattura con Campo di Fase risulta accurato quando si utilizza la decomposizione dell'energia No-Tension assieme alle funzioni di modellazione AT1. Una volta descritto il paradigma di base della modellazione della frattura con Campo di Fase, l'approccio è stato applicato in un contesto dinamico in virtù del principio di Hamilton per le evoluzioni irreversibili. Sono stati coperti i principali aspetti tecnici riguardanti la sua efficiente implementazione numerica in base al metodo degli Elementi Finiti utilizzando un integratore temporale esplicito. La formulazione risultante è stata poi utilizzata per studiare la frammentazione post-punch di un pannello in vetro biassialmente pre-caricato, fornendo chiare prove della capacità dell'approccio di affrontare intrinsecamente pattern di fessure altamente complessi ed anche evoluzioni dinamiche. Infine, entrambi le varianti quasi-statiche e dinamiche del modello di frattura con Campo di Fase sono giustapposte nel caso di frattura instabile sotto carichi quasi-statici. Attraverso diversi studi dedicati che includono risultati analitici, numerici e sperimentali, è stato dimostrato con forza che i modelli quasi-statici di frattura non sono né adatti né sicuri per riprodurre lo sviluppo instabile della frattura. In conclusione, a seguito dei risultati ottenuti possiamo affermare che qualsiasi evento di frattura è essenzialmente dinamico e che le semplificazioni quasi-statiche dovrebbero essere applicate con somma cura.

D'altra parte, l'approccio della Meccanica della Frattura Finita all'innesco della rottura è stato utilizzato con l'obiettivo di fornire uno strumento robusto e veloce

per prevedere l'insorgenza della frattura. Ancora una volta, il potenziale del criterio per prevedere l'innesco della rottura è stato prima investigato sotto condizioni di carico quasi-statico, considerando due scenari diversi. Il primo consisteva in un dominio infinito sottoposto a tensione uniassiale contenente un singolo poro sferico di raggio variabile, e per il quale si è dimostrato che la Meccanica della Frattura Finita fornisce previsioni ragionevoli del carico di rottura dipendente dalla dimensione del poro, e che risultano in accordo con quelle ottenute attraverso il Modello di Zona Coesiva di Dugdale o simulazioni atomiche, così come coi risultati sperimentali. Inoltre, lo studio considerevolmente più complesso dell'innesco di rottura da un foro circolare sotto carico biassiale remoto è stato ripreso, e le previsioni risultanti hanno mostrato di essere in accordo con quelle precedentemente ottenute. Muovendosi verso lo studio dell'innesco della rottura sotto carichi dinamici, la formulazione convenzionale della Meccanica della Frattura Finita è stata prima modificata per tener conto dell'influenza dell'ora significativa velocità di carico. Per raggiungere questo obbiettivo in modo strutturato, si è prima condotta una discussione di alto livello sui requisiti di un criterio di frattura dinamica ideale, per valutare i criteri di rottura dinamica più rilevanti proposti in letteratura. Sulla base delle intuizioni risultanti, è stato proposto un criterio accoppiato della Meccanica della Frattura Finita Dinamica attraverso una valutazione non istantanea, nello spirito del concetto di Tempo di Incubazione. Il nuovo approccio è stato poi particolarizzato per alcuni casi di studio, e il successivo confronto con i risultati degli esperimenti dinamici corrispondenti ha dimostrato un accordo soddisfacente.

Naturalmente, sebbene siano state condotte analisi dettagliate ed esaustive, la ricerca qui presentata non costituisce una risposta definitiva al problema analizzato. Invece, essa è vista come un solido contributo verso una migliore comprensione del complesso fenomeno della frattura dinamica e della sua modellazione.

7.4 Conclusiones (ESP)

El modelado de la fractura dinámica mediante el modelo de fractura con Campo de Fase y el criterio de rotura de la Mecánica de la Fractura Finita se ha cubierto en detalle a lo largo de esta tesis. Aprovechando la naturaleza complementaria de los dos enfoques considerados, se ha abordado la comprensión de este aspecto complejo y bastante importante del fallo en dos modos diferentes, tanto desde

una perspectiva teóricamente rigurosa y detallada, como desde un punto de vista ingenieril e industrial. En general, para cada técnica de modelado se ha seguido un enfoque ascendente, comenzando siempre desde las formulaciones cuasi-estáticas, las cuales están bien establecidas, para luego ir progresivamente añadiendo capas de complejidad hasta finalmente llegar al caso dinámico.

Particularmente para el modelo de fractura con Campo de Fase, se ha cubierto en primer lugar su evolución desde la revisión variacional de la fractura frágil primigenia hasta la formulación generalizada moderna en modo de proporcionar una comprensión sólida de la metodología. A continuación, se ha desarrollado tanto el marco teórico y como su forma débil, proporcionando también ideas detalladas sobre los grados de libertad de modelado resultantes y las particularidades de las opciones más populares de entre las muchas disponibles. El gran potencial del enfoque para tratar la iniciación de la fractura bajo estados de tensión multiaxial se ha constatado a través de un estudio de referencia simple pero exhaustivo: la nucleación de grieta a partir de un agujero circular bajo una carga biaxial remota. Tomando el Modelo de Zona Cohesiva de Dugdale como referencia, se ha observado que el modelo de fractura con Campo de Fase resulta preciso cuando se acoplan la descomposición de energía No-Tensión y las funciones AT1. Después de desarrollar el paradigma cuasi-estático del modelado de fractura con Campo de Fase, esta metodología se ha llevado al contexto dinámico en virtud del principio de Hamilton para evoluciones irreversibles. Además, se han cubierto en detalle los principales aspectos técnicos relacionados con su eficiente implementación numérica utilizando el método de los Elementos Finitos y un integrador de tiempo explícito. La formulación resultante se ha utilizado para estudiar la fragmentación post-punzonado de un panel de vidrio pre-cargado biaxialmente, cuyos resultados han evidenciado claramente la capacidad del enfoque para tratar intrínsecamente tanto patrones de grietas complejos como evoluciones dinámicas. Finalmente, las variantes cuasi-estáticas y dinámicas del modelo de fractura con Campo de Fase se han yuxtapuesto para casos de fractura inestable y cargas cuasi-estáticas. En particular, se ha demostrado vehementemente que los modelos cuasi-estáticos de fractura no son ni adecuados ni seguros para reproducir el crecimiento inestable de grietas a través de varios estudios de caso, los cuales incluyen resultados analíticos, numéricos y experimentales. Como tal, de este primer bloque temático se puede concluir que cualquier evento de rotura es esencialmente dinámico, y que por tanto las simplificaciones cuasi-estáticas deben siempre aplicarse con sumo cuidado.

Por otro lado, el enfoque de la Mecánica de Fractura Finita para la nucleación de grietas se ha utilizado con el objetivo de proporcionar una herramienta robusta y rentable para predecir la ocurrencia de fallos. Una vez más, el potencial del marco para predecir la nucleación de grietas bajo condiciones de carga cuasi-estáticas se ha desarrollado en primer lugar, habiéndose considerado dos escenarios diferentes. En el primero se ha estudiado un dominio infinito bajo tracción uniaxial que contiene un solo poro esférico de radio variable, y para el cual se ha demostrado que la Mecánica de Fractura Finita proporciona predicciones razonables del efecto del radio en la carga de fallo en comparación con el Modelo de Zona Cohesiva de Dugdale, así como con resultados experimentales relevantes y simulaciones atómicas. Además, el estudio considerablemente más complejo del inicio del rotura desde un agujero circular bajo carga biaxial remota se ha retomado en este segundo bloque, y las predicciones de la Mecánica de la Fractura Finita se han mostrado en consonancia con las obtenidas previamente. Pasando al estudio del inicio del fallo bajo cargas dinámicas, la formulación convencional de la Mecánica de Fractura Finita ha sido modificada para tener en cuenta la ahora significativa velocidad de carga. Para lograr esto de forma ordenada, primero se ha presentado una discusión de alto nivel sobre los requisitos que debe cumplir un criterio de fractura dinámica ideal, a partir de la cual se han evaluado los criterios de fallo dinámico propuestos en la literatura. Basándose en las conclusiones obtenidas, se ha presentado una propuesta para el criterio de la Mecánica de Fractura Finita Dinámica basada en una evaluación no instantánea, siguiendo el concepto del Tiempo de Incubación. Finalmente, la nueva formulación se ha validado mediante la particularización a diversos estudios de caso, en los que la correlación entre predicciones y resultados experimentales resulta satisfactoria.

Por supuesto, aunque se ha intentado que los análisis realizados fueran detallados y exhaustivos, la investigación presentada no encarna la respuesta definitiva a la tarea emprendida. En cambio, esta sí que se ve como una sólida contribución hacia una mejor comprensión del complejo fenómeno de la fractura dinámica y su modelado.

References

[1] I. Newton. *Philosophiæ naturalis principia mathematica*. Londini, iussu Societatis Regiae ac typis Josephi Streater, 1687.

[2] A. A. Griffith. VI. The phenomena of rupture and flow in solids. *Philosophical Transactions of the Royal Society of London. Series A, Containing Papers of a Mathematical or Physical Character*, 221(582-593):163–198, 1921.

[3] G. R. Irwin. Analysis of Stresses and Strains Near the End of a Crack Traversing a Plate. *Journal of Applied Mechanics*, 24(3):361–364, 1957.

[4] C. E. Inglis. Stresses in Plates Due to the Presence of Cracks and Sharp Corners. *Transactions of the Institute of Naval Architects*, 55:219–241, 1913.

[5] H. M. Westergaard. Bearing Pressures and Cracks: Bearing Pressures Through a Slightly Waved Surface or Through a Nearly Flat Part of a Cylinder, and Related Problems of Cracks. *Journal of Applied Mechanics*, 6(2):A49–A53, 1939.

[6] M. L. Williams. On the Stress Distribution at the Base of a Stationary Crack. *Journal of Applied Mechanics*, 24(1):109–114, 1957.

[7] E. H. Yoffe. LXXV. The moving Griffith crack. *The London, Edinburgh, and Dublin Philosophical Magazine and Journal of Science*, 42(330):739–750, 1951.

[8] B. R. Baker. Dynamic Stresses Created by a Moving Crack. *Journal of Applied Mechanics*, 29(3):449–458, 1962.

[9] L. B. Freund. Crack propagation in an elastic solid subjected to general loading—III. Stress wave loading. *Journal of the Mechanics and Physics of Solids*, 21(2):47–61, 1973.

[10] K. Ravi-Chandar and W. G. Knauss. An experimental investigation into dynamic fracture: I. Crack initiation and arrest. *International Journal of Fracture*, 25(4):247–262, 1984.

[11] K. Ravi-Chandar and W. G. Knauss. An experimental investigation into dynamic fracture: II. Microstructural aspects. *International Journal of Fracture*, 26(1):65–80, 1984.

[12] K. Ravi-Chandar and W. G. Knauss. An experimental investigation into dynamic fracture: III. On steady-state crack propagation and crack branching. *International Journal of Fracture*, 26(2):141–154, 1984.

[13] K. Ravi-Chandar and W. G. Knauss. An experimental investigation into dynamic fracture: IV. On the interaction of stress waves with propagating cracks. *International Journal of Fracture*, 26(3):189–200, 1984.

[14] D. S. Dugdale. Yielding of steel sheets containing slits. *Journal of the Mechanics and Physics of Solids*, 8(2):100–104, 1960.

[15] G. I. Barenblatt. The mathematical theory of equilibrium cracks in brittle fracture. *Advances in Applied Mechanics*, 7:55–129, 1962.

[16] X.-P. Xu and A. Needleman. Numerical simulations of fast crack growth in brittle solids. *Journal of the Mechanics and Physics of Solids*, 42(9):1397–1434, 1994.

[17] G. T. Camacho and M. Ortiz. Computational modelling of impact damage in brittle materials. *International Journal of Solids and Structures*, 33(20):2899–2938, 1996.

[18] M. Vocialta, N. Richart, and J.-F. Molinari. 3D dynamic fragmentation with parallel dynamic insertion of cohesive elements. *International Journal for Numerical Methods in Engineering*, 109(12):1655–1678, 2017.

[19] M. Vocialta, M. Corrado, and J.-F. Molinari. Numerical analysis of fragmentation in tempered glass with parallel dynamic insertion of cohesive elements. *Engineering Fracture Mechanics*, 188:448–469, 2018.

[20] T. Laschuetza and T. Seelig. Remarks on dynamic cohesive fracture under static pre-stress — with a comparison to finite fracture mechanics. *Engineering Fracture Mechanics*, 242:107466, 2021.

[21] M. Vieira de Carvalho, I. A. Rodrigues Lopes, and F. M. Andrade Pires. On the solution of unstable fracture problems with non-linear cohesive laws. *Engineering Fracture Mechanics*, 295:109736, 2024.

[22] G. A. Francfort and J.-J. Marigo. Revisiting brittle fracture as an energy minimization problem. *Journal of the Mechanics and Physics of Solids*, 46(8):1319–1342, 1998.

[23] B. Bourdin, G. A. Francfort, and J.-J. Marigo. Numerical experiments in revisited brittle fracture. *Journal of the Mechanics and Physics of Solids*, 48(4):797–826, 2000.

[24] C. Miehe, M. Hofacker, and F. Welschinger. A phase field model for rate-independent crack propagation: Robust algorithmic implementation based on operator splits. *Computer Methods in Applied Mechanics and Engineering*, 199(45-48):2765–2778, 2010.

[25] K. Pham, H. Amor, J.-J. Marigo, and C. Maurini. Gradient damage models and their use to approximate brittle fracture. *International Journal of Damage Mechanics*, 20(4):618–652, 2011.

[26] J.-J. Marigo, C. Maurini, and K. Pham. An overview of the modelling of fracture by gradient damage models. *Meccanica*, 51(12):3107–3128, 2016.

[27] C. J. Larsen, C. Ortner, and E. Süli. Existence of solutions to a regularized model of dynamic fracture. *Mathematical Models and Methods in Applied Sciences*, 20(07):1021–1048, 2010.

[28] B. Bourdin, C. J. Larsen, and C. L. Richardson. A time-discrete model for dynamic fracture based on crack regularization. *International Journal of Fracture*, 168(2):133–143, 2011.

[29] T. Y. Li, J.-J. Marigo, D. Guilbaud, and S. Potapov. Gradient damage modeling of brittle fracture in an explicit dynamics context. *International Journal for Numerical Methods in Engineering*, 108(11):1381–1405, 2016.

[30] J. Bleyer, C. Roux-Langlois, and J.-F. Molinari. Dynamic crack propagation with a variational phase-field model: limiting speed, crack branching and velocity-toughening mechanisms. *International Journal of Fracture*, 204(1):79–100, 2017.

[31] J. Bleyer and J.-F. Molinari. Microbranching instability in phase-field modelling of dynamic brittle fracture. *Applied Physics Letters*, 110(15):151903, 2017.

[32] F. Tian, J. Zeng, X. Tang, T. Xu, and L. Li. A dynamic phase field model with no attenuation of wave speed for rapid fracture instability in hyperelastic materials. *International Journal of Solids and Structures*, 202:685–698, 2020.

[33] G. Galilei. *Discorsi e dimostrazioni matematiche intorno a due nuove scienze*. House of Elzevir, 1638.

[34] W. J. M. Rankine. II. On the stability of loose earth. *Philosophical Transactions of the Royal Society of London*, 147:9–27, 1857.

[35] H. Neuber. *Theory of Notch Stress: Principles for Exact Calculation of Strength with Reference to Structural form and Material*. Springer Verlag, 1958.

[36] V. Novozhilov. On a necessary and sufficient condition for brittle strength. *Prikladnaya Mathematika i Mekanika*, 33:212–222, 1969.

[37] N. M. Pugno and R. S. Ruoff. Quantized fracture mechanics. *Philosophical Magazine*, 84(27):2829–2845, 2004.

[38] D. Taylor. *The Theory of Critical Distances*. Elsevier, 2007.

[39] D. Leguillon. Strength or toughness? A criterion for crack onset at a notch. *European Journal of Mechanics - A/Solids*, 21(1):61–72, 2002.

[40] P. Cornetti, N. Pugno, A. Carpinteri, and D. Taylor. Finite fracture mechanics: A coupled stress and energy failure criterion. *Engineering Fracture Mechanics*, 73(14):2021–2033, 2006.

[41] P. Weißgraeber, D. Leguillon, and W. Becker. A review of Finite Fracture Mechanics: crack initiation at singular and non-singular stress raisers. *Archive of Applied Mechanics*, 86(1–2):375–401, 2016.

[42] G. R. Johnson and W. H. Cook. Fracture characteristics of three metals subjected to various strains, strain rates, temperatures and pressures. *Engineering Fracture Mechanics*, 21(1):31–48, 1985.

[43] Y. V. Petrov and N. F. Morozov. On the modeling of fracture of brittle solids. *Journal of Applied Mechanics*, 61(3):710–712, 1994.

[44] T. Yin, A. Tyas, O. Plekhov, A. Terekhina, and L. Susmel. A novel reformulation of the Theory of Critical Distances to design notched metals against dynamic loading. *Materials & Design*, 69:197–212, 2015.

[45] L. Ambrosio and V. M. Tortorelli. Approximation of functional depending on jumps by elliptic functional via t-convergence. *Communications on Pure and Applied Mathematics*, 43(8):999–1036, 1990.

[46] B. Bourdin, G. A. Francfort, and J.-J. Marigo. The variational approach to fracture. *Journal of Elasticity*, 91(1-3):5–148, 2008.

[47] C. Miehe, F. Welschinger, and M. Hofacker. Thermodynamically consistent phase-field models of fracture: Variational principles and multi-field FE implementations. *International Journal for Numerical Methods in Engineering*, 83(10):1273–1311, 2010.

[48] Y. Navidtehrani, C. Betegón, and E. Martínez-Pañeda. A simple and robust abaqus implementation of the phase field fracture method. *Applications in Engineering Science*, 6:100050, 2021.

[49] H. Amor, J.-J. Marigo, and C. Maurini. Regularized formulation of the variational brittle fracture with unilateral contact: Numerical experiments. *Journal of the Mechanics and Physics of Solids*, 57(8):1209–1229, 2009.

[50] G. Lancioni and G. Royer-Carfagni. The variational approach to fracture mechanics. A practical application to the French panthéon in Paris. *Journal of Elasticity*, 95(1-2):1–30, 2009.

[51] F. Freddi and G. Royer-Carfagni. Regularized variational theories of fracture: A unified approach. *Journal of the Mechanics and Physics of Solids*, 58(8):1154–1174, 2010.

[52] L. De Lorenzis and C. Maurini. Nucleation under multi-axial loading in variational phase-field models of brittle fracture. *International Journal of Fracture*, 237:61–81, 2022.

[53] R. Cavuoto, P. Lenarda, D. Misseroni, M. Paggi, and D. Bigoni. Failure through crack propagation in components with holes and notches: An experimental assessment of the phase field model. *International Journal of Solids and Structures*, 257:111798, 2022.

[54] J. Reinoso, A. Arteiro, M. Paggi, and P. P. Camanho. Strength prediction of notched thin ply laminates using finite fracture mechanics and the phase field approach. *Composites Science and Technology*, 150:205–216, 2017.

[55] F. Vicentini, P. Carrara, and L. De Lorenzis. Phase-field modeling of brittle fracture in heterogeneous bars. *European Journal of Mechanics - A/Solids*, 97:104826, 2023.

[56] C. Miehe, M. Hofacker, L.-M. Schänzel, and F. Aldakheel. Phase field modeling of fracture in multi-physics problems. Part II. Coupled brittle-to-ductile failure criteria and crack propagation in thermo-elastic–plastic solids. *Computer Methods in Applied Mechanics and Engineering*, 294:486–522, 2015.

[57] E. Martínez-Pañeda, A. Golahmar, and C. F. Niordson. A phase field formulation for hydrogen assisted cracking. *Computer Methods in Applied Mechanics and Engineering*, 342:742–761, 2018.

[58] C. Cui, R. Ma, and E. Martínez-Pañeda. Electro-chemo-mechanical phase field modeling of localized corrosion: theory and COMSOL implementation. *Engineering with Computers*, 39(6):3877–3894, 2023.

[59] M. Pundir, D. S. Kammer, and U. Angst. An FFT-based framework for predicting corrosion-driven damage in fractal porous media. *Journal of the Mechanics and Physics of Solids*, 179:105388, 2023.

[60] Z. Liu, J. Reinoso, and M. Paggi. Hygro-thermo-mechanical modeling of thin-walled photovoltaic laminates with polymeric interfaces. *Journal of the Mechanics and Physics of Solids*, 169:105056, 2022.

[61] M. Negri and C. Ortner. Quasi-static crack propagation by Griffith's criterion. *Mathematical Models and Methods in Applied Sciences*, 18(11):1895–1925, 2008.

[62] J. M. Sargado, E. Keilegavlen, I. Berre, and J. M. Nordbotten. High-accuracy phase-field models for brittle fracture based on a new family of degradation functions. *Journal of the Mechanics and Physics of Solids*, 111:458–489, 2018.

[63] J.-Y. Wu. A unified phase-field theory for the mechanics of damage and quasi-brittle failure. *Journal of the Mechanics and Physics of Solids*, 103:72–99, 2017.

[64] A. Kumar, B. Bourdin, G. A. Francfort, and O. Lopez-Pamies. Revisiting nucleation in the phase-field approach to brittle fracture. *Journal of the Mechanics and Physics of Solids*, 142:104027, 2020.

[65] D. Johnson, T. Maxfield, Y. Jin, and R. Fedkiw. Software-based automatic differentiation is flawed.

[66] A. Chambolle, S. Conti, and G. A. Francfort. Approximation of a brittle fracture energy with a constraint of non-interpenetration. *Archive for Rational Mechanics and Analysis*, 228(3):867–889, 2018.

[67] G. Del Piero and D. R. Owen. Structured deformations of continua. *Archive for Rational Mechanics and Analysis*, 124(2):99–155, 1993.

[68] E. Sacco. Modellazione e calcolo di strutture in materiale non resistente a trazione. *Atti della Accademia Nazionale dei Lincei. Classe di Scienze Fisiche, Matematiche e Naturali. Rendiconti Lincei. Matematica e Applicazioni, Serie 9*, 1(3):235–258, 1990.

[69] H. Tada, P. C. Paris, and G. R. Irwin. *The Stress Analysis of Cracks Handbook, Third Edition*. ASME Press, 2000.

[70] A. Sapora and P. Cornetti. Crack onset and propagation stability from a circular hole under biaxial loading. *International Journal of Fracture*, 214(1):97–104, 2018.

[71] G. Kirsch. Die theorie der elastizität und die bedürfnisse der festigkeitslehre. *Zeitshrift des Vereines deutscher Ingenieure*, 42:797–807, 1898.

[72] M. S. Alnæs, A. Logg, K. B. Ølgaard, M. E. Rognes, and G. N. Wells. Unified Form Language: A domain-specific language for weak formulations of partial differential equations. *ACM Transactions on Mathematical Software*, 40(2), 2014.

[73] M. S. Alnæs, J. Blechta, J. Hake, A. Johansson, B. Kehlet, A. Logg, C. Richardson, J. Ring, M. E. Rognes, and G. N Wells. The FEniCS Project Version 1.5. *Archive of Numerical Software*, 3, 2015.

[74] M. W. Scroggs, J. S. Dokken, C. N. Richardson, and G. N. Wells. Construction of arbitrary order finite element degree-of-freedom maps on polygonal and polyhedral cell meshes. *ACM Transactions on Mathematical Software*, 48(2), 2022.

[75] M. W. Scroggs, I. A. Baratta, C. N. Richardson, and G. N. Wells. Basix: a runtime finite element basis evaluation library. *Journal of Open Source Software*, 7(73):3982, 2022.

[76] I. A. Baratta, J. P. Dean, J. S. Dokken, M. Habera, J. S. Hale, C. N. Richardson, M. E. Rognes, M. W. Scroggs, N. Sime, and G. N. Wells. DOLFINx: The next generation FEniCS problem solving environment, 2023.

[77] P. Cornetti and A. Sapora. Penny-shaped cracks by Finite Fracture Mechanics. *International Journal of Fracture*, 219:153–159, 2019.

[78] P. C. Paris. The mechanics of fracture propagation and solutions to fracture arrester problem. *Document D2-2195*, 1957.

[79] A. Chao Correas, M. Corrado, A. Sapora, and P. Cornetti. Size-effect on the apparent tensile strength of brittle materials with spherical cavities. *Theoretical and Applied Fracture Mechanics*, 116:103120, 2021.

[80] A. Chao Correas, A. Sapora, J. Reinoso, M. Corrado, and P. Cornetti. Coupled versus energetic nonlocal failure criteria: A case study on the crack onset from circular holes under biaxial loadings. *European Journal of Mechanics - A/Solids*, 101:105037, 2023.

[81] R. E. Ely. Strength of titania and aluminum silicate under combined stresses. *Journal of the American Ceramic Society*, 55(7):347–350, 1972.

[82] S. Sato, H. Awaji, K. Kawamata, A. Kurumada, and T. Oku. Fracture criteria of reactor graphite under multiaxial stesses. *Nuclear Engineering and Design*, 103(3):291–300, 1987.

[83] M. J. Borden, C. V. Verhoosel, M. A. Scott, T. J. R. Hughes, and C. M. Landis. A phase-field description of dynamic brittle fracture. *Computer Methods in Applied Mechanics and Engineering*, 217-220:77–95, 2012.

[84] M. Hofacker and C. Miehe. A phase field model of dynamic fracture: Robust field updates for the analysis of complex crack patterns. *International Journal for Numerical Methods in Engineering*, 93(3):276–301, 2013.

[85] A. Schlüter, A. Willenbücher, C. Kuhn, and R. Müller. Phase field approximation of dynamic brittle fracture. *Computational Mechanics*, 54(5):1141–1161, 2014.

[86] T. Y. Li, J.-J. Marigo, D. Guilbaud, and S. Potapov. Variational approach to dynamic brittle fracture via gradient damage models. *Applied Mechanics and Materials*, 784:334–341, 2015.

[87] R. J. M. Geelen, Y. Liu, T. Hu, M. R. Tupek, and J. E. Dolbow. A phase-field formulation for dynamic cohesive fracture. *Computer Methods in Applied Mechanics and Engineering*, 348:680–711, 2019.

[88] J. F. Kalthoff and S. Winkler. Failure mode transition at high rates of shear loading, 1987.

[89] P. K. Kristensen, C. F. Niordson, and E. Martínez-Pañeda. Applications of phase field fracture in modelling hydrogen assisted failures. *Theoretical and Applied Fracture Mechanics*, 110:102837, 2020.

[90] M. Corrado, M. Paggi, and J. Reinoso. Dynamic formulation of phase field fracture in heterogeneous media with finite thickness cohesive interfaces. *Computational Materials Science*, 205:111226, 2022.

[91] N. M. Newmark. A method of computation for structural dynamics. *Journal of the Engineering Mechanics Division*, 85(3):67–94, 1959.

[92] R. Courant, K. Friedrichs, and H. Lewy. Über die partiellen Differenzengleichungen der mathematischen Physik. *Mathematische Annalen*, 100:32–74, 1928.

[93] S. Duczek and H. Gravenkamp. Mass lumping techniques in the spectral element method: On the equivalence of the row-sum, nodal quadrature, and diagonal scaling methods. *Computer Methods in Applied Mechanics and Engineering*, 353:516–569, 2019.

[94] A. Carpinteri. *Interpretation of the Griffith Instability as a Bifurcation of the Global Equilibrium*, page 287–316. Springer Netherlands, 1985.

[95] A. Carpinteri and I. Monetto. Snap-back analysis of fracture evolution in multi-cracked solids using boundary element method. *International Journal of Fracture*, 98(3/4):225–241, 1999.

[96] L. Biolzi and J. F. Labuz. Global instability and bifurcation in beams composed of rock-like materials. *International Journal of Solids and Structures*, 30(3):359–370, 1993.

[97] A. Carpinteri. Cusp catastrophe interpretation of fracture instability. *Journal of the Mechanics and Physics of Solids*, 37(5):567–582, 1989.

[98] F. Barpi and S. Valente. Size-effects induced bifurcation phenomena during multiple cohesive crack propagation. *International Journal of Solids and Structures*, 35(16):1851–1861, 1998.

[99] P. Cornetti, M. Corrado, L. De Lorenzis, and A. Carpinteri. An analytical cohesive crack modeling approach to the edge debonding failure of FRP-plated beams. *International Journal of Solids and Structures*, 53:92–106, 2015.

[100] E. Riks. The application of newton's method to the problem of elastic stability. *Journal of Applied Mechanics*, 39(4):1060–1065, 1972.

[101] M. A. Crisfield. A fast incremental/iterative solution procedure that handles "snap-through". In A. K. Noor and H. G. McComb, editors, *Computational Methods in Nonlinear Structural and Solid Mechanics*, pages 55–62. Pergamon, 1981.

[102] F. Zhou. *Study on the macroscopic behavior and the microscopic process of dynamic crack propagation*. PhD thesis, The University of Tokyo, 1996.

[103] G. Albertini, M. Lebihain, F. Hild, L. Ponson, and D. S. Kammer. Effective toughness of heterogeneous materials with rate-dependent fracture energy. *Physical Review Letters*, 127:035501, 2021.

[104] E. Marin, F. Boschetto, M. Zanocco, H. N. Doan, T. P. M. Sunthar, K. Kinashi, D. Iba, W. Zhu, and G. Pezzotti. UV-curing and thermal ageing of methacrylated stereo-lithographic resin. *Polymer Degradation and Stability*, 185:109503, 2021.

[105] F. J. Gómez, G. V. Guinea, and M. Elices. Failure criteria for linear elastic materials with U-notches. *International Journal of Fracture*, 141(1–2):99–113, 2006.

[106] M. Creager and P. C. Paris. Elastic field equations for blunt cracks with reference to stress corrosion cracking. *International Journal of Fracture Mechanics*, 3(4):247–252, 1967.

[107] A. Parvizi, K. W. Garrett, and J. E. Bailey. Constrained cracking in glass fibre-reinforced epoxy cross-ply laminates. *Journal of Materials Science*, 13(1):195–201, 1978.

[108] A. Sapora, F. Ferrian, P. Cornetti, H. Talebi, and M. R. Ayatollahi. Ligament size effect in largely cracked tensile structures. *Theoretical and Applied Fracture Mechanics*, 125:103871, 2023.

[109] A. Carpinteri, P. Cornetti, N. Pugno, A. Sapora, and D. Taylor. A finite fracture mechanics approach to structures with sharp V-notches. *Engineering Fracture Mechanics*, 75(7):1736–1752, 2008.

[110] I. G. García and D. Leguillon. Mixed-mode crack initiation at a V-notch in presence of an adhesive joint. *International Journal of Solids and Structures*, 49(15):2138–2149, 2012.

[111] A. Doitrand, R. Estevez, and D. Leguillon. Comparison between cohesive zone and coupled criterion modeling of crack initiation in rhombus hole specimens under quasi-static compression. *Theoretical and Applied Fracture Mechanics*, 99:51–59, 2019.

[112] A. Doitrand, P. Cornetti, A. Sapora, and R. Estevez. Experimental and theoretical characterization of mixed mode brittle failure from square holes. *International Journal of Fracture*, 228(1):33–43, 2021.

[113] E. Martin, D. Leguillon, and N. Carrère. A coupled strength and toughness criterion for the prediction of the open hole tensile strength of a composite plate. *International Journal of Solids and Structures*, 49(26):3915–3922, 2012.

[114] P. L. Rosendahl, P. Weißgraeber, N. Stein, and W. Becker. Asymmetric crack onset at open-holes under tensile and in-plane bending loading. *International Journal of Solids and Structures*, 113-114:10–23, 2017.

[115] A. Sapora, A. R. Torabi, S. Etesam, and P. Cornetti. Finite fracture mechanics crack initiation from a circular hole. *Fatigue & Fracture of Engineering Materials & Structures*, 41(7):1627–1636, 2018.

[116] A. Sapora and D. Firrao. Finite fracture mechanics predictions on the apparent fracture toughness of as-quenched Charpy V-type AISI 4340 steel specimens. *Fatigue & Fracture of Engineering Materials & Structures*, 40(6):949–958, 2017.

[117] P. Weissgraeber, J. Felger, D. Geipel, and W. Becker. Cracks at elliptical holes: Stress intensity factor and finite fracture mechanics solution. *European Journal of Mechanics - A/Solids*, 55:192–198, 2016.

[118] P. Cornetti, V. Mantič, and A. Carpinteri. Finite fracture mechanics at elastic interfaces. *International Journal of Solids and Structures*, 49(7):1022–1032, 2012.

[119] M. Muñoz-Reja, L. Távara, V. Mantič, and P. Cornetti. Crack onset and propagation at fibre–matrix elastic interfaces under biaxial loading using finite fracture mechanics. *Composites Part A: Applied Science and Manufacturing*, 82:267–278, 2016.

[120] J. Andersons, S. Tarasovs, and E. Spārniņš. Finite fracture mechanics analysis of crack onset at a stress concentration in a UD glass/epoxy composite in off-axis tension. *Composites Science and Technology*, 70(9):1380–1385, 2010.

[121] P. P. Camanho, G. H. Erçin, G. Catalanotti, S. Mahdi, and P. Linde. A finite fracture mechanics model for the prediction of the open-hole strength of composite laminates. *Composites Part A: Applied Science and Manufacturing*, 43(8):1219–1225, 2012.

[122] I. G. García, V. Mantič, and A. Blázquez. The effect of residual thermal stresses on transverse cracking in cross-ply laminates: an application of the coupled criterion of the finite fracture mechanics. *International Journal of Fracture*, 211(1–2):61–74, 2018.

[123] M. Baldassari, A. Monaco, A. Sapora, and P. Cornetti. Size effect on flexural strength of notched and un-notched concrete and rock specimens by Finite Fracture Mechanics. *Theoretical and Applied Fracture Mechanics*, 125:103787, 2023.

[124] P. L. Rosendahl, Y. Staudt, A. P. Schneider, J. Schneider, and W. Becker. Nonlinear elastic finite fracture mechanics: Modeling mixed-mode crack nucleation in structural glazing silicone sealants. *Materials & Design*, 182:108057, 2019.

[125] F. Ferrian, P. Cornetti, L. Marsavina, and A. Sapora. Finite Fracture Mechanics and Cohesive Crack Model: Size effects through a unified formulation. *Frattura ed Integrità Strutturale*, 16(61):496–509, 2022.

[126] G. Molnár, A. Doitrand, R. Estevez, and A. Gravouil. Toughness or strength? Regularization in phase-field fracture explained by the coupled criterion. *Theoretical and Applied Fracture Mechanics*, 109:102736, 2020.

[127] S. Timoshenko and J. Goodier. *Theory of Elasticity*. McGraw-Hill, 1951.

[128] T. Fett. Stress intensity factors and weight function for a void with an annular crack. *International Journal of Fracture*, 67(2):R41–R47, 1994.

[129] P. Cornetti, A. Sapora, and A. Carpinteri. Short cracks and V-notches: Finite Fracture Mechanics vs. Cohesive Crack Model. *Engineering Fracture Mechanics*, 168:2–12, 2016.

[130] R. L. Bertolotti and R. M. Fulrath. Effect of micromechanical stress cocentrations on strength of porous glass. *Journal of the American Ceramic Society*, 50(11):558–562, 1967.

[131] M. Barlet, J.-M. Delaye, T. Charpentier, M. Gennisson, D. Bonamy, T. Rouxel, and C. L. Rountree. Hardness and toughness of sodium borosilicate glasses via Vickers's indentations. *Journal of Non-Crystalline Solids*, 417-418:66–79, 2015.

[132] M. Kaji, S. Yoshiura, and M. Nishimura. Strength estimation for silicon nitride specimens with a spherical void. *Journal of Materials Science*, 29(22):5947–5952, 1994.

[133] M. Ippolito, A. Mattoni, N. M. Pugno, and L. Colombo. Failure strength of brittle materials containing nanovoids. *Phys. Rev. B*, 75:224110, 2007.

[134] V. Mantič. Interface crack onset at a circular cylindrical inclusion under a remote transverse tension. application of a coupled stress and energy criterion. *International Journal of Solids and Structures*, 46(6):1287–1304, 2009.

[135] A. Doitrand, G. Molnár, D. Leguillon, E. Martin, and N. Carrère. Dynamic crack initiation assessment with the coupled criterion. *European Journal of Mechanics - A/Solids*, 93:104483, 2022.

[136] X. Chen, A. Doitrand, N. Godin, and C. Fusco. Crack initiation in PMMA plates with circular holes considering kinetic energy and nonlinear elastic material behavior. *Theoretical and Applied Fracture Mechanics*, 124:103783, 2023.

[137] Y. V. Petrov, N. F. Morozov, and V. I. Smirnov. Structural macromechanics approach in dynamics of fracture. *Fatigue & Fracture of Engineering Materials & Structures*, 26(4):363–372, 2003.

[138] N. Alanazi and L. Susmel. Theory of Critical Distances and static/dynamic fracture behaviour of un-reinforced concrete: length scale parameters vs. material meso-structural features. *Engineering Fracture Mechanics*, 261:108220, 2022.

[139] V. Bratov and Y. Petrov. Application of incubation time approach to simulate dynamic crack propagation. *International Journal of Fracture*, 146(1–2):53–60, 2007.

[140] H. Homma, D. A. Shockey, and Y. Murayama. Response of cracks in structural materials to short pulse loads. *Journal of the Mechanics and Physics of Solids*, 31(3):261–279, 1983.

[141] Y. V. Petrov and E. V. Sitnikova. Dynamic cracking resistance of structural materials predicted from impact fracture of an aircraft alloy. *Technical Physics*, 49(1):57–60, 2004.

[142] N. M. Pugno. Dynamic quantized fracture mechanics. *International Journal of Fracture*, 140(1–4):159–168, 2006.

[143] L. B. Freund. *Dynamic Fracture Mechanics*. Cambridge Monographs on Mechanics. Cambridge University Press, 1990.

[144] B. Wu, R. Chen, and K. Xia. Dynamic tensile failure of rocks under static pre-tension. *International Journal of Rock Mechanics and Mining Sciences*, 80:12–18, 2015.

[145] W. Yao, K. Xia, and A. K. Jha. Experimental study of dynamic bending failure of Laurentian granite: loading rate and pre-load effects. *Canadian Geotechnical Journal*, 56(2):228–235, 2019.

[146] W. Yao, K. Xia, and T. Zhang. Dynamic fracture test of Laurentian granite subjected to hydrostatic pressure. *Experimental Mechanics*, 59(2):245–250, 2019.

[147] M. J. Iqbal and B. Mohanty. Experimental calibration of stress intensity factors of the ISRM suggested cracked chevron-notched brazilian disc specimen used for determination of mode-I fracture toughness. *International Journal of Rock Mechanics and Mining Sciences*, 43(8):1270–1276, 2006.

[148] R. Chen, K. Xia, F. Dai, F. Lu, and S. N. Luo. Determination of dynamic fracture parameters using a semi-circular bend technique in Split Hopkinson Pressure Bar testing. *Engineering Fracture Mechanics*, 76(9):1268–1276, 2009.

[149] M. H. B. Nasseri and B. Mohanty. Fracture toughness anisotropy in granitic rocks. *International Journal of Rock Mechanics and Mining Sciences*, 45(2):167–193, 2008.

[150] D. J. Frew, M. J. Forrestal, and W. Chen. Pulse shaping techniques for testing brittle materials with a Split Hopkinson Pressure Bar. *Experimental Mechanics*, 42(1):93–106, 2002.

[151] F. Dai, K. Xia, and S. N. Luo. Semicircular bend testing with Split Hopkinson Pressure Bar for measuring dynamic tensile strength of brittle solids. *Review of Scientific Instruments*, 79(12):123903, 2008.

[152] F. Dai, R. Chen, and K. Xia. A semi-circular bend technique for determining dynamic fracture toughness. *Experimental Mechanics*, 50(6):783–791, 2010.

[153] A. R. Torabi, S. Etesam, A. Sapora, and P. Cornetti. Size effects on brittle fracture of brazilian disk samples containing a circular hole. *Engineering Fracture Mechanics*, 186:496–503, 2017.

[154] A. Doitrand and A. Sapora. Nonlinear implementation of Finite Fracture Mechanics: A case study on notched brazilian disk samples. *International Journal of Non-Linear Mechanics*, 119:103245, 2020.

[155] S. Ghouli, B. Bahrami, M. R. Ayatollahi, T. Driesner, and M. Nejati. Introduction of a scaling factor for fracture toughness measurement of rocks using the semi-circular bend test. *Rock Mechanics and Rock Engineering*, 54(8):4041–4058, 2021.

[156] M. Sangsefidi, J. Akbardoost, and A. R. Zhaleh. Assessment of mode I fracture of rock-type sharp V-notched samples considering the size effect. *Theoretical and Applied Fracture Mechanics*, 116:103136, 2021.

[157] Y. Navidtehrani, C. Betegón, R. W. Zimmerman, and E. Martínez-Pañeda. Griffith-based analysis of crack initiation location in a brazilian test. *International Journal of Rock Mechanics and Mining Sciences*, 159:105227, 2022.

[158] C. Maurini, A. Chao Correas, S. Jimenez-Alfaro, G. Blondet, L. De Lorenzis, V. Lazarus, and A. Latyshev. Computational fracture mechanics examples with FEniCSx, 2024. H2020-MSCA-ITN 861061-NEWFRAC.

[159] G. Bradski. The OpenCV Library. *Dr. Dobb's Journal of Software Tools*, 2000.

[160] Formlabs. *Clear Resin Technical Data Sheet*, August 2023. Rev. 2.

Appendix A

Resolution kernels for the quasi-static and dynamic Phase Field fracture models

This appendix contains the algorithms for the resolution kernels of the two main variants of the Phase Field fracture model used, namely the quasi-static (Algorithm 1) and dynamic (Algorithm 2) approaches. These follow a notation coherent with the rest of chapters, and so the fields in italic denote mathematical forms, i.e. expressions that have not been discretized in the Finite Element context. On the other hand, magnitudes in Sans Serif indicate already discretized fields, of which matrices and vectors are represented by uppercase and lowercase letters, respectively. In any case, it is to be noted that the different mathematical forms must be discretized for their Finite Element implementation, yet the form notation has been retained wherever possible for it is more generic.

Regarding the actual numerical implementation of the algorithms using FeniCSx, some relevant minimum working examples for the Phase Field fracture models can be found in NEWFRAC's specific repository [158], to which the Author of this thesis has contributed extensively.

Algorithm 1 Resolution kernel for the quasi-static Phase Field fracture model using a staggered approach and an Alternate Minimization scheme

Initialize $\{t, \Delta t, i, N_{\text{fails}}, \underline{u}_0, \alpha_0\} \leftarrow \{t_0, \Delta t_0, 1, 0, \underline{u}_{t_0}, \alpha_{t_0}\}$
while $t_i \leq T$ and $N_{\text{fails}} \leq N_{\text{fails\_max}}$ **do**
  update Dirichlet BCs on $\underline{u}$ and α to t_i
  set $\{j, \text{converged}, \underline{u}_{i0}, \alpha_{i0}\} \leftarrow \{0, \text{False}, \underline{u}_{i-1}, \alpha_{i-1}\}$
  while $j \leq N_{\text{iter\_max}}$ and converged is False **do**
    update $j \leftarrow j+1$
    solve for $\underline{u}_{ij}$ with $\alpha = \alpha_{ij-1}$ fixed
    solve for α_{ij} with $\underline{u} = \underline{u}_{ij}$ fixed
    assess converged for $\left(\underline{u}_{ij}, \alpha_{ij}\right)$
  end while
  if converged is True **then**
    assign $\{\underline{u}_i, \alpha_i\} \leftarrow \{\underline{u}_{ij}, \alpha_{ij}\}$
    determine Δt
    perform postprocessing
    update $t_{i+1} \leftarrow t_i + \Delta t$
    update $i \leftarrow i+1$
    set $N_{\text{fails}} \leftarrow 0$
  else
    set $t_i \leftarrow \tau$ with $\tau \in (t_{i-1}, t_i)$
    update $N_{\text{fails}} \leftarrow N_{\text{fails}} + 1$
  end if
end while

Algorithm 2 Resolution kernel for the dynamic Phase Field fracture model problem using a staggered approach and an explicit Newmark's β-method time integrator

Initialize $\{t,\, i,\, \underline{u}_0,\, \underline{\dot{u}}_0,\, \underline{\ddot{u}}_0,\, \alpha_0\} \leftarrow \{t_0,\, 1,\, \underline{u}_{t_0},\, \underline{\dot{u}}_{t_0},\, \underline{\ddot{u}}_{t_0},\, \alpha_{t_0}\}$
determine Δt according to Courant–Friedrichs–Lewy condition
compute the consistent mass matrix M
compute the lumped mass matrix: $\mathsf{M_L} \leftarrow (\mathsf{M}\,\mathsf{1})\,\mathsf{I}$
while $t_{i+1} \leq T$ **do**
  update BCs on $\underline{u}$, $\underline{\dot{u}}$, $\underline{\ddot{u}}$ and α to t_{i+1}
  propagate $\underline{u}$ to t_{i+1}: $\underline{u}_{i+1} \leftarrow \underline{u}_i + \Delta t\, \underline{\dot{u}}_i + \Delta t^2\, \underline{\ddot{u}}_i/2$
  impose restricted DoFs of $\underline{u}_{i+1}$ per the Dirichlet BCs on $\underline{u}$ at t_{i+1}
  solve for α_{i+1} with $\underline{u} = \underline{u}_{i+1}$ fixed
  compute the motion stiffness matrix $\mathsf{K_u}(\alpha_{i+1})$
  compute the vector of nodal forces $\mathsf{F}_{i+1} \leftarrow -\mathsf{K_u}(\alpha_{i+1})\mathsf{d}_{i+1}$
  propagate $\underline{\ddot{u}}$ to t_{i+1}: $\mathsf{a}_{i+1} \leftarrow \mathsf{M_L^{-1}}\mathsf{F_{i+1}}$
  correct restricted DoFs of $\underline{\ddot{u}}_{i+1}$ per the Dirichlet BCs on $\underline{\ddot{u}}$ at t_{i+1}
  propagate $\underline{\dot{u}}$ to t_{i+1}: $\underline{\dot{u}}_{i+1} \leftarrow \underline{\dot{u}}_i + \Delta t(\underline{\ddot{u}}_{i+1} + \underline{\ddot{u}}_i)/2$
  correct restricted DoFs of $\underline{\dot{u}}_{i+1}$ per the Dirichlet BCs on $\underline{\dot{u}}$ at t_{i+1}
  update $t_{i+1} \leftarrow t_i + \Delta t$
  update $i \leftarrow i + 1$
end while

Appendix B

The Virtual Extensometer: an effective optical technique for *in situ* measuring specimen elongations

This appendix describes the Virtual Extensometer (VE) technique used in Chapter 4 to measure specimen elongations *in situ*. In particular, this is a digital-optical tool that exploits well-established object recognition techniques to track the position of two differently coloured markers within the plane of measure. Since each marker moves in unison with one end of the gauge region throughout the test, their relative displacements provide a reliable measure over time of the specimen's elongation. Therefore, this technique mimics a conventional extensometer while not requiring any physical contact with the specimen, since the sampling points are optically tracked. This characteristic renders it particularly beneficial for testing setups in which the space surrounding the specimen is limited (see e.g. Fig. 4.2). Furthermore, compared to other conventional *in situ* measuring techniques, the VE proves more cost effective than strain gauges and requires less pre- and post-processing than the also optical Digital Image Correlation techniques. Moreover, the VE can also be easily upscaled to yield multiple measures by increasing the number of optical markers, although this appendix will focus on the use of just two markers placed along the specimen's length. In what follows, the VE working principles will be thoroughly described, including an overview of the colour-based object recognition technique on which it relies and a discussion on some technical aspects of its implementation, concluding the appendix with a quantitative validation of the methodology.

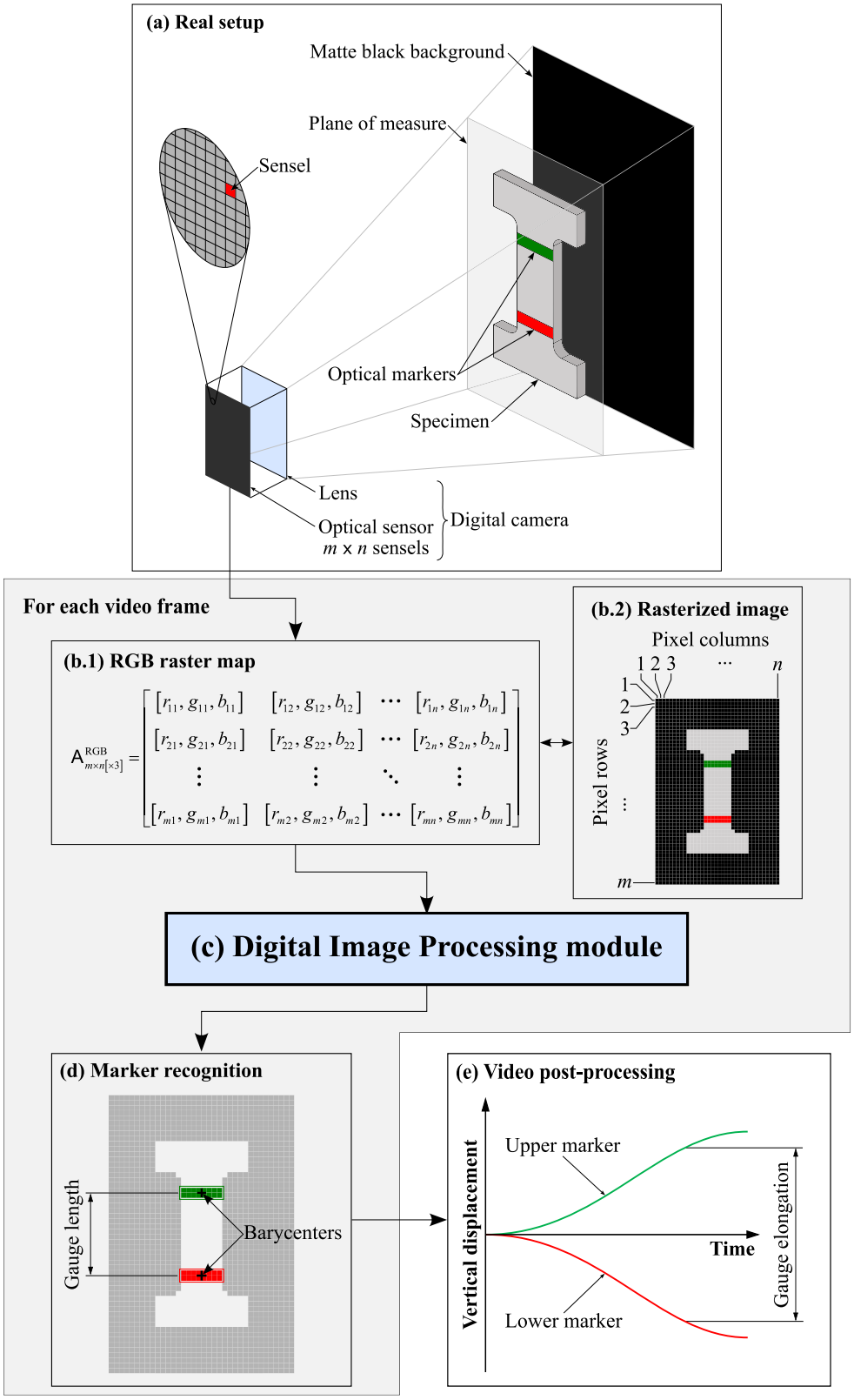

Fig. B.1 Illustration of the Virtual Extensometer's logical flowchart.

The logical flowchart behind the VE's measure of the specimen elongation over time is illustrated in Fig. B.1. Given that this particular optical approach relies on the recognition of coloured markers, the actual test is conducted under bright indirect lighting and against a matte black background to minimize unwanted reflections and distortions. Similar to other digital-image-based measuring techniques, the evolution of the specimen over time is video-recorded within the plane of measure. This is done with a digital camera, which besides the lens set and other accessory components, essentially comprises an optical sensor with an array of $m \times n$ sensels. Each of these electro-optical components is able to encode the characteristics of the incident light in a triad of discrete numerical values, mostly often corresponding to the intensity of the three primary additive colours, i.e. Red, Green and Blue (RGB). At every instant in which the sensor is sampled[1], the RGB triplets determined by each of the sensels are assembled into an array $\mathsf{A}^{\mathrm{RGB}}$ of dimensions $m \times n\,[\times 3]$, the so-called raster map, which numerically encodes the tessellated sampling of the scene as projected onto the sensor[2]. When recording a digital video, this sampling and encoding process is performed at each time frame, hence generating a sequence in time of raster maps. As such, a digital video essentially discretizes in space, colour and time a planar projection of the recorded scene, encoding this information in a sequence of arrays of digits. This discretization is then exploited by the VE's digital image processing module, which takes $\mathsf{A}^{\mathrm{RGB}}$ as an input, identifies the optical markers through digital image processing, and outputs the corresponding barycentre positions. In particular, this core module was implemented on Python using the open source computer vision library OpenCV [159].

Therefore, the VE's cornerstone lies in the digital image processing module that enables the recognition of which pixels within $\mathsf{A}^{\mathrm{RGB}}$ correspond to one of the two optical markers. Ideally, each marker would showcase a perfectly uniform colour[3] that is unique in the recorded scene, so that only the pixels belonging to a specific marker would display the corresponding RGB triplets. Nonetheless, this procedure

[1] Please notice that many commercially available sensors feature a *rolling shutter*, which does not read all sensels simultaneously but quickly scans across them. While their use is admissible for scenes with slowly-moving objects such as the one here at hand, a *global shutter* is required for applications with fast-moving objects.

[2] Raster maps decode into rasterized images, which are a "mosaic" of $m \times n$ "tiles" (or pixels) in which the colour of the ij-th pixel is dictated by the RGB triplet stored in the ij-th component of $\mathsf{A}^{\mathrm{RGB}}$.

[3] The term colour refers to the visual perception of electromagnetic radiation, which can be broken down into different perceived properties such as hue, saturation, and brightness.

proves too rigid for real-life images, since even apparently homogeneous colouring is hardly ever so, as it can be seen when analysing Fig. B.2a in detail. As such, a robust marker recognition procedure involves comparing pixels against a range of colours that can be attributed to the markers, allowing it to tolerate moderate lighting inhomogeneities and slight colour shifts, among other distortions occurring when video-recording actual experiments. However, defining these sought after colour subspaces in RGB coordinates is challenging because any change in each of the three intensity channels simultaneously affects the hue, saturation, and brightness of the colours (see Figs. B.2b to B.2d).

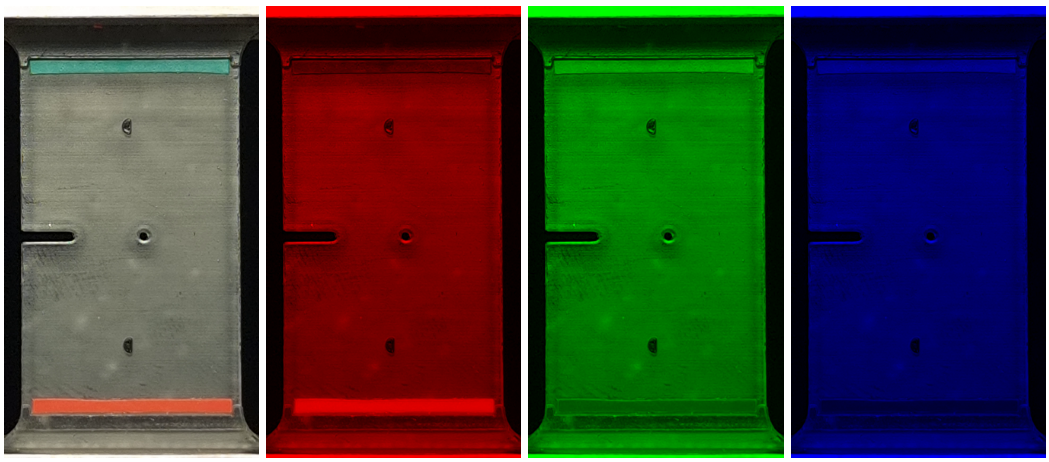

(a) (b) (c) (d)

Fig. B.2 Graphical representation of: (a) the rasterized image of a real-life experiment with the optical markers; and the corresponding (b) red, (c) green, and (d) blue intensity channels.

In fact, the conventional 24-bit RGB colour space (8-bits per pixel and channel) can be graphically depicted as a three-dimensional Cartesian-like space in Fig. B.3a, with the three orthogonal axes representing the pure red, green, and blue intensity channels. Thus, the greyscale lies along the cube diagonal from $[0, 0, 0]$ (black) to $[255, 255, 255]$ (white), while fully-saturated colours are located on the cube edges that do not intersect with this diagonal. Hence, the saturation of a colour in the RGB space is in some sense determined by how close it is to the greyscale diagonal, the brightness results from how close a colour is to white, and the hue mainly changes as the colour revolves around the greyscale diagonal. Taking this into consideration, the tridimensional colour space can be instead defined as a cylindrical-like coordinate system in which the hoop, radial and height coordinates determine the hue, saturation and brightness channels, respectively. In this way, apparent

colour shifts due to lighting inhomogeneities or reflections would primarily affect the saturation and brightness channels, while the hue channel would expectedly remain unaffected. Therefore, the recognition of optical markers under real-life conditions is considerably facilitated. Various colour spaces that meet these characteristics are widespread available, such as Hue-Saturation-Value (HSV) or Hue-Saturation-Lightness (HSL), with the former being the one here used. Provided the 24-bit pixel encoding, both the saturation and brightness channels take integer values in the range $[0, 255]$. On the other hand, the hue channel often takes integer values corresponding to the polar angle in degrees, and so defined within the range $[0, 360]$ in principle. Nonetheless, such a range exceeds the 256 integers achievable by 8-bits encoding, so that some libraries (such as OpenCV) actually half such range to $[0, 179]$, as illustrated in Fig. B.3b. Still, OpenCV allows hue values over 179 (and up to 255) by treating them as if they were subtracted by 180, and so the hue value of 180 in Fig. B.3b is actually equivalent to a hue of 0.

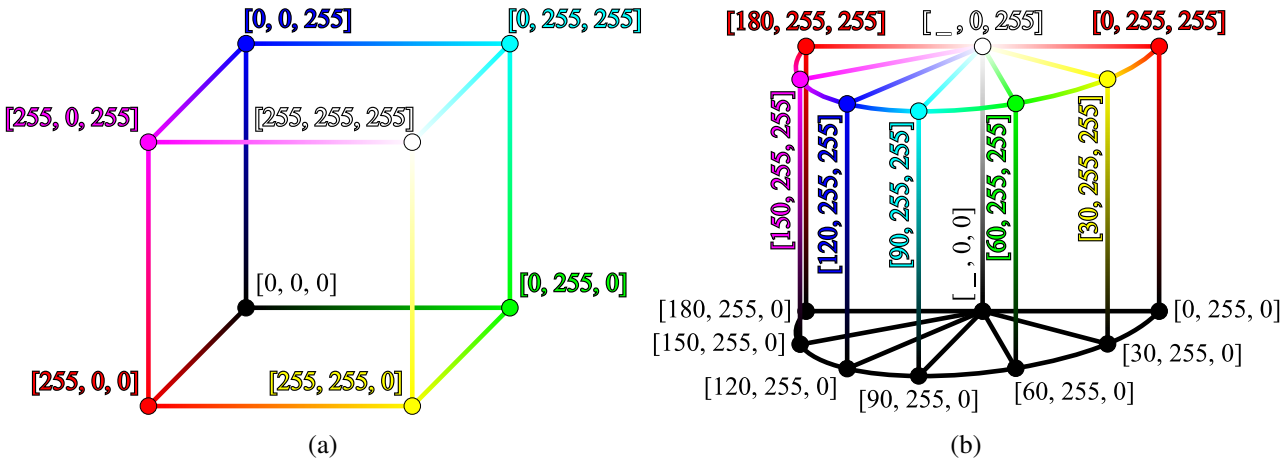

Fig. B.3 Illustration of the (a) Red-Green-Blue and (b) Hue-Saturation-Value colour spaces using 24-bit encoding per pixel.

The advantages of using the HSV colour space for marker recognition become evident after examining Fig. B.4, which separately illustrates the hue, saturation, and brightness channels corresponding to the rasterized image in Fig. B.2a. In these figures, it can be observed that only the pixels corresponding to the markers display relatively high values of both saturation and brightness. Likewise, a detailed analysis of Fig. B.4a reveals that the green-ish and red-ish coloured markers present quasi-homogeneous hue values approximately equal to 82 (green/teal hue) and 6 (red

hue), respectively. Therefore, the green-ish (red-ish) marker can be easily recognized by searching for pixels with an HSV triplet that has a hue channel close to 82 (6) and displays sufficiently high values of both saturation and brightness. Thereafter, the condition of each pixel concerning their belonging to a marker is stored in an array $\mathsf{A}^{\mathrm{Bool}}$ of $m \times n$ Boolean values a_{ij}^{Bool}, which is also referred to as a Boolean mask.

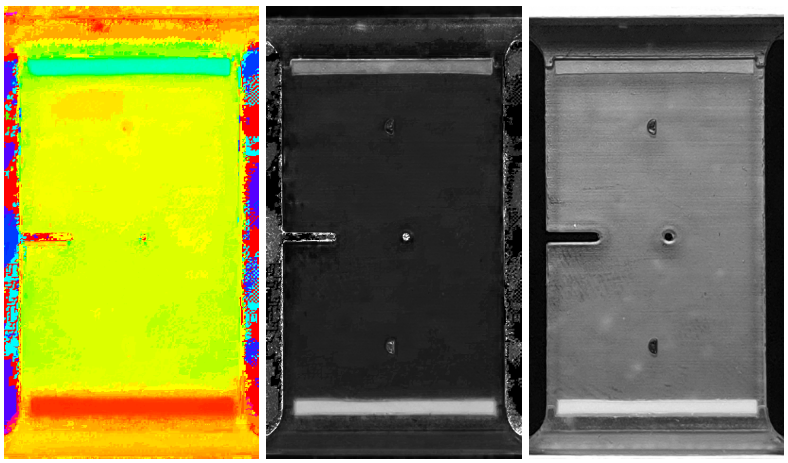

(a) (b) (c)

Fig. B.4 Separate graphical representation of (a) hue, (b) saturation, and (c) brightness channels of the rasterized image in Fig. B.2a after its conversion to the HSV colour space.

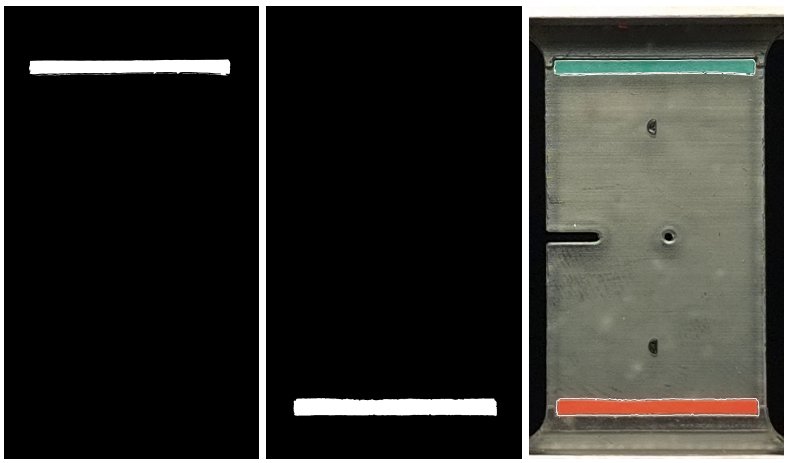

(a) (b) (c)

Fig. B.5 Graphical representation of: the Boolean masks corresponding to (a) the green-ish ($\mathsf{A}^{\mathrm{Bool}}|_{\mathrm{Green}}$), and (b) the red-ish ($\mathsf{A}^{\mathrm{Bool}}|_{\mathrm{Red}}$) markers from Fig. B.2a; and (c) superimposition of the recognized marker contours over the original image.

Using the image in Fig. B.2a as an example, there can be assumed that any pixel with an HSV triplet within $[55, 55, 100]$ and $[90, 255, 255]$ belongs to the greenish marker, while any pixel within $[0, 100, 100]$ and $[15, 255, 255]$ belongs to the reddish marker (see Fig. B.3b). In such a case, one obtains the two Boolean masks $\mathsf{A}^{\mathrm{Bool}}$ represented in Fig. B.5a and B.5b, where white (black) pixels represent True (False) values. Notice that, even though these HSV ranges are broader than strictly necessary, the approach proves robust enough to accurately identify the location of each of the two markers, as clearly shown in Fig. B.5c.

At this point, each of the obtained Boolean masks contains the spatial distribution of pixels that belong to the corresponding marker, so that leveraging the fact that each pixel represents an in-plane spatial element of constant size, one can determine the position of each marker's barycentre within the raster map $(i_c,\, j_c)$ as:

$$(i_c,\, j_c) = \frac{\sum_{i=1}^{m} \sum_{j=1}^{n} (i,\, j)\, a_{ij}^{\mathrm{Bool}}}{\sum_{i=1}^{m} \sum_{j=1}^{n} a_{ij}^{\mathrm{Bool}}}\,, \tag{B.1}$$

which is a reliable estimate of the marker position within the raster map for it relies on the aggregation of many individual measures. In fact, neither i_c nor j_c are integers any longer but quantized natural numbers, with their quanta being equal to $1/\sum_{i=1}^{m} \sum_{j=1}^{n} a_{ij}^{\mathrm{Bool}}$. Therefore, the larger the marker is in relation to the pixel size, the higher the resolution of the VE's barycentre measurements. For a digital video with N frames recorded at the instants $t = t_k \mid k \in [1, N]$, repeating this entire marker recognition process for every frame results in the discrete temporal sequence of the in-plane position of both marker barycentres, i.e. $(i_c,\, j_c)\,|_{\mathrm{Green},\, t_k}$ and $(i_c,\, j_c)\,|_{\mathrm{Red},\, t_k}$. After post-processing these sequences, one can then determine the discrete evolution over time of the in-plane distance d_{t_k} (in pixels) between the barycentres of the Green and Red optical markers as:

$$d_{\mathrm{px},t_k} = \sqrt{\left| (i_c,\, j_c)_{\mathrm{Green},\, t_k} - (i_c,\, j_c)_{\mathrm{Red},\, t_k} \right|^2}\,, \tag{B.2}$$

which can easily be used to determine the engineering strain of the gauge length at each sampled instant ε_{t_k} as:

$$\varepsilon_{t_k} = \frac{\Delta d_{\mathrm{px},t_k}}{d_{\mathrm{px},t_1}} = \frac{d_{\mathrm{px},t_k} - d_{\mathrm{px},t_1}}{d_{\mathrm{px},t_1}}\,. \tag{B.3}$$

Eventually, given that the initial gauge length in millimetres d_{mm,t_1} is known, the actual gauge elongation can be derived from the VE measurements as $\Delta d_{\mathrm{mm},t_k} = \varepsilon_{t_k} d_{\mathrm{mm},t_1}$.

B.1 Resolution, precision, accuracy and validation of the Virtual Extensometer technique

Once the VE's working principles have been thoroughly described, its quantitative representativeness is now to be empirically proven. To this end, a tensile test was performed on a plain 3D printed specimen with gauge dimensions $27 \times 16 \times 3.5$ mm while using the same polymeric resin, curing cycle, experimental setup, and testing conditions as those described in Chapter 4. To avoid the uncontrolled failure of the specimen, the tensile test was limited up to a $\sim 5\%$ gauge elongation since the resin manufacturer reports a post-curing failure strain of 6%. As previously mentioned, the load applied was measured by the machine's built-in 5 kN load cell, whereas the VE was used to determine the specimen's engineering longitudinal strain. In particular, the sampling frequencies for each of these magnitudes were 10 Hz for the former and 24 Hz for the latter. Likewise, the test was video-recorded on 4K resolution, meaning that each frame consisted on 3840×2160 pixels, resulting in an apparent pixel dimension within the plane of measure on the order of $10^{-2} \times 10^{-2}$ mm^2. At the same time, the optical markers had an area on the order of $10^{0} \times 10^{1}$ mm^2, hence meaning that $\mathscr{O}\left(10^{2} \times 10^{3}\right)$ pixels would belong to each marker. Overall, this results in a quantization of the barycentre positions of $\mathscr{O}\left(10^{-5}\right)$ pixels, or a VE's dimensional resolution on the order of 10^{-7} mm.

The measurements of the applied force and the marker position throughout the test are then synchronized and post-processed to determine the evolution over time of the engineering stress σ_t and strain ε_t, as reported in Fig. B.6a. Regarding the strain results, the minimal scatter shown in Fig. B.6a, wherein no filter has been used, indicates that the VE technique can produce measurements with relatively high precision. In particular for the cases at hand, the scatter in the strain measures was found to yield a measurement precision of $\mathscr{O}\left(10^{-4}\right)$, thus considerably higher than the aforementioned resolution. This, combined with the specimen's gauge length of 27 mm, involves a measuring precision in the specimen elongation on the order

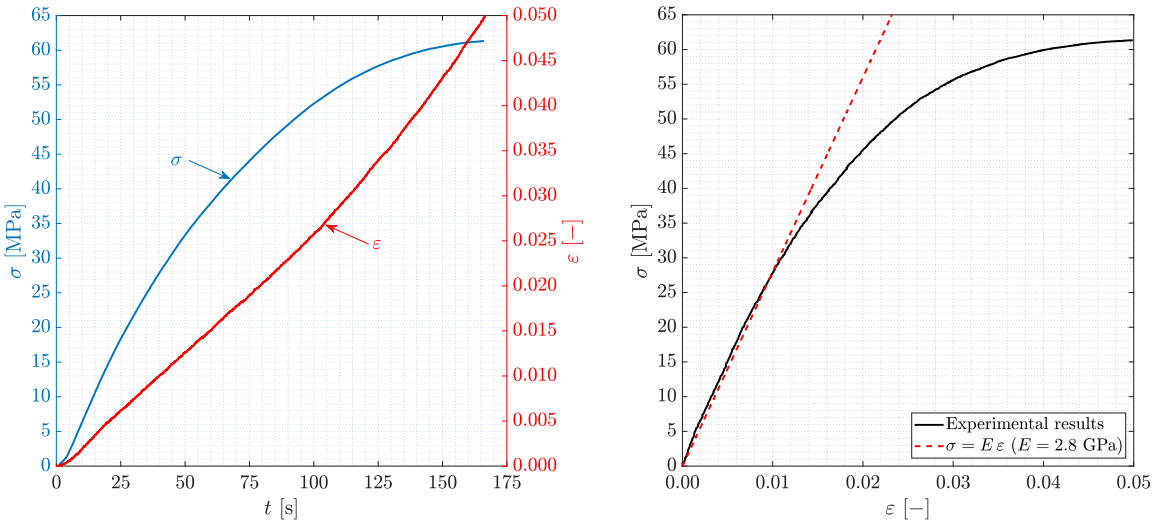

(a) (b)

Fig. B.6 For a single tensile test up to a 5% elongation: (a) evolution over time of the engineering stress and strain measurements; and (b) the resulting stress versus strain chart.

of 10^{-3} mm. Henceforth, the punctual values for σ_t and ε_t can be interpolated to a shared time discretization and plotted against each other as in Fig. B.6b. From this figure, it is evident that the force and elongation measurements align well with the post-curing "elastic" Young's modulus reported in the resin datasheet [160], i.e. 2.8 GPa. This suggests that the VE technique provides accurate elongation measurements, thereby offering solid quantitative validation of the self-developed optical tool. In addition, it is worth noting that, even though the test was stopped before reaching specimen failure, the obtained results are still consistent with the resin's reported post-curing ultimate strength and elongation [160], namely 65 MPa and 6 %.